PB-FREE ELECTRONICS: FROM NANOTECHNOLOGY TO COMBINATORIAL MATERIALS SCIENCE

By

ALFREDO J. DIAZ GONZALEZ

A thesis submitted in partial fulfillment of the requirements for the degree of

MASTER OF SCIENCE

in

MECHANICAL ENGINEERING

UNIVERSITY OF PUERTO RICO
MAYAGÜEZ CAMPUS
2013

Approved by:

_____	_____
Pedro Quintero, Ph.D President, Graduate Committee	Date
_____	_____
Ricky Valentín, Ph.D Member, Graduate Committee	Date
_____	_____
Rubén Díaz, Ph.D Member, Graduate Committee	Date
_____	_____
Juan Ortiz, Ph.D Representative of Graduate Studies	Date
_____	_____
Gustavo Gutierrez, Ph.D Chairperson of the Department	Date

Abstract of Dissertation Presented to the Graduate School
of the University of Puerto Rico in Partial Fulfillment of the
Requirements for the Degree of Master of Science

PB-FREE ELECTRONICS: FROM NANOTECHNOLOGY TO COMBINATORIAL MATERIALS SCIENCE

By

Alfredo Díaz González

2013

Chair: Pedro Quintero-Aguiló
Major Department: Mechanical Engineering

The elimination of lead (Pb) from the electronics industry due to a government directive caused problems on the manufacturing and use of electronic components. The current alloys used to attach components have a significant higher processing temperature (~30-40°C) that those containing Pb. The higher processing temperatures cause damage to the electronic components; printed circuit boards (PCB) and represents an increase in energetic costs for the manufacturer. Tin whiskers are out-of-plane structures that grow from tin (Sn) plated surfaces and cause short circuits and metal vapor arc. The electrical connection of components to the PCB relies on leads that are close to each other and are manufactured from tin-plated copper.

Materials have shown a tendency to modify their bulk properties depending on powder particle size. Nanoparticle's coalescence temperature tends to decrease as particle size decreases. Exploiting this behavior, a nanoparticle based solder paste has been developed for attaching electronic components at a lower processing temperature to avoid thermally induced damage and reduce energy consumption. Tin nanoparticles were successfully synthesized via a wet chemistry route using tin (II) chloride dihydrated (metal precursor), 1,10-Phenanthroline (surfactant),

and sodium borohydride (reducing agent). A flux system was developed based on Ethylene Glycol. Results showed acceptable coalescence of the non-capped nanoparticles at temperatures as low as 200°C with a processing time of 20 minutes. Synthesized nanoparticles with capping agent required higher flux content thus resulting in a poor metallic load paste. A reduction in processing temperature of approximately 40°C have been found when comparing the developed solder paste with typical SAC lead-free solders (~240°C). The electrical behavior was found to be an order of magnitude below that of bulk tin.

Compositional libraries have been developed in an attempt to screen, via a high throughput method, alloys that are prone to tin whiskers growth. These libraries are samples containing a range of sub-samples with varying compositions within it than can be processed simultaneously. Using sputtering, a physical vapor deposition technique, a gradient composed of Ag-Cu was deposited over a Sn-plated Cu substrate. After reflow, the growth mechanism of the whiskers was accelerated using the *IEC60068-82-2 standard*. SEM and EDS analysis was used to characterize the growth of the tin whiskers at different elemental compositions. The gradients found across the samples are in accordance with the theoretical geometrical spacing. Tin whiskers were found on control samples, whereas almost all elemental compositions showed mitigation or elimination of the whiskers. This combinatorial material science methodology proved to be an efficient and fast screening method for the plating materials selection process in Pb-free electronics.

To my family, for the support and encouragement for pursuing my goals

Acknowledgments

It is a pleasure to thank the many people who made this thesis possible. Many thanks to my advisor, Dr. Pedro Quintero, for the guidance, support, for being such a great source of encouragement and for having total confidence in my work. Thanks to Lockheed Martin Corporation for the financial support throughout this investigation and giving us the opportunity to acquire the required materials and equipment to work on this project. Thanks to Dr. Wilfredo Otaño from University of Puerto Rico at Cayey who supported with his knowledge and equipment this project. To my friends and colleagues, I appreciated all the feedback, ideas, comments, questions and all the scientific discussion while having coffee, mate, tea or a few beers, thank you all. Michelle Almodovar, thank you for the unconditional support, true friendship and for all the good journal papers from your database. And last but not least, to my family for teaching me the value of education.

Table of Contents

List of Tables

List of Figures

1. INTRODUCTION

Semiconductor industry generates more than $298 billion annually according to the Semiconductor Industry Association[1]. Most of the revenue is from the sales of consumer electronics, i.e. cellphones, laptops, tablets, etc. This industry have encounter technical difficulties after a legislation banned the use of some materials, mainly lead (Pb), that have been used for many years; thus resulting in manufacturing and reliability problems with the integration of new technologies.

In 2005, Intel (one of the biggest electronics company with a $34.2B annual revenue) made the statement that the efforts to remove lead from its chips have so far cost the company more than $100 million and there is no clear end in sight to the project's mounting costs. In 2011, Intel reported that their products are still not completely Pb-free although some of their product lines have achieved that status[2]. The major impacts of lead-free soldering in electronics can be attributed to higher soldering temperatures and the increased complexity of the microstructures of solder joints. The main issue is that higher soldering temperatures might cause damage to temperature sensitive components[3].

For surface mount technology (SMT), solders are demanded to have high reliability and dimensional stability for improved mechanical properties[4]. Figure 1 shows a SMT device placed over the solder paste going through a reflow process to attach the component. Solder paste can be deposited on top of the pads using a process called stencil printing. Electronic components have leads that are responsible for providing mechanical support and electrical contact to the chip. The leads in electronic devices are typically coated with a thin Sn-based electroplated layer to improve their solderability with the printed circuit board[5]. For lead-free component's

metallization and solders, materials such as Cu, Ag, Bi to mention a few, are typically added to Sn, however there is not much confidence in these metallurgical systems when compared to the well documented Sn-Pb system.

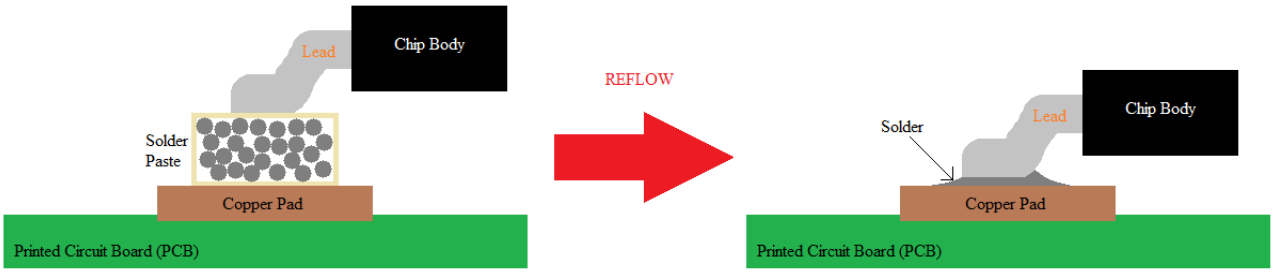

Figure 1: Schematic of a SMT component going through a reflow process.

The objective of this investigation is to: (1) develop a solder paste based on nanoparticles which can be stencil printed for the attachment of SMT components and (2) find suitable plating alloys for the mitigation of tin whiskers.

1.1. Motivation

In the last years, there has been a global endeavor towards the development of eco-friendly technologies. In order to achieve consensus through the community, often, laws are issued to establish the requirements for these technologies. The RoHS (Restriction of Hazardous Substances) Directive is a European Union (EU) initiative intended to reduce the environmental impact of electrical or electronic products in the waste stream and improve the recyclability of that waste. Under RoHS, electrical and electronic products destined for sale in Europe must be free of six hazardous substances by July 1, 2006 as defined by the directive [6]. The prohibited materials are lead, mercury, cadmium, hexavalent chromium, polybrominated biphenyls (PBB) or polybrominated diphenyl ethers (PBDE)[2]. There are exemptions to RoHS, automotive electronics must be compliant in EU by 2016, medical electronics by 2014 and the military and aero-

nautic/aerospace equipment are currently exempt of the guidance documents. Since the initiative took place in 2006, other countries that proficiently participate in the electronics consumption and production market, like China or Japan[7], have enacted the legislation. Some states in the USA has similar environmental legislations to the RoHS, but due to the suppliers moving their commercial products towards RoHS compliant, the US is in the urge of developing new technologies to replace the non-compliant ones, mainly because the removal of lead (Pb).

The Pb-free initiative is in charge of developing new solder alloys and lead finishes for RoHS compliant electronics. For the last decades, Sn-Pb solder alloys have been the preferred interconnection material used in such applications[8]. Sn-Pb solders were relatively inexpensive and exhibited high ductility, low surface tension, good solderability and wettability, and low melting temperature (183°C for the eutectic composition Sn-37Pb by weight). Many different Pb-free solder alloy systems, such as Sn-Ag, Sn-Cu-Ag, Sn-Cu, Sn-Ag-Bi, have been developed and are currently been used as promising alternatives to Sn-Pb, but the preferred one is the Sn-Ag-Cu (SAC) system due to its relatively low melting point (~217°C), good solderability, high strength, low wetting angles and good reliability[9].

The peak reflow or processing temperature of Pb-free alloys will increase, for example, from 220°C when using conventional Sn-37Pb eutectic solder to ~250°C when using a Sn-Ag-Cu alloy causing potential damage to electronic components that cannot withstand such high reflow temperatures[8]. Thus, in order to use the lead-free solders, all the materials of the PCB (printed circuit board) and the components on it must be able to withstand the increased thermal exposure. This leads not only to requiring support of the infrastructure (materials, equipment, components, PCB, etc.) but also to increased cost and lower reliability. Furthermore, significantly more energy is needed, which causes environmental concerns[10].

As part of this investigation, the melting point depression of tin (Sn) nanoparticles, which is an intrinsic property of nanoparticles where the decreasing particles size is poised to significantly reduce the melting point of the material due to the increase of surface energy[11–15]), will be used to produce a lead-free solder paste with lower processing temperature.

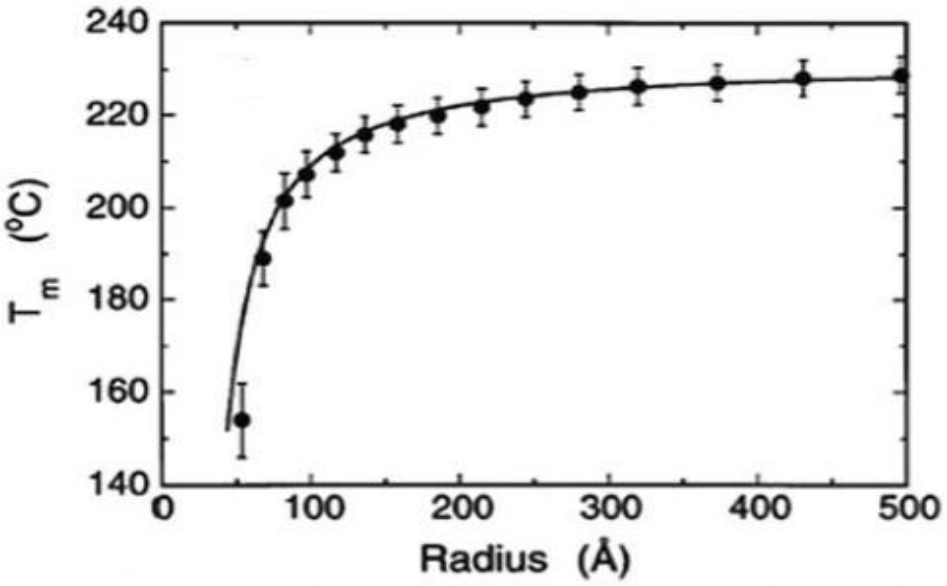

Figure 2: Melting point size dependence of tin nanoparticles. The solid line is based on theory and the point are experimental results[12]**.**

Figure 2 shows graphically the significant decrease in melting point with particle size. A solder paste is a homogeneous and kinetically stable mixture of solder alloy powder (Sn nanoparticles, in this case), flux, and vehicle, which is capable of forming metallurgical bonds at a given soldering condition[16] and that have the properties required by the manufacturing process. The solder paste properties, such as mechanical strength or electrical conductivity, will be highly influenced by the reflow profile. After reflow, the solder will have a bulk behavior. The reflow process will induce nanoparticles to coalesce. The consolidation of the nanoparticles will increase the particle or cluster size thus reducing the total surface energy of the system. The advantage of this process will be to have a higher melting temperature of the solder at application

conditions than in processing due to densification of the metal content, hence annihilating the effect of size-dependency on the melting point.

Pb-free finishes (for lead's plating) such as nickel/palladium/gold, nickel/gold, SAC, and pure tin had replaced the Sn-Pb, but most of the companies prefer the pure tin finish due to the low cost compared to alloys containing gold[17], [18]. Many pure tin platings have a tendency to develop tin whiskers, which (electrically conductive single crystal structures that growths spontaneously from a Sn plated surface[19]) combined with the lack of accepted methods for testing whisker growth susceptibility, gives rise to major reliability concerns[17], [20]. Tin whiskers were first reported and recognized as a threat to the electronics industry in a laboratory study by Bell Telephone Labs in 1951[18]. Whiskers of critical length are a reliability risk for electronics because they could bridge interconnects, causing a short circuit or a metal vapor arc, or they could break off and interfere with other mechanical or electronic components.

In this investigation a technique to screen for alloys that minimize the growth of tin whiskers will be presented by using combinatorial materials science. Combinatorial materials science is a high-throughput screening method that creates "libraries" of materials by generating some form of controlled gradient. Samples with continuous gradients in different directions will be manufactured using a magnetron sputtering system. Sputtering is an atomic deposition technique that removes material from a target and deposits it over a substrate having a thickness gradient according to the geometry of the system. Processing the samples using this method will be faster and cheaper because they require less interaction and consumption of resources, i.e. materials, processing energy, characterization equipment usage time, among others.

1.2. Specific Objectives

- Develop and characterize a Sn nanoparticle based solder paste.
  - *Study the best embodiment for the nano-solder paste, considering that it will be used for SMT processes.*
  - *Determine optimal process parameters for an attachment to occur.*
  - *Investigate the mechanical and electrical responses of the solder after re-flow.*
- Use combinatorial materials science to present a possible method for testing alloys that minimizes the growth of tin whiskers in Pb-free electronics.
  - *Develop a sputtering process that produces controlled directional gradients of materials.*
  - *Correlate whisker growth with elemental composition using a SEM with EDS module.*

1.3. Literature Review

1.3.1. Nanoparticles as solder

1.3.1.1. Size dependent melting properties of nanoparticles

Many researchers have reported the thermal characteristics of synthesized nanoparticles accounting for a reduction in the melting point. The idea of smaller particles having a lower melting point than the bulk have been around for years, but in 1998 Schmidt et al.[21] published in Nature that they have found irregular variations in the melting point of size-selected clusters. Using calorimetric analysis developed by Lai et al.[12](1996) for isolated tin nanoparticles, they experimentally acquired data for clusters of different sizes finding irregular tendencies, thus con-

cluding that the size dependence of melting point cannot be explained easily and depends on a complicated interplay between geometric and electronic structure. In 2000, Efremov et al.[22] used the nanocalorimetric technique to investigate the thermodynamic properties of indium clusters. They observed multiple periodic melting peaks which were attributed to certain clusters with specific sizes that are more stable than others. They also discovered that the incremental difference between the sizes of these stable particles corresponds to one atomic layer in radial thickness. Jiang et al.[23], in 2007, published a work based on synthesis and thermal characterization of Sn-Ag alloy particles. They synthesized the nanoparticles using a low temperature wet chemistry route with a surfactant to reduce the agglomeration and oxidation of the nanoparticles. For an average particle size of 10nm, differential scanning calorimetry (DSC) revealed a melting point of around 194°C. The following year two groups, Jiang et al.[24] and Zou et al.[8] published works on synthesis and characterization of Sn-Ag-Cu nanoparticles thermal properties. Jiang et al. used a chemical reduction method to produce surfactant covered SAC nanoparticles to investigate their thermal behavior which resulted in a melting point as low as 199°C. When using naked nanoparticles (particles without surfactant) no obvious peaks on the DSC scan were observed due to oxidation of the particle's surface. Zou et al. used a self-developed consumable-electrode direct current arc to produce SAC nanoparticles of approximately 30nm having a melting point, according to DSC, of 213.9°C. No significant difference was found from nanoparticles covered in two different surfactants. A comparison of experimental data with the homogenous melting model was performed showing concordance, and demonstrating that their method produced size-dependent melting nanoparticles. In 2010, Zou et al.[13] published that tin nanoparticles, synthesized via a wet chemistry route, using tin 2-ethylhexanoate, sodium borohydride, 1,10-phenanthroline and anhydrous methanol as precursor, reducing agent, surfactant and sol-

vent, respectively; resulted in diameters of 81, 40, 36 and 34 nm that had a melting points of 226.1, 221.8, 221.1 and 219.5°C, according to DSC measurements. They compared their experimental results to various melting-point models (LSM (liquid-skin melting), SPI (surface-phonon instability), LNG (liquid nucleation and growth) and HM (Homogenous melting)), concluding that experimental data is in accordance with the LSM model and SPI model, where the LSM model gives a better understanding for the melting behavior of the Sn nanoparticles. LSM suggests the formation of a liquid layer over the solid core at a low temperature which remains unchanged until the particle transforms completely to liquid at the melting temperature of the bulk. Alarifi et al. [25] published a procedure where chemically synthesized silver nanoparticles, covered in an organic material to prevent room temperature sintering, proved to bond copper wires at temperatures as low as 160°C.

1.3.1.2. Nano-paste development

Some researchers have applied the advances in the synthesis and melting point depression of nanoparticles to produce nanosolder paste for lower processing temperatures. In 2005, Hsiao et al.[26] published their findings in the properties of a solder based on SAC chemically synthesized nanoparticles mixed with a Rosin mildly activated commercial flux (TACFLUX®, Indium Corp.) to produce a paste. The processing temperature of the solder paste was reduced to almost 215°C and they reported to have favorable wetting of the surface. Later, Lin et al.[27] reported that the addition, in less than 1 wt. % concentration, of Cu nanoparticles to eutectic Sn-Ag microparticle solder paste resulted in a 20% increase in microhardness due to a refinement of the intermetallic compounds. Andersson et al.[4] reported an increase in Vickers microhardness when adding SAC nanoparticles from 0 to 5 wt. % to a Sn-58Bi matrix due to a refined crystal grain growth. In 2008, Liu et al.[9] concluded in their review paper that pure nano-solder pastes

are a relatively new research subject and it should be studied down to its core to take advantage of the lower melting point. Some experiments of such solders have shown complete reflow and wetting on Cu substrates patterned using conventional stencil printing techniques, but lots of research is still pending. For silver nanoparticles solder pastes, Wakuda et al.[28], Alarifi et al.[25], among others, have published that nanosilver can be mixed with hexanol, toluene or even in deionized water obtaining reasonably good mechanical properties. Jiang et al.[15] in 2009 synthesized tin, tin/silver (SnAg) and tin/silver/copper (SnAgCu) alloy nanoparticles of various sizes to prepare a solder paste. They developed a flux based on citric acid and ethanol having a low reflow temperature. Wetting test for the as-prepared SnAg and SnAgCu alloy nanoparticle pastes on a Cu surface showed the typical Cu_6Sn_5 intermetallic compound (IMC) formation.

1.3.1.3. Important findings

Nanoparticle based solder paste take advantage of the melting point depression to reduce the reflow temperature. The basic components of a solder paste are the metallic powder, flux, and a vehicle that provides the desired rheology to the mixture. Common vehicles are low boiling point liquids such as alcohols or glycols. The flux system is in charge of cleaning the surfaces, commonly weak or mild organic acids are used, for example citric acid. No significant effect on the melting point depression was observed on oxidized or agglomerated nanoparticles. The melting point depression has shown to be a single occurrence phenomenon; after the nanoparticles coalesce the re-melting temperature will be higher than the initial processing temperature. Intermetallic compounds have been found on nanoparticle based solders, showing typical metal behavior after reflow. This project will take advantage of the melting point depression of Sn nanoparticles to engineer and investigate the behavior a solder paste to attach SMT components. The properties of the attachment will be characterized and compared to Sn-Pb. The mechanism

of coalescence of the nanoparticles going through reflow will be studied to provide further knowledge on how nano-solder works. As a result of this investigation, optimal parameters of processing time and temperature for the best mechanically acceptable attachment will we obtained in order to suggest nano Sn based solder as an alternative to SAC solder in commercial electronics.

1.3.2. Tin Whiskers

1.3.2.1. Mitigation strategies

Few techniques have been published as whiskers mitigators. A Ni underlayer has been suggested to reduce the propensity of growing whiskers by inhibiting the formation of intermetallics compounds between Cu and Sn. Heat treatments, such as annealing, have been used to reduce the residual stress on the plating as a result of the electroplating process. Also, matte tin finishes on the components, according to some researchers, suppress the growth of whiskers better than bright tin. Other suppression techniques include the use of thicker coats of Sn or the use of alloys[29–31]. Wang et al.[5] published that the Ni barrier layer was very effective in suppressing whisker growth according to their research, but Panashchenko et al. [32] contradicted them publishing that the Ni barrier layer did not have any noticeable effect in suppressing whisker growth during the sequential environmental test exposure. Fukuda et al. [33] reported that annealing only retard the growth of the whiskers. It has been documented that the finish of the tin (matte/bright) is not what matters, but the parameters of the plating process is what reduces or improves the growth of whiskers[29]. Mitigation techniques have been influenced by contradictory information that leads to conclude that the suggested mitigation strategies are not valid.

1.3.2.2. Whisker testing protocol

Previous works involve the use of test coupons as samples[32–34]. Preparing coupons is a labor intensive work, because samples are fabricated and characterized one at a time. In this investigation, a novel technique will be presented based on creating alloys by gradients across the sample, i.e. libraries. One sample will contain a wide range of alloys having the advantage of single sample handling, processing, and characterization. Combinatorial libraries can provide a convenient, compact, and powerful platform for scientific research. When properly designed, the library amplifies the scientific effectiveness of sample preparation and allows researchers to consider "spaces" rather than individual "points"[35]. The procedure to fabricate the gradients of materials across the libraries will be performed via sputtering. The overlap of different gradients will be used to obtain a range of possible compositions over the sample. The investigation will present a test protocol to screen for alloys that minimizes the growth of tin whiskers.

2. THEORETICAL BACKGROUND

This section is focused in discussing theoretical concepts that are relevant to this project. A description of electronic packaging and the soldering processes, explanation on how nanoparticles grow and behave, possible growth mechanisms for tin whiskers, and a description of the deposition technique for producing the libraries will be presented.

2.1. Electronic Packaging

Electronic packaging is the discipline in charge of providing carriage to a silicon chip full of transistors with electrical interconnections, mechanical support and thermal dissipations[36]. As shown in Figure 3, electronic packaging is subdivided into levels. Level 0 goes from the growth of single crystal Si to the dicing of individual chips containing millions of transistors. Level 1 involves the manufacturing of the carrier for the chip, connecting the Input/Outputs and providing protection from outside elements. In level 2 the electronic devices are attached to a printed circuit board (PCB) by the use of some kind of solder. Above level 2, interconnection of boards is performed for a specific use[37]. The focus of this investigation will be on levels 1 and 2.

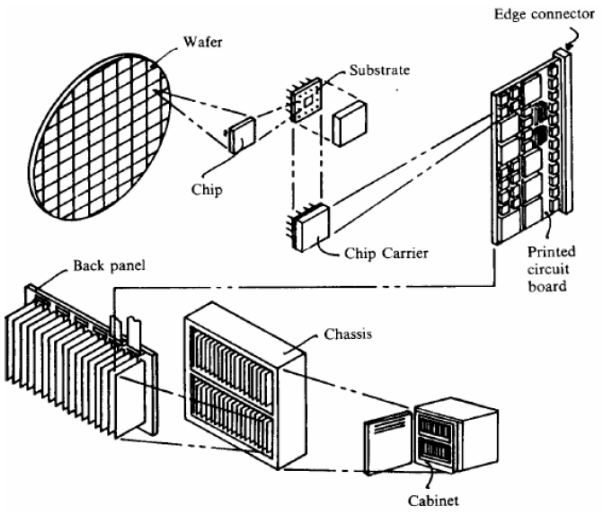

Figure 3: Levels of electronic packaging (source: Seraphim, Donald P., Ronald Lasky, and Che-Yu Li. Principles of Electronic Packaging. New York: McGraw-Hill, 1989.)

In Figure 4(B), there is a schematic of a typical surface mount technology (SMT) component. SMT components are electronic devices that are soldered onto the surface of a PCB. The leads of the component provide the mechanical support and also an electrical path for the signal. Typically, the leads are constituted of a copper substrate with an electroplated material over it to protect the substrate from the environment. In Figure 4(A), there is a schematic of a typical SMT component showing acceptable limits of solder that can be used as an attachment. A real SMT component is shown in Figure 4(C). The solder is added as a paste with a rheology similar to toothpaste. The solder paste has three main constituents, metallic powder, a vehicle that provides the desired rheology and a surface cleaning agent, typically an acid.

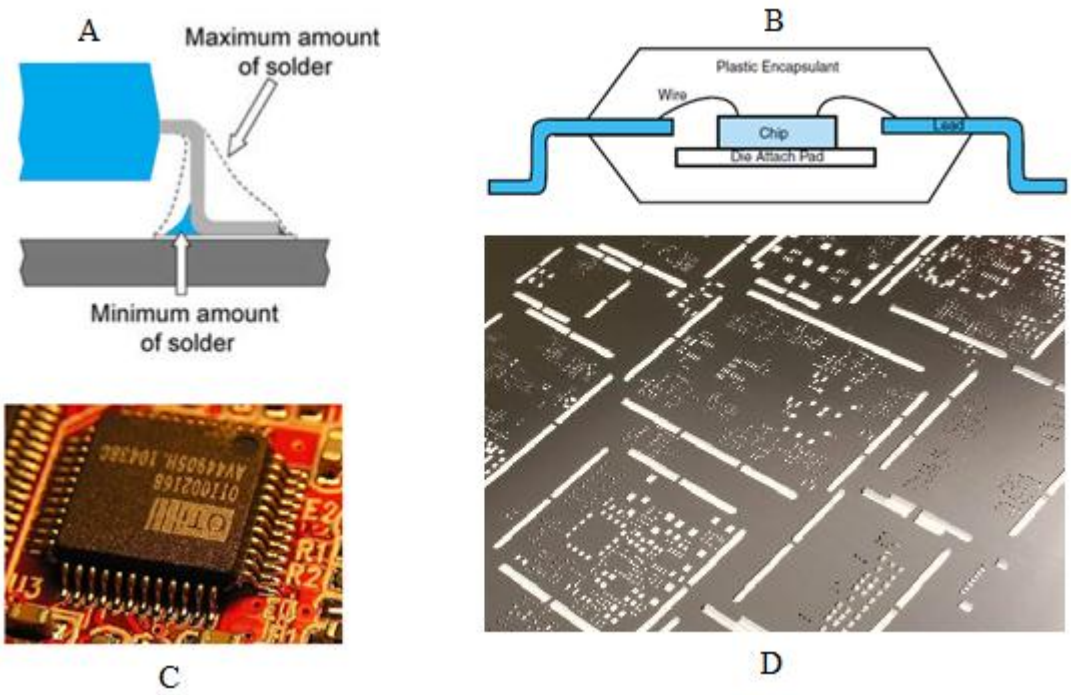

Figure 4: (A) Schematic of an SMT attachment (B) Schematic of an SMT electronic component (C) Real SMT component attached to a PCB [38]

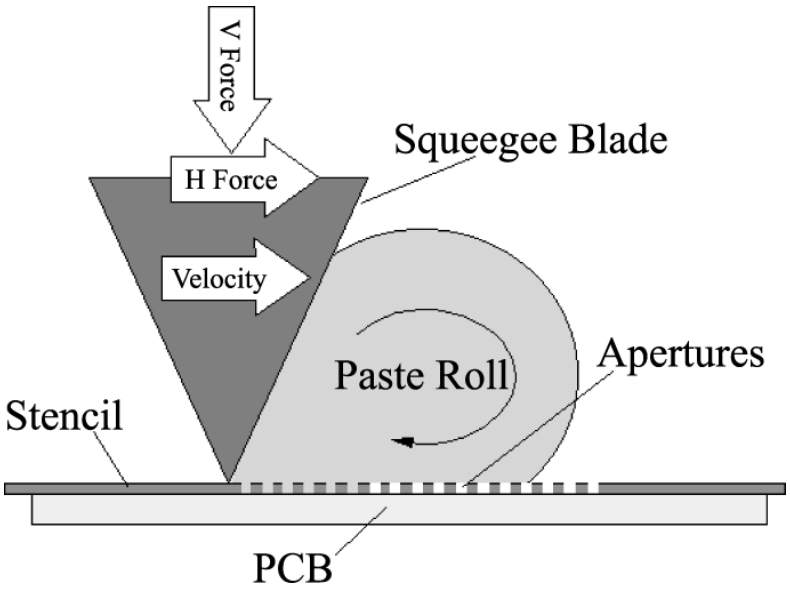

Figure 5: Stencil printing process schematic (source:http://www.emeraldinsight.com/journals.htm?articleid=878540&show=html)

A process called stencil printing, shown in Figure 5, is used to deposit the paste onto the desired areas of the PCB (called pads). Using a stencil, shown in Figure 4(D), solder paste is forced through the apertures leaving the paste over the pads. After the solder is deposited over

the pads, the electronic components will get positioned on their respective connecting points. Then, a thermal profile called reflow is used to melt the solder paste and provide a permanent attachment of the components. A typical reflow profile is shown in Figure 6, with the usual four stages: pre-heat, soaking, reflow, and cooling. The purpose of pre-heat is to evaporate the solvent from the paste. Then, the flux will be activated in the next stage follow by soaking to clean the surfaces to be attached. During the reflow stage, the metallic content of the paste will melt and then solidify upon cooling to produce the attachment of the component. There are different kinds of components, but this research will focus on SMT components attached by stencil printing.

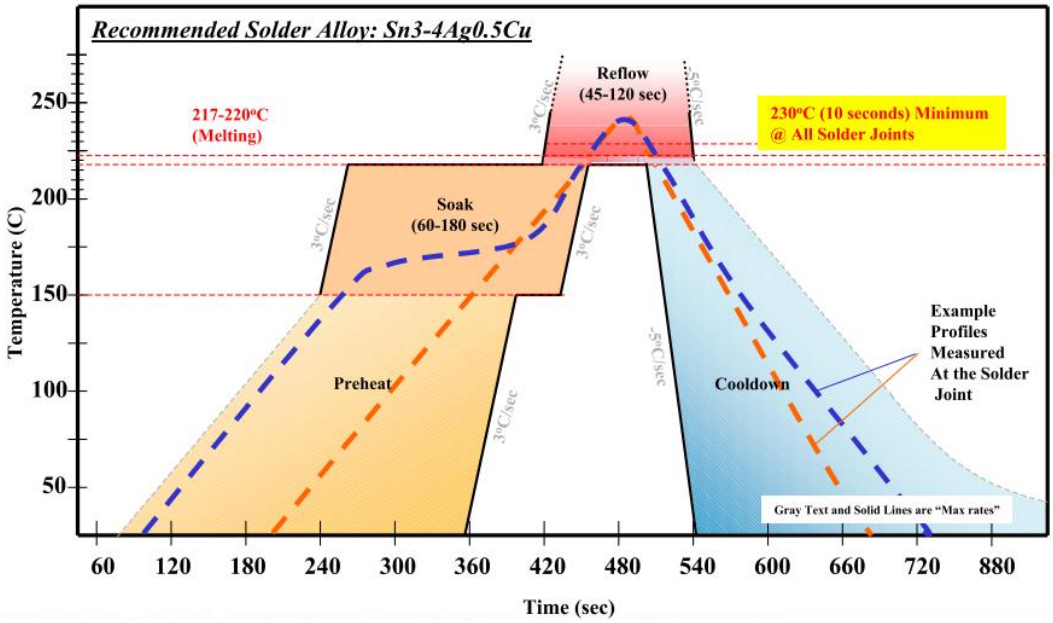

Figure 6: Typical reflow profile for SAC solder[39]

2.2. Nucleation, growth and agglomeration of nanoparticles

Despite the fact that a unique definition does not exist for nanoparticles, they are usually referred to as particles with a size up to 100 nm. It can be argued that below that size, the physi-

cal properties of the material don't just scale down or up, but change. Nanoparticles exhibit completely new or improved properties based on specific characteristics (size, distribution, morphology, phase, etc.), if compared with larger particles of the bulk material they are made of. Nanoparticles present several different morphologies, including flakes, spheres, dendritic shapes, etc[40].

Nanoparticles can be made of a wide range of materials, the most common being metal oxide, ceramics, metals, silicates and non-oxide ceramics. Even though nanoparticles of other materials exist, e.g. those based on polymer materials or compound semiconductors, the former categories count for the most part of current applications[40].

Nanoparticles can be obtained from a number of different methods. Most common approaches include solid state or vapor methods, such as grinding, milling, or vaporization and recondensation (are top-down approaches based on the diminution of the bulk form) and chemical synthesis/solution methods(bottom-up approaches based on aggregation of atoms)[40][41]. For this particular research a wet chemistry reduction route will be used for the synthesis of tin nanoparticles due to laboratory equipment restrictions. The "bottom-up" method of wet chemical nanoparticle preparation is based on the reduction of metal salts. In this type of synthesis a metal oxide precursor is prepared in a solution that will be later reduced in order to obtain metallic nanoparticles. The nucleation process of the nanoparticles starts with the dissolution of the precursor oxide, in this case $SnCl_2*2H_2O$. The released species in solution are first associated with the surfactant (1,10 phenanthroline) then reduced using sodium borohydrate.

The growth of nanocrystals in solution involves two important processes, the nucleation followed by the growth of the nanocrystals. Once metallic particles are formed, they tend to

form clusters or start growing by aggregation of single crystallites. There are different stages on the particle growing; the incorporation of metallic particles from the solution is usually the first growing stage and further growing is due to the dissolution of small particles through the so-called Ostwald ripening process[42].

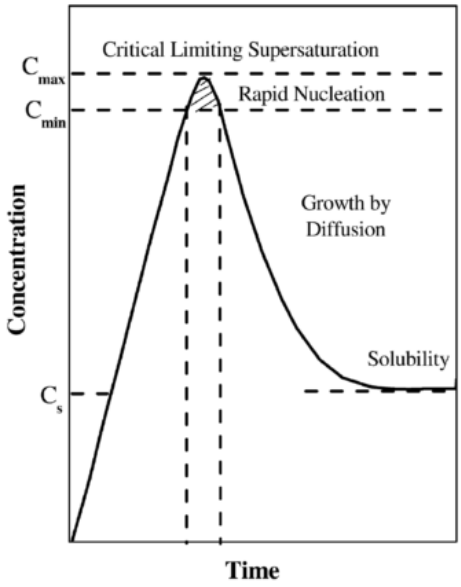

Figure 7: Schematic of La Mer's condition for nucleation of nanocrystals[43]

La Mer's diagram, shown in Figure 7, is very useful to describe the mechanism for the formation of nanoparticles in a synthesis environment. The mechanism suggested is that a synthesis of a material should be designed in such a way that the concentration increases rapidly, rising above the saturation concentration for a brief period, when a short burst of nucleation occurs with the formation of a large number of nuclei in a short space of time. These particles grow rapidly and lower the concentration below the nucleation level whilst allowing the particles to grow further at a rate determined by the slowest step in the growth process, thus separating the nucleation and growth in time[43].

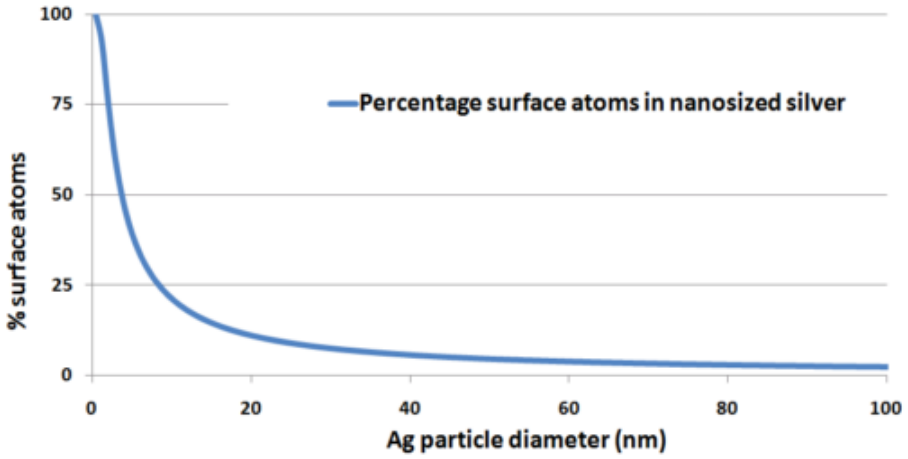

Figure 8: The percentage of surface atoms of spherical silver particles as a function of diameter of the particle[44]

It is clear that very small particles have a big fraction of their atoms located on the surface. This has a very big influence on the properties of the particles, e.g. giving an increase in both re- activity and vapor pressure for decreasing particle sizes. To make stable metal nanoparticles, the aggregation process must be prevented at an early stage of the particle formation. Often, this aggregation is caused by Van der Waals forces. There are in general two methods for achieving counteraction, electrostatic and steric stabilization[44].

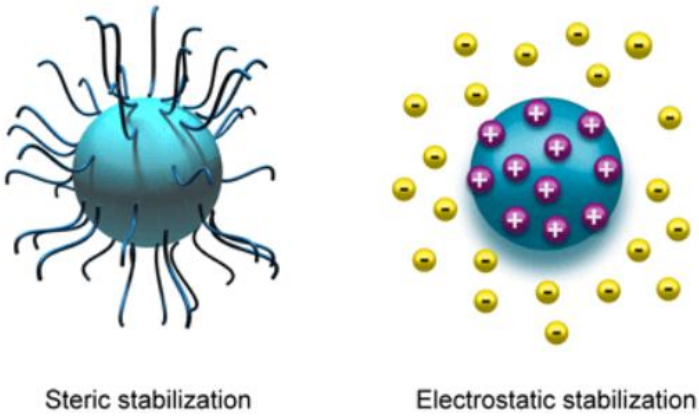

Figure 9: Schematic of the mechanisms of steric and electrostatic stablization[44]

Electrostatic stabilization is achieved by providing the nanoparticle's surface with a net charge from absorbed species to promote electrostatic repulsive forces among them. Stearic stabiliza-

tion is achieved by the coordination of large molecules, such as polymers or surfactants, to the surface of the nanoparticles. The molecules polar groups are attracted to the surface of the nanoparticle providing a mechanical barrier between metal cores. Schematic of each stabilization technique is provided in Figure 9.

2.3. Nanoparticle coalescence methods:

2.3.1. Melting Point Depression and Liquid Skin Melting (LSM) model

At small sizes, nanoparticles may melt at temperatures (T_{cm}) significantly below the bulk melting point, due to increasing surface energy at small sizes[11], [12], [45], [46], this is well established both experimentally and theoretically[46]. From an atomistic point of view, as the size of the nanostructure decreases an increased proportion of atoms occupy the surface or interfacial sites. The atoms in the surface are more loosely bound than bulk atoms, which facilitates the melting of the nanostructure[45]. Experimental results have revealed surface melting before the complete melting. The driving force for the surface melting is thought to be a reduction in the total surface energy[46]. There are different size-dependent melting models (LSM, SPI, LNG and HM). Zou et al., when comparing synthesized Sn nanoparticles experimental melting properties to theoretical models, showed that their data is in accordance with the LSM model and SPI model, where the LSM model gives the better representation of what they found[13].

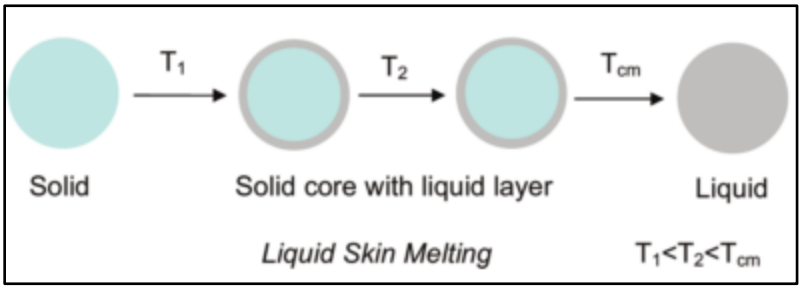

Figure 10: Liquid skin melting model (LSM)[46]

LSM states, as shown in Figure 10, that there is a temperature (T_1) in which a liquid layer is formed over a the solid core at a low temperature that remains unchanged until the particle transforms completely to liquid at the melting temperature, however there is another theory that states that the liquid skin thickness increases slowly when the temperature is increased until the T_{cm} is reached and the solid core abruptly melts. Experimental observations showed that the liquid skin growth occur near the size-dependent melting temperature[47].

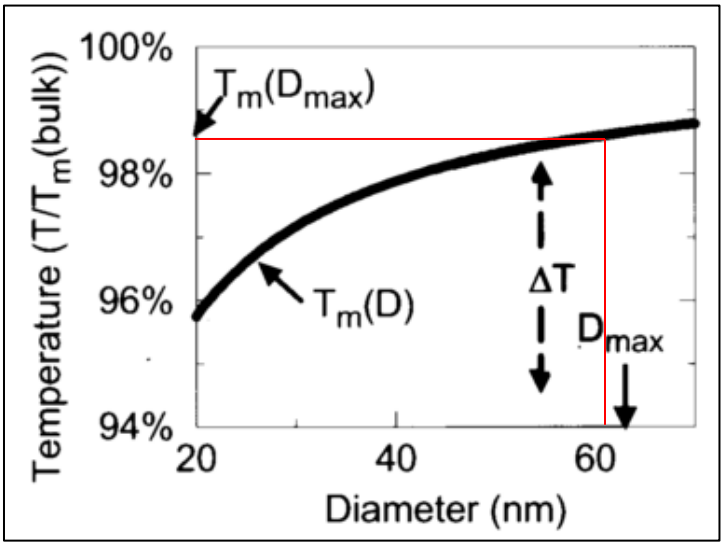

Figure 11: Melting temperature vs particle diameter for Pb[47]**. The figure shows the temperature ratio $T/T_m(\infty)$, in which $T_m(\infty)$ (T_m(bulk))represents the bulk melting temperature of Pb and T is the actual temperature. The curve, $T_m(D)$, represent the temperature at which a nanoparticle having a diameter, D, will melt.**

Let's consider a distribution of particles with maximum particle diameter, D_{max} (as shown in Figure 11), a sharp or narrow crystallite size distribution is achieve near to D_{max} by heating the sample to slightly below $T_m(D_{max})$ because, as temperature approaches the melting temperature of bulk, the majority of the particles are molten while the remaining crystallites might have a liquid skin. When the sample is then cooled slightly, the liquid particles remain liquid while the liquid skin on the crystallites solidifies, due to undercooling. In situ x-ray diffraction can then provide the changes in the average crystallite size and hence, the liquid skin thickness. Experimentally, the thickness of the liquid layer is confirmed by the use of XRD pattern peak shape

analysis. X-ray diffraction from 52 nm Pb crystallites, with a 0.5nm liquid skin, reveals reversible liquid skin appearance as a change in the crystallite volume, when cooling the samples down by $\Delta T=3.5\%$ from 99.5% $T_m(D_{max})$. The liquid skin thickness increases near the size-dependent melting temperature[47]. Also, it was proposed that for very small particles, the melting temperature becomes lower than the temperature where surface melting occurs, resulting in a sharp melting transition[48]. Despite this theory, the mechanism by which the nanostructures melt is not fully understood[45].

2.3.2. Temperature driven pressure-less sintering

Sintering is a thermal treatment for bonding particles into a coherent, predominantly solid structure via mass transport events that often occur at the atomic scale. The bonding leads to improved strength and lower system energy[49]. The temperature needed to induce bonding through sintering depends on material and particle size. Most materials exhibit sintering behavior between temperatures around 0.5 to 0.8 T_m(bulk). Bonds and densification become more evident with higher temperatures, longer times and smaller particles.

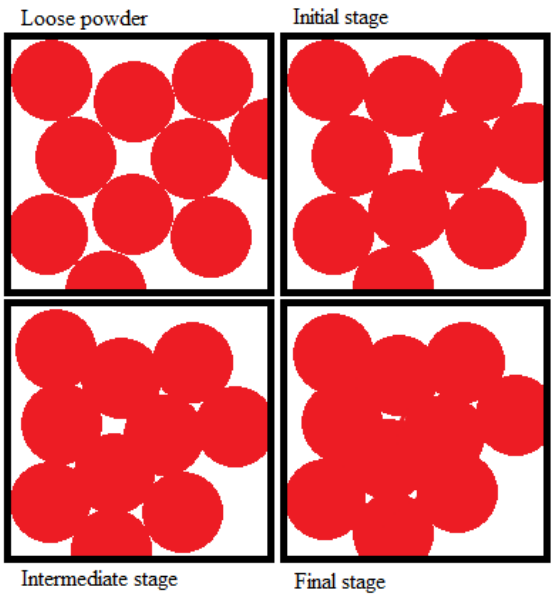

Figure 12: Sintering densification stages.

For simplicity, solid-state densification is considered to be accomplished through three stages: initial, intermediate and final. Multiple mechanisms are involved throughout these stages, namely, evaporation-condensation, surface diffusion, grain boundary diffusion, bulk diffusion, viscous flow, and plastic deformation[50]. In the initial stage, there is a growth of interparticle neck. For nanoparticles, with excessive surface area and highly curved surfaces, surface diffusion is expected to be extremely rapid in this early sintering stage. Evidence of the surface diffusion contribution to the neck formation in nanopowder sintering has been given by many researchers[50]. During the intermediate and final stage there is a substantial reduction in the pores and the interconnections increase with time, at the final stage the grain growth is evident. Surface diffusion mechanisms are most sensitive to particle size. Therefore, enhanced surface diffusion with reduced low-temperature densification should be observed in sintering nanoparticles[50].

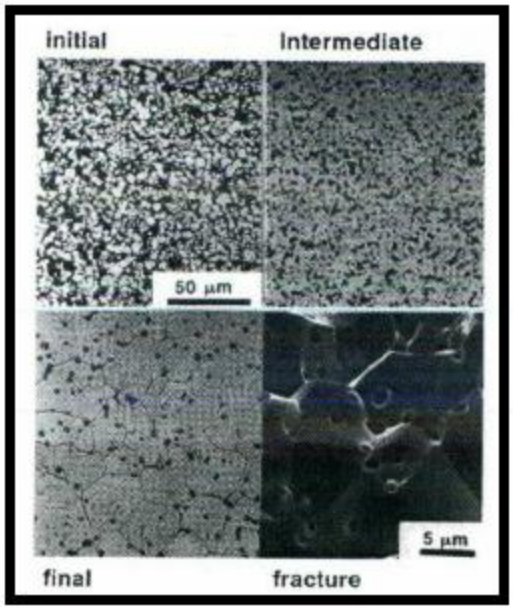

Figure 13: Example of sintering progress in tungsten powder[49]**.**

2.4. Growth mechanism of tin whiskers

Tin whiskers are conductive structures that grow spontaneously from Sn films over different types of substrates having a shape variation that goes from straight needle-like structures to kinked forms. The major reliability issue with whiskers is the electrical shortening propensity in electronic components; been attributed for failures in satellites, nuclear facilities, among other. There is no consensus on an accepted explanation of the mechanism of whiskers growth, but there are some commonly agreed factors involved in their formation and their growth rates [51]. Tin whisker growth is primarily attributed to compressive stresses in the Sn plating. The sources of the compressive stress could be the grain size, shape or orientation, impurities in the lattice, external mechanical stress (like bending, scratching or Coefficient of Thermal Expansion (CTE) mismatch), oxidation, substrate stress or the growth of intermetallic compounds on the interface[29].

Smetana [52] published in 2007 a theory that comprises and apply to most of the tin whiskers growth cases. The key growth mechanism is a recrystallization process due to grain boundary sliding caused by compressive stress which may result in growth of the whisker grain. When stress is present, the grain boundary atoms moves leaving vacancies on the base. The movement of atoms from the grain boundary into the whisker grain results in open sites in the adjacent grain boundary, where Sn atoms can then move to by diffusion. Grain boundary diffusion from the higher stress grain boundaries can now occur. The Sn atoms will start moving to the vacancies due to the difference of energy states from the surrounding areas to the base, where the whisker grain will start to grow. This grain growth is unique in that it results only in vertical growth of the grain, which results in a whisker. The whiskers will grow from the base (the interface between the Sn plating and the substrate) to out of the plane.

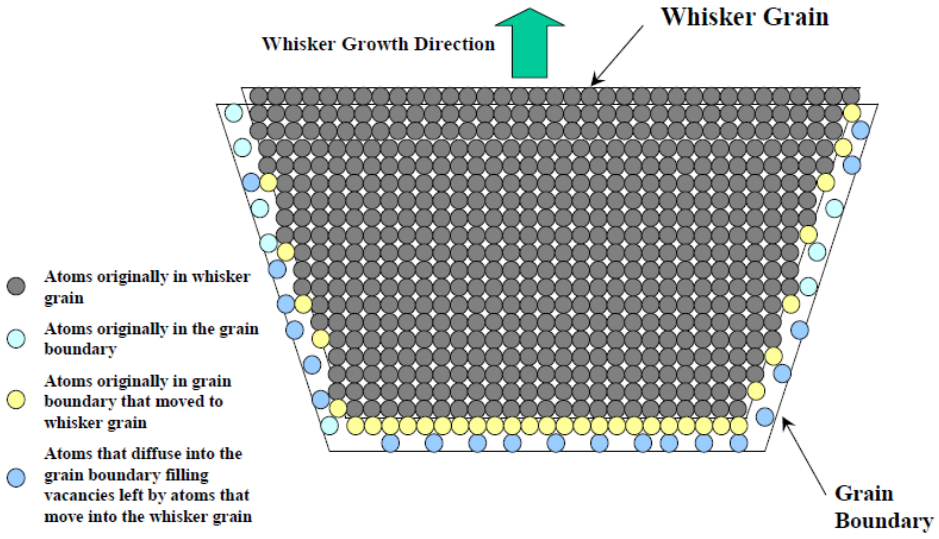

Figure 14: Whisker growth mechanism schematic[52]

The mechanism of whisker growth is better described in Figure 14. The base of the whisker is the lower part of the figure and the whisker grain is growing out of the surface. The growth is a consequence of a cyclical process. The atoms in the grain boundary will move into the whisker

grain. Then, atoms from the surroundings will diffuse into the grain boundary repeating the process.

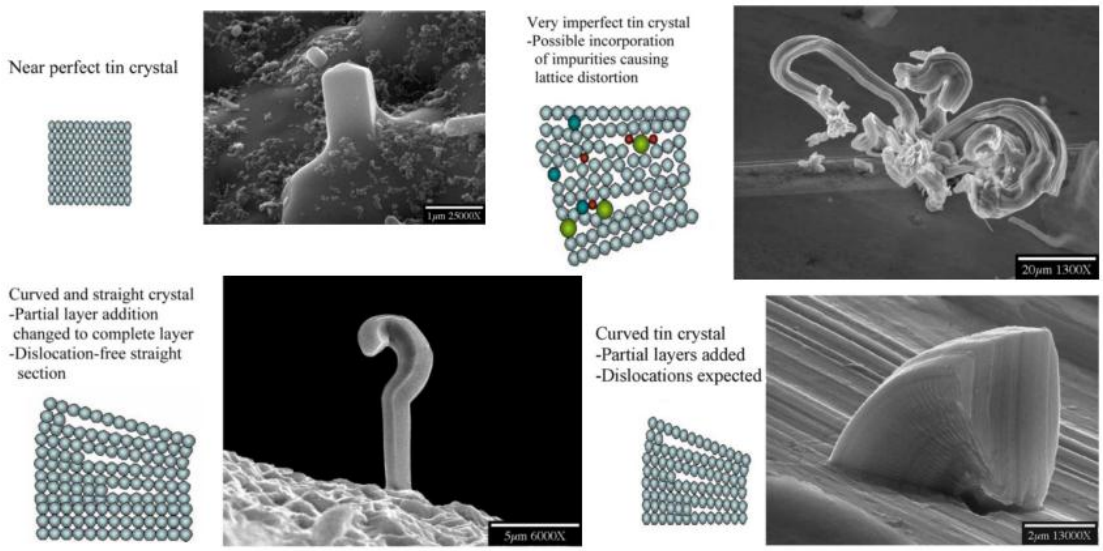

Figure 15: Crystallographic arrangement of atoms related to whisker shapes[52]

Different shapes of whiskers could be explained by this theory, as shown in Figure 15. Dislocations or impurities in the whisker grain will produce a lattice distortion causing the final whisker shape. Based on this theory of tin whisker growth, the SnPb grain structure does not support significant tin whisker growth because of lots of horizontal grain boundaries, almost an equiaxial grain structure and not a columnar grain structure, like typical matte or bright Sn.

2.5. Sputtering

The sputtering phenomenon was discovered by W.R. Grove in 1852. Sputtering is the emission of atoms or molecules from a solid or liquid surface caused by a bombardment of heavy particles, usually ions with high velocities. In practice, it is necessary to control the erosion effect on the desired surface (target) to avoid contamination from other surfaces inside the chamber. Sputtering is produced by generating plasma near the target in the presence of an inert gas that could be partially ionized. High vacuum is needed in order to increase the mean free path

(the distance and atom could travel without colliding with another atom) of the atoms. Sputtering is driven by a momentum transfer between the ions and the target. The distribution of emitted atoms depends on the direction on the incident ions. Ions with higher energy and mass will produce a higher erosion rate on the target[53], [54].

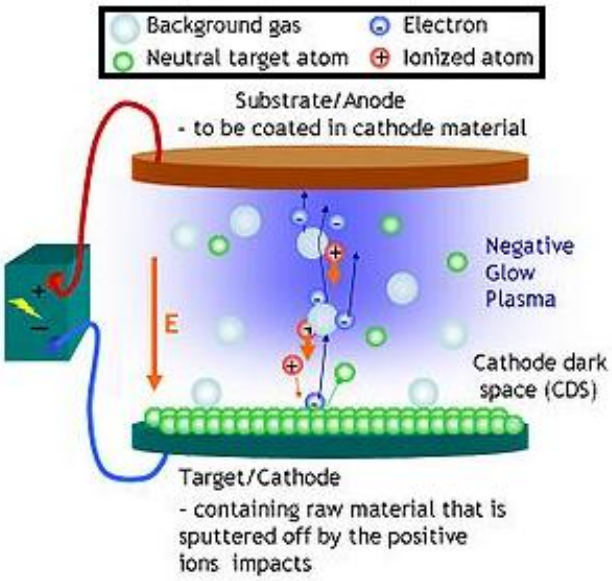

Figure 16: Schematic of sputtering basics. (source:http://www.etafilm.com.tw/PVD_Sputtering_Deposition.html)

Figure 16 shows the basic mechanism of sputtering. The ionized atoms are accelerated towards the target or cathode by electric potential removing atoms from the surface and sending them at a lower velocity towards the substrate. By tilting the substrate in an angle, a thickness gradient of material could be obtained[35]. The thickness gradient depends on the material and the sputtering parameters.

3. METHODOLOGY

3.1. Nanoparticles as solder

3.1.1. Synthesis of tin nanoparticles

Kwon et al.[55] and Yong[41] were successful in synthesizing tin nanoparticles via a wet chemistry route. They use different approaches to the synthesis, but common ground is between them. For preparing the tin metal nanoparticles , Kwon et al., used anhydrous $SnCl_4$, hydrobenzamide (as surfactant) and $NaBH_4$ (as reducing agent) dissolved in 1,2- dimethoxyethane. Yong used $SnCl_4$, 1,10 phenanthroline (as surfactant) (phen: SnCl4 = 1:1) and $NaBH_4$(as reducing agent), using water as solvent. Jiang et al.[56] stated that 1,10 phenanthroline is a very effective capping agent for tin nanoparticles and its alloys. Then the scientist cleaned, usually with ethanol or acetone, centrifuge and vacuum dry the resulting mixture to recover the nanoparticles.

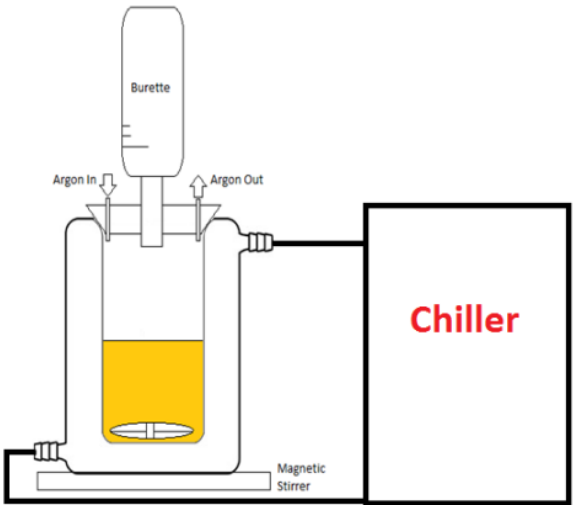

Figure 17: Experimental setup for the tin synthesis

The experimental setup used to control the parameters of the synthesis is shown in Figure 17. The atmosphere for the reaction is inert owing to the presence of argon flowing through the reaction chamber as well as the burette. The reaction chamber is a jacketed beaker connected to

a Thermo Scientific Neslab RTE7 chiller to control the temperature at which the reaction occurs. A magnetic stirrer is used for the homogenization of the solution.

An aqueous solution of 100ml 0.1 M $SnCl_2*2H_2O$ was prepared in glyme (1,2 dimethoxyethane) and 2g of 1,10-phenanthroline were added to the solution (for a 1:1 molar ratio of phen:$SnCl_2$). The solution was then added to the reaction chamber and magnetically stirred for 10min at a controlled temperature of 20°C. A 100 ml suspension of 1.5g sodium borohydride in glyme was then added to the reaction chamber and held for 1 hour. The resulting solution was then centrifuged at 9,000RPM for 5minutes, and then re-dispersed in ethanol for cleaning. This process was repeated three times and then the samples were vacuum dried. All the chemicals were supplied by Sigma–Aldrich.

3.1.2. Development of flux and solder paste

A flux medium is needed when two surfaces are to be joined in order to chemically clean the interfaces as well as the particle's surface. The flux for our system was developed in parallel with the Sn nanoparticle's synthesis. For simplicity reasons, and lack of nanoparticles at the initial stage, the preliminary tests were done using Sn microparticles (1-5μm) for solder paste preparation. Flux components were chosen based on a literature review. Ethylene glycol is one of the most common solvent used in commercial fluxes[57]. The active components of the flux will vary according to the obtained results, the most widely used chemicals are rosin (regular or mildly activated) or some type of organic acid with a carboxylic group. The first approach was to use fluxes based on 90, 95 and 99% w/w of ethylene glycol with additions of citric acid and hydrogenated rosin. Metallic Sn micropowder was added to the flux in the range of 85-95% w/w in order to have qualitative observations of the resulting sintered paste upon which a decision

could be made. The second approach to the flux formulation included the use of ethylene glycol and glutamic acid hydrochloride at different compositions by weight. The components for each flux were weighted for the specific quantities and then mixed and homogenized. The metallic powder was weighted and the required quantity of flux was added to it.

3.2. Tin whiskers

3.2.1. Initial Stage

Combinatorial libraries can provide a convenient, compact, and powerful platform for scientific research. When properly designed, the library amplifies the scientific effectiveness of sample preparation and allows researchers to consider "spaces" rather than individual "points"[35]. The procedure to fabricate the gradients of materials across the libraries will be detailed in this section. The overlap of different gradients will be used to obtain a range of possible compositions over the sample.

The samples consist of a mirror finished Cu substrate electroplated with matte and bright Sn, the main difference between them is the grain size and according to some researchers it makes an impact on the growth of wiskers. The thickness of the Sn film is about 15µm as measured from metallographic characterization using an optical microscope.

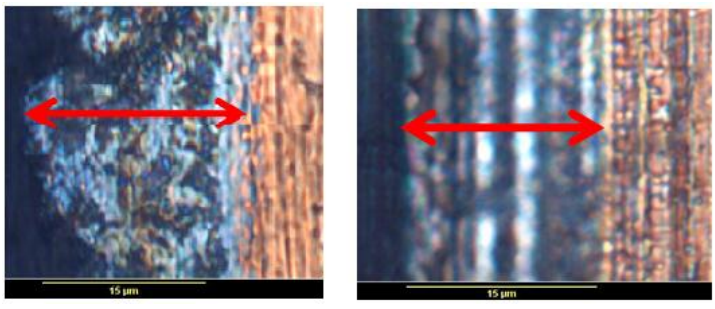

Figure 18: Cross-section of the matte and bright tin electroplated on the Cu substrate.

To obtain the gradients of the other elemental additions, in this case Ag, Ni and Cu, the use of an atomic deposition technique was required, i.e. Magnetron Sputtering. The sputtering chamber was equipped with three magnetrons; one of which is specially designed for magnetic materials (nickel) that can hold a two inches target whereas the other two are designed for one inch diameter targets (silver and copper). The stainless steel chamber was connected to two vacuum pumps, a mechanical pump and a turbomolecular pump. The power supply was an Advance Energy MDX 500 and an ENI RPG 50. The mass flow controller was a MKS type 246 and the pressure reader was a 307 vacuum gauge controller connected to a MKS PDR C 2C. From geometrical arguments, the chamber is poised to produce gradients as schematically shown in Figure 19.

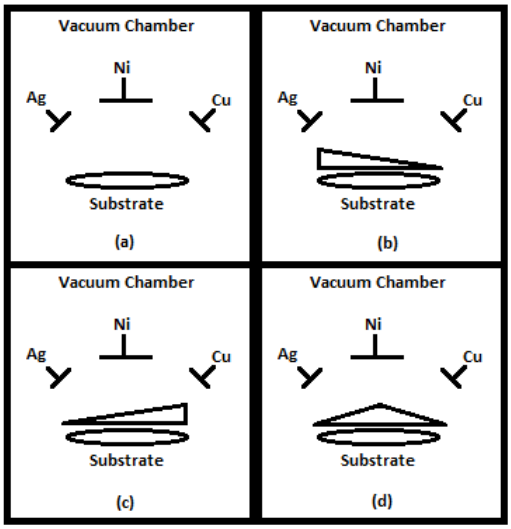

Figure 19: (a) Schematic of the Sputtering Chamber (b) Schematic for the sputtered gradient of Ag (c) Schematic for the sputtered gradient of Cu (d)Schematic for the sputtered gradient of Ni

Characterization of the deposited gradients required an independent test with each magnetron before any co-sputtering could be attempted. For these tests, a silicon wafer was used as a substrate and placed along the deposition line of each gun. Using the following conditions; power of 50W, back pressure of $5x10^{-5}$Torr and a deposition pressure of 5mTorr, three silicon sub-

strates were independently sputtered with Ni, Ag and Cu for 5minutes. The thickness gradient was characterized with a KLA Tencor Alpha-Step IQ Surface Profiler.

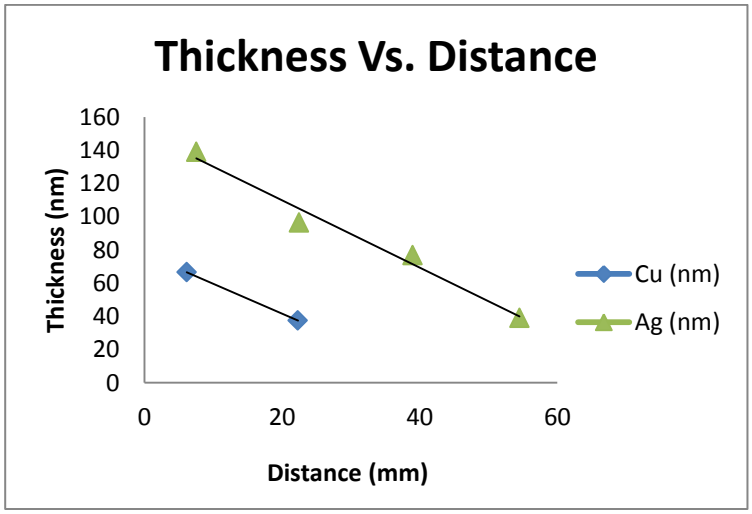

Figure 20: Thickness gradient of Cu and Ag. The origin (0) is the point closer to the target, at the left for Ag and at the rigth for Cu.

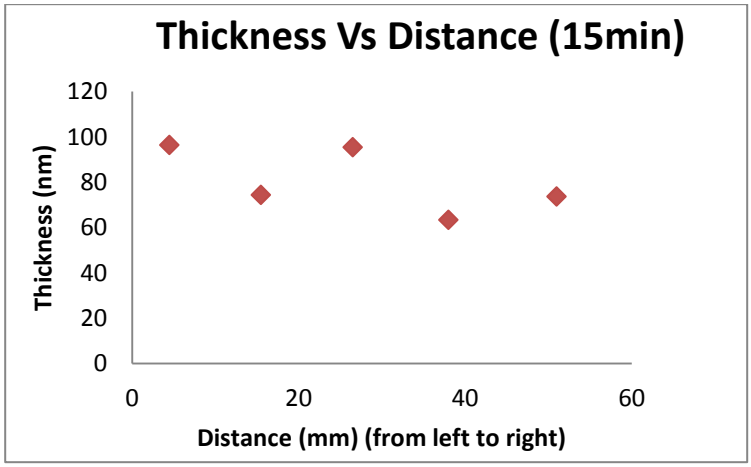

Figure 21: Thickness gradient for Ni.

Ag and Cu will be co-sputtered which implies that both will have the same deposition time. Figure 20 shows the thicknesses profile for a five minutes deposition from where it was observed that the deposition rate for copper is less than for silver. A deposition time of 30 minutes was selected so that the final maximum thicknesses, extrapolating from our graph, for the Ag will be 840nm and for 420nm the Cu. The copper line shows two points owing to the fact

that the other experimental conditions yielded thicknesses too thin for the profilometer to measure. For nickel, a deposition time of 70 minutes was selected in order to achieve a final maximum thickness of approximately 443 nm.

As fabricated samples are shown in Figure 22, where a mask was placed over the sample to form discrete points in which the alloy compositions will be measured.

Figure 22: As fabricated sample (center image) using the mask depicted in the far right.

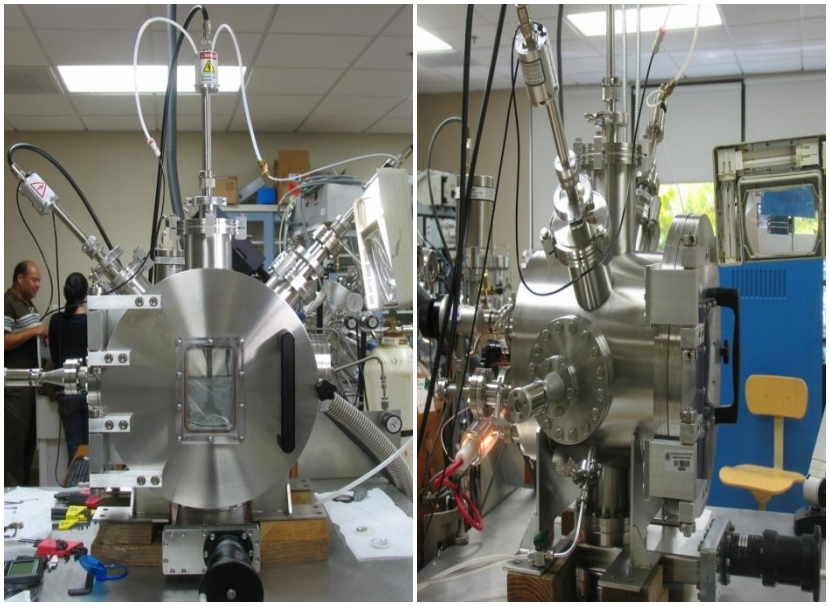

Figure 23: Experimental set-up and laboratory equipment.

The resulting test specimens have a layered structure following the deposition stage; therefore a reflow profile is needed in order to mix all the elemental components together.

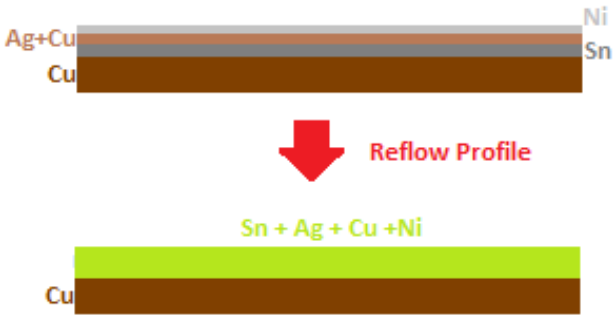

Figure 24: Schematic sample before and after reflow profile aimed at mixing the constituents.

A recommended Pb-free reflow profile is shown in Figure 25, the intention is to melt the tin and force the other materials to mix. A similar profile was developed at our laboratory by calibrating an Omegalux LMF 3550 oven. The actual profile is shown in Figure 26.

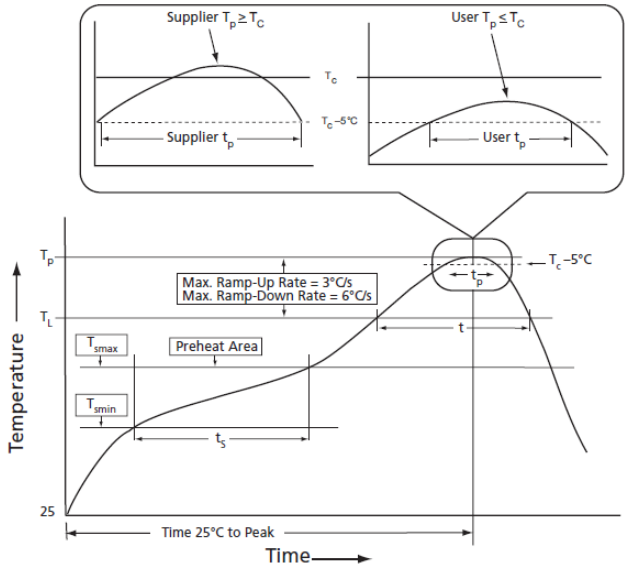

Figure 25: Recommended lead-free reflow profile[58]

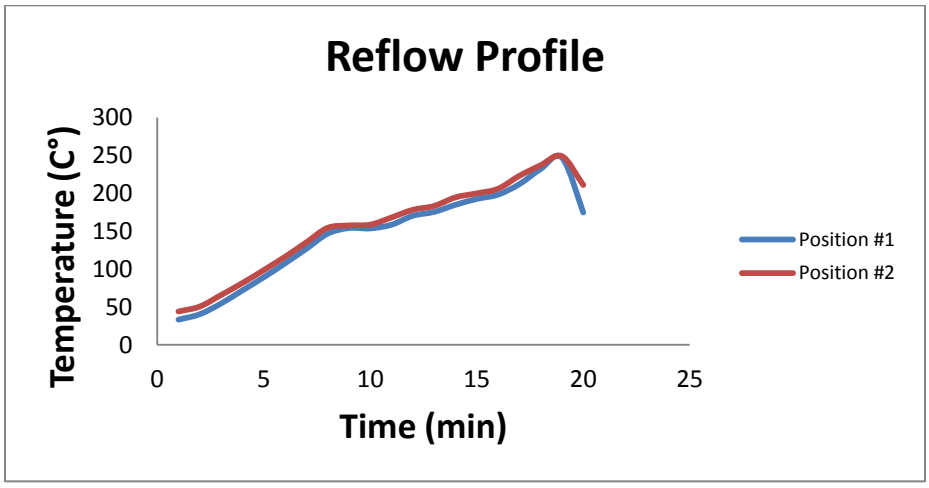

Figure 26: Actual profile performed on the samples.

Environmental testing, to assess the growth of Tin Whiskers, is required in order to accelerate the growth mechanisms that the scientific community had agreed upon. There are a few organizations in charge of developing standards, e.g. JEDEC, JEITA, IEC, among others. In a review paper published by Osterman et al.[18], they summarized some of the most used standards to assess the growth of whiskers. The *IEC60068-82-2 High Temperature/ Humidity Test* was cho-

sen as the standard to follow with the specific test condition of 55^0C and 85% RH for 2000 hours which has been performed using a BTL-433 ($4ft^3$) bench-top temperature and humidity chamber. The characterization process is by means of scanning electron microscopy (SEM Jeol JSM 6360) equipped with EDS.

3.2.2. Refined approach

Copper squares (about 25 mm^2) plated with Sn were arranged over another substrate that served as a carrier or holder (Figure 27).

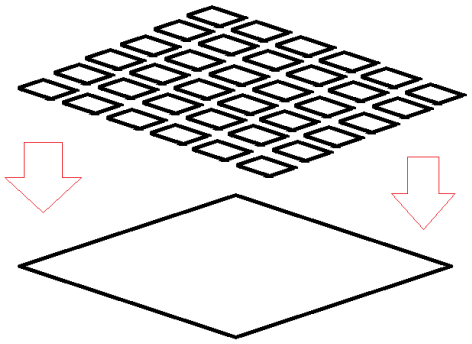

Figure 27: Schematic of the sample preparation

The sputtering process was performed over the grid of squares, thus helping on the characterization process owing to the fact that better defined, discrete areas were obtained. These individual squares represent a test condition that can be characterized independent from others; therefore a better control of the composition and whisker occurrence is possible. Pure Sn plated samples were used as control where they followed the same reflow profile and aging of the sputtered samples.

The electroplating process used to cover the copper substrates with Sn consisted of the following steps:

1. Add 430mL of Di-water to a 600mL beaker
2. Add 25µL of sulfuric acid.
3. Add 13.8g of tin sulfate.
4. Stir the mixture for about 5-10min.
5. Add sodium hidroxide until the solution reaches a pH of about 3.8.
6. Centrifuge the solution to eliminate the precipitate.
    a. 5min at 9000RPM
7. Filter the solution using a Büchner flask, a funnel and a glass fiber filter.
8. Add 14mL of tetraethyleneglycol and 1.8g of citric acid. Stir for 5min.
9. Clean the copper surface with a mix of acetic acid and NaCl and scrub it with a brush. Then, rise with Di-water and insert it in acetone overnight. Rinse and soak the samples in a 10% solution of nitric acid.
10. Start the electroplating process using 0.9A. Use 10min intervals, cleaning the surface with Di-water between the depositions.

The thickness of the electroplated tin was characterized using cross-sectioning and optical microscopy obtaining about 3µm, as shown in Figure 28.

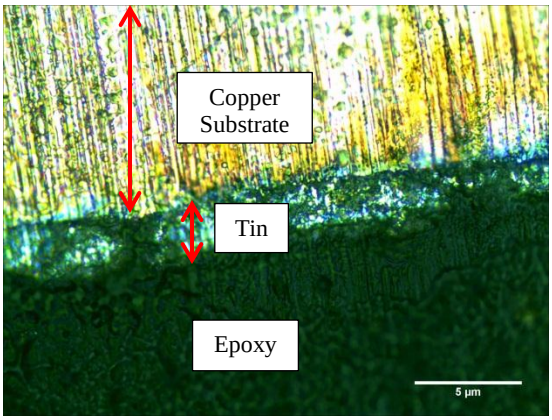

Figure 28: Cross-section of the Cu substrate electroplated with Sn

The Cu square substrates, plated with Sn, were placed over the holder having the arrangement shown in Figure 29. The top of the sample, the side with the notch, will be closest to the Cu target and the other side to the Ag during the co-sputtering process.

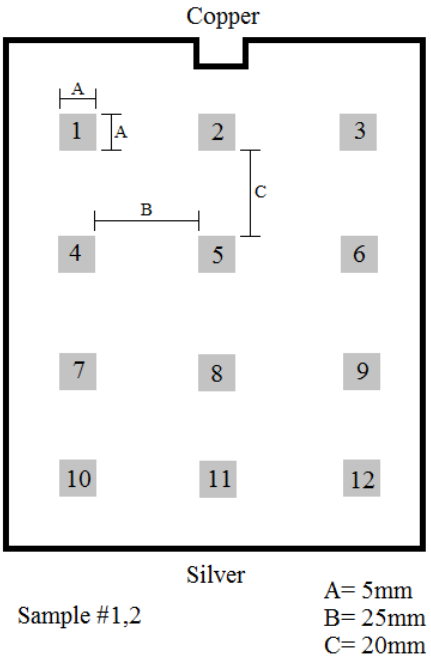

Figure 29: Sample arrangement

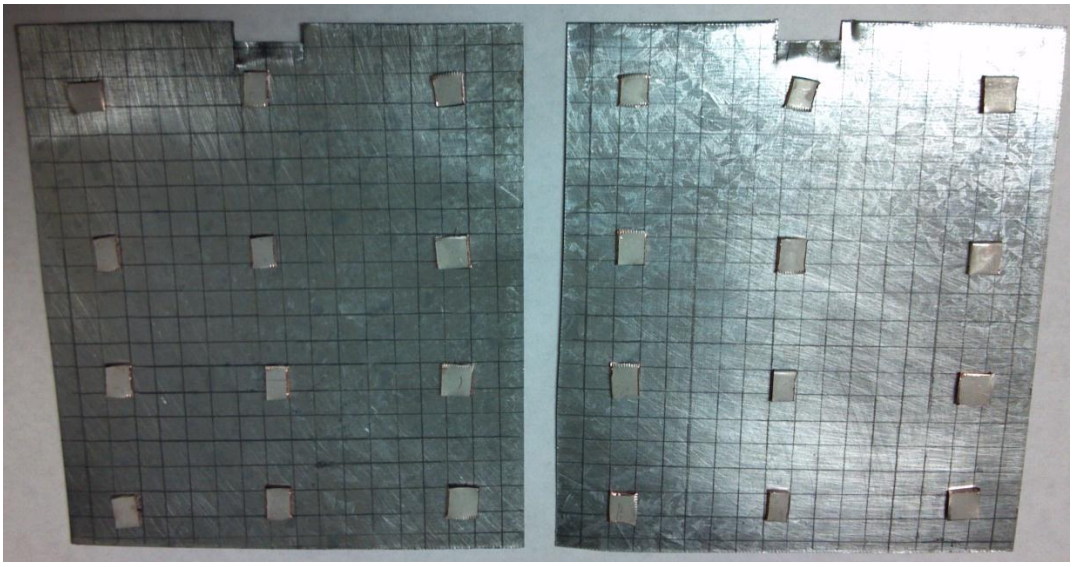

Figure 30: Actual sample before sputtering process.

The gradients were produced over the samples using the previously described technique of magnetron sputtering. In this case Ag and Cu were added on top of the Sn plated Cu substrate. The same equipment was used to process these samples. From geometrical arguments, the chamber is poised to produce gradients as schematically shown in Figure 31.

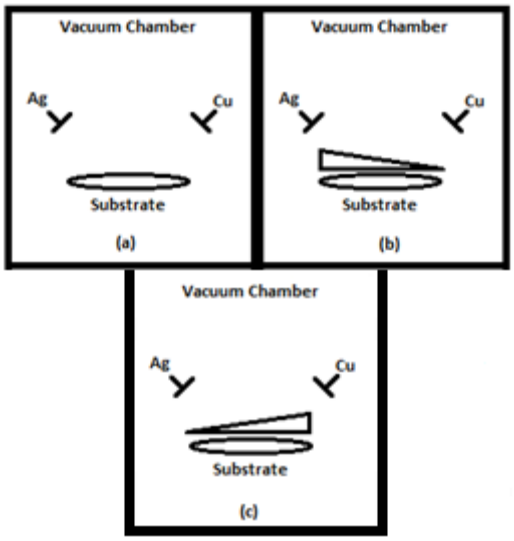

Figure 31:(a) Schematic of the sputtering chamber (b) Schematic for the sputtered gradient of Ag (c) Schematic for the sputtered gradient of Cu

An independent test was performed in order to characterize the optimal sputtering conditions for the samples. The thickness was characterized with a KLA Tencor Alpha-Step IQ Surface Profiler. Ag and Cu are to be co-sputtered which implies that both will have the same deposition time of 5minutes. Extrapolating from our tests, the required power to deposit 500nm of Ag in 5 min is 500W and 50W for depositing 100nm of Cu, on the area closer to the magnetron gun that supposed to be the thicker. Other parameters were a back pressure of 6.6×10^{-6} Torr and a deposition pressure of 20mT.

As fabricated samples are shown in Figure 32, each square is a discrete point in which the alloy compositions will be measured.

Figure 32: Samples after Ag-Cu co-sputtering

A reflow profile was needed in order to mix all the elemental components together. Using the Omegalux LMF 3550 oven, a reflow profile with a longer dwell time above Sn liquidus was developed. The atmosphere wasn't controlled through the reflow profile.

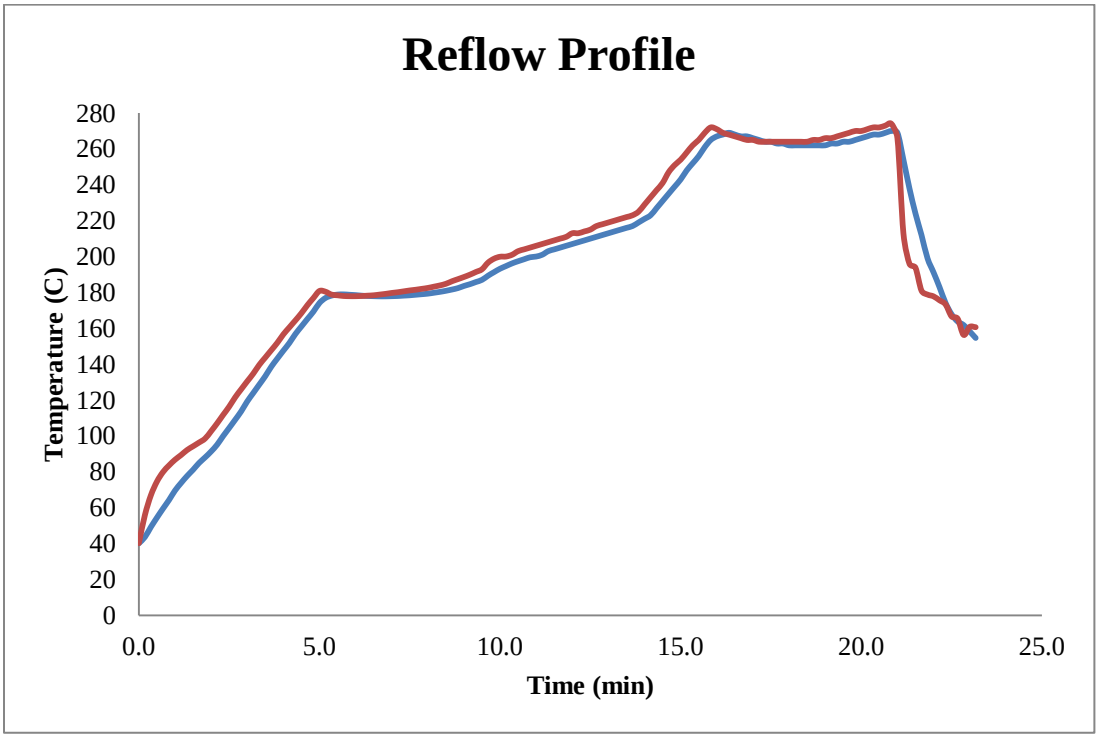

Figure 33: Reflow profile used to mix the elemental components

The same standard, *IEC60068-82-2 High Temperature/ Humidity Test*, was used to test for whisker growth. Using a BTL-433 ($4ft^3$) bench-top temperature and humidity chamber the test conditions were guaranteed. The characterization process was by means of scanning electron microscopy (SEM Jeol JSM 6360) equipped with EDS.

4. RESULTS AND DISCUSSION

4.1. Nanoparticles as Solder

4.1.1. Synthesized Sn nanoparticles

X-Ray diffraction (XRD) was used to characterize the results from the synthesis. Figure 34 shows the XRD pattern for the dried residues from the synthesis. The intensity of the peaks was compared with possible matches: Sn(a), NaCl(b), SnO(c), and SnO_2(d). A mixture of tin, tin oxide, and tin dioxide was obtained from the synthesis; also NaCl was detected as a product of the reaction. From Figure 34(a) it can be seen that the more intense peaks matched those from Sn.

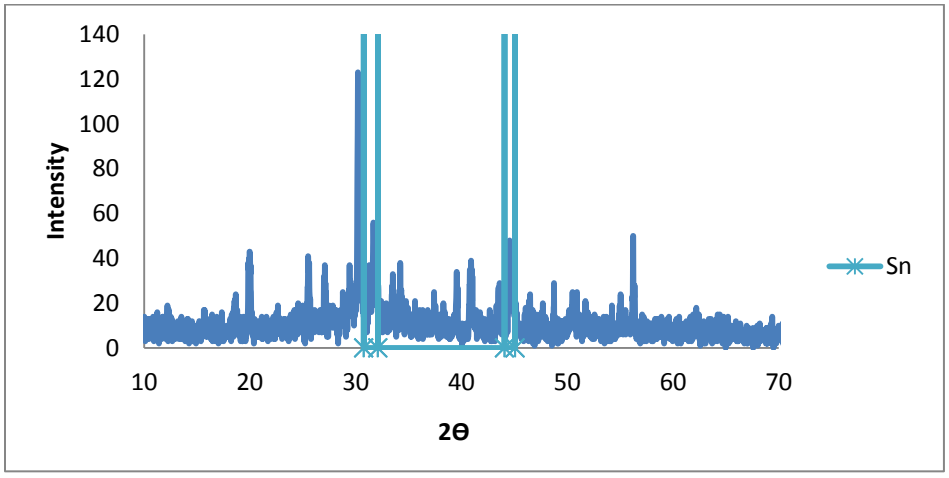

(a)

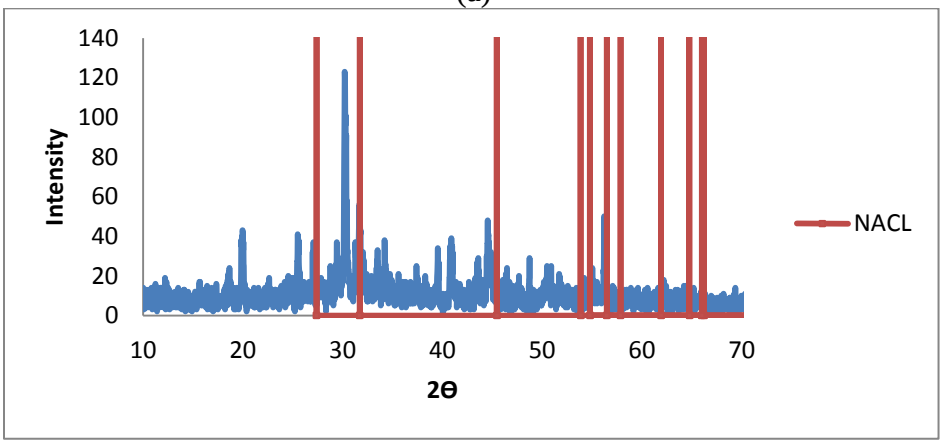

(b)

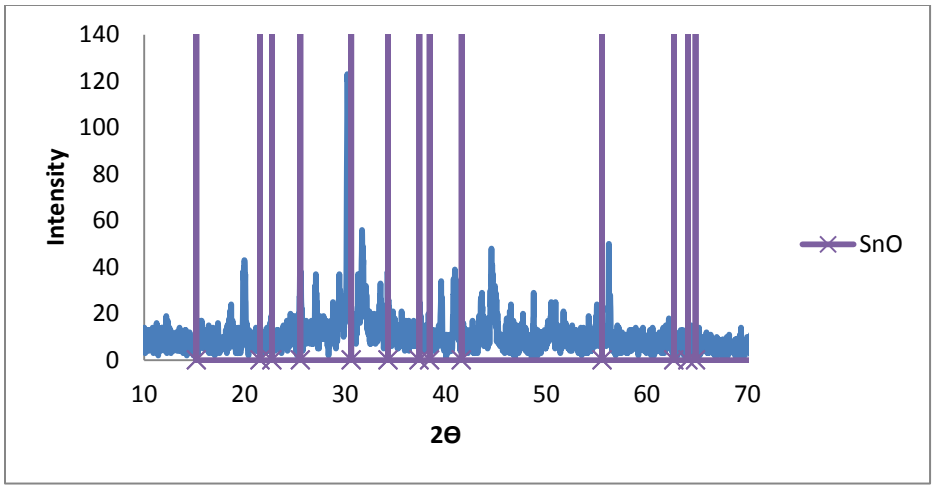

(c)

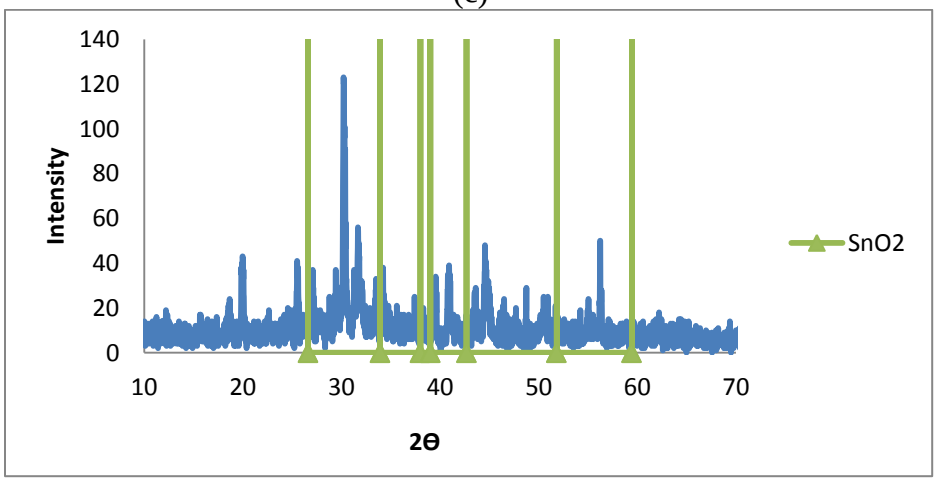

(d)

Figure 34: XRD patterns for the obtained Sn nanoparticles compared with (a) Sn (b)NaCl (c)SnO (d)SnO_2

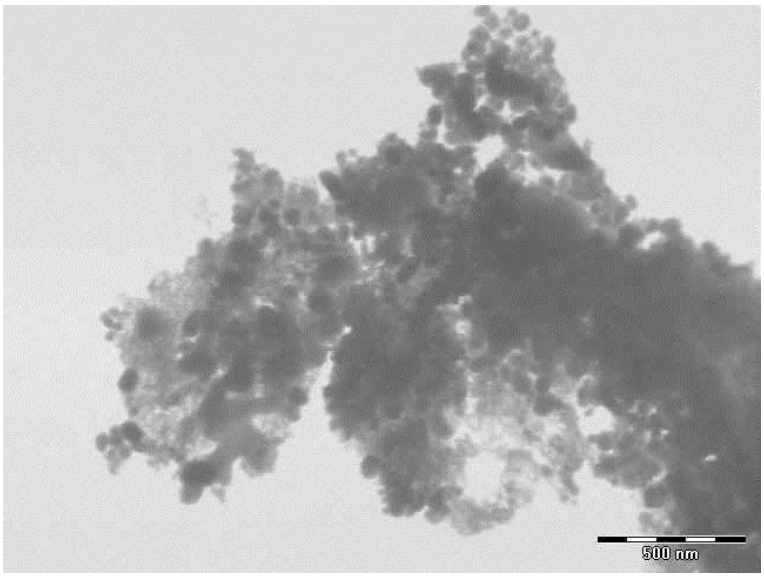

Figure 35: TEM image of the Sn nanoparticles

Figure 35 shows a TEM image for the synthesized Sn nanoparticles. Average particle sizes of 30 to 60nm in diameter were recovered from our synthesis.

For the preliminary tests, Sn microparticles were used for the qualitative characterization of the solders formulated with the different fluxes developed during this stage. The first step of the preliminary tests involved the use of 90, 95 and 99 wt% ethylene glycol and the addition of citric acid and hydrogenated rosin to prepare the flux. The system was mixed into a solder paste containing from 85 to 95 wt.% of the metallic tin microparticles. The temperature for these tests was 250ºC to guarantee the full melting of the tin precursor (melting point of Sn is 232º). Qualitative results from the obtained solder showed that the flux was unable to remove the oxides from the surface of the microparticles as suggested from the unwetted substrate; furthermore the rosin residues were burnt on the samples impeding any joint formation. Figure 36 shows some of the results from the tests, black and grainy residues were appreciable.

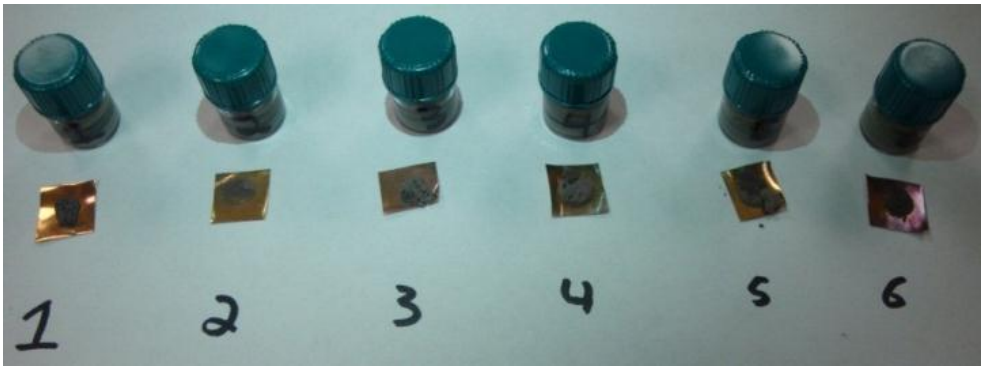

Figure 36: Some results from the preliminary solder paste test (ethylene glycol, citric acid, and hydrogenated rosin).

A second attempt for the flux formulation was aimed at improving the oxide removal capability from the surface of the microparticles. Ethylene glycol was mixed with glutamic acid hydrochloride (from 5 to 50 wt.% concentration) to use it as the flux medium. A solder paste was developed by adding from 85 to 95 wt.% metallic tin microparticles and tested at a reflow

temperature of 250ºC. Figure 37 shows some of the test results for these solder pastes. Qualitative observations demonstrated that the best combination of metallic powder-flux is 85 wt.% Sn (microparticles) with 15wt.% flux; where the flux itself contains 50 wt.% ethylene glycol and 50 wt.% glutamic acid. Figure 38 shows an image for this best combination.

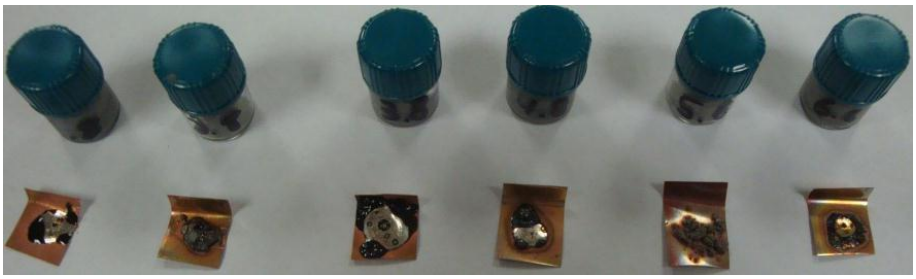

Figure 37: Resulting solders from the ethylene glycol and glutamic acid flux

Figure 38: Best solder paste embodiment.

From the aforementioned set of experimental trials, the best paste formulation was selected for performing tests with the synthesized Sn nanoparticles. Using the particles from our synthesis, a solder paste was developed using the best-known flux as defined in the previous section, i.e. ethylene glycol with glutamic acid. As reported from XRD patterns, it is known that some oxides will be present, therefore the flux should be able remove them from the surfaces. In our nano-paste formulation, the dried product from the synthesis was mixed with the flux using a ratio of 25wt% nanoparticles and 75 wt.% flux. The particle size difference between the microparticles and the nanoparticles represents an increase in surface area (as high as $1/d^2$, for spheres (Particle Surface Area– A Critical Metric in the Characterization of Suspensions David Fairhurst, PhD.)). The paste preparation involves the addition of a liquid phase to produce a non-

Newtonian suspension. When the particle size is decreased, the quantity of liquid that will be required to wet the surface of the particles increase due to the fact that the surface area exposed is bigger. The outer surface of the particles is what interacts with the flux. Reflow was performed on copper test coupons where the solder paste was deposited on top. Temperatures ranging from 197ºC to 217ºC were used to process the samples. Local substrate temperature was measure by the direct reading of an external thermocouple that was attached to the surface of the test coupon. The resulting coupon exhibited a tinned surface where good wetting of the surface was observed, as shown in Figure 39. SEM and EDS was used to characterize the surface of the copper coupons.

Figure 39: As reflow sample of synthesized Sn-nanoparticle paste on top of a Cu substrate.

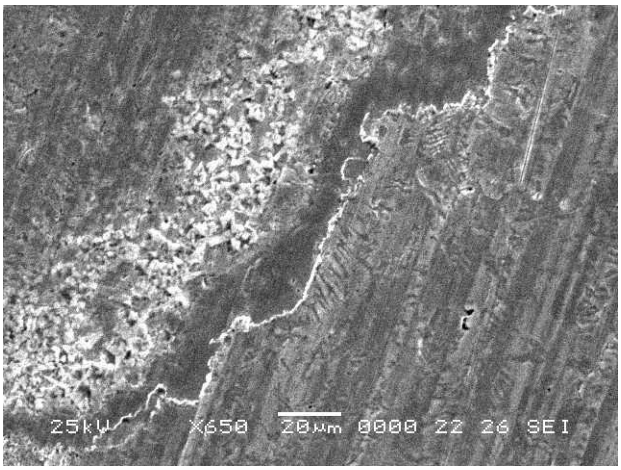

(a)

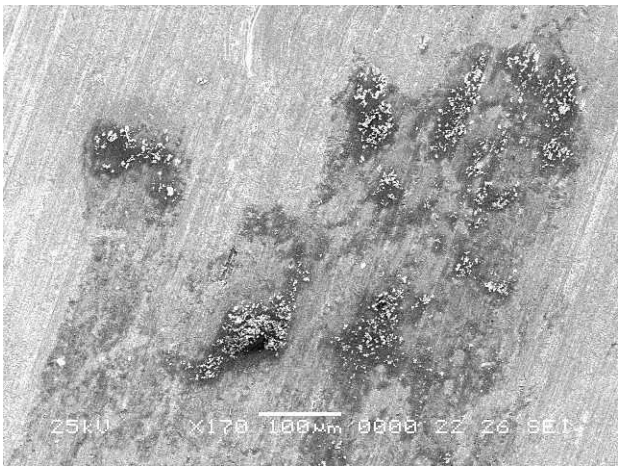

(b)

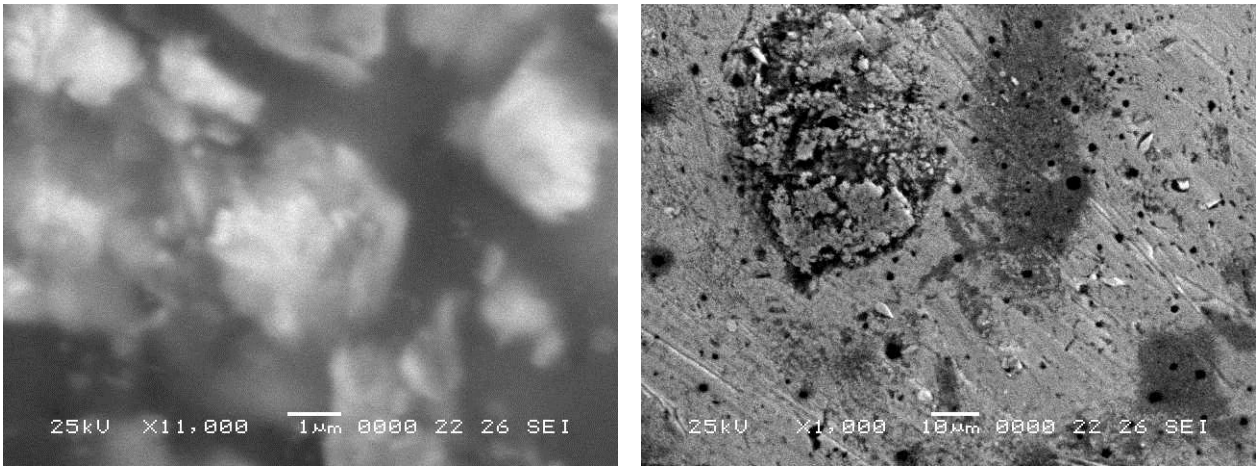

(c) (d)

Figure 40: SEM images for the test coupons: (a) 205°C-interface copper-tin (tin on the right) (b) 205°C-surface defects (c) 205°C-surface defects at x11K (d) 217°C-Solder bump surface

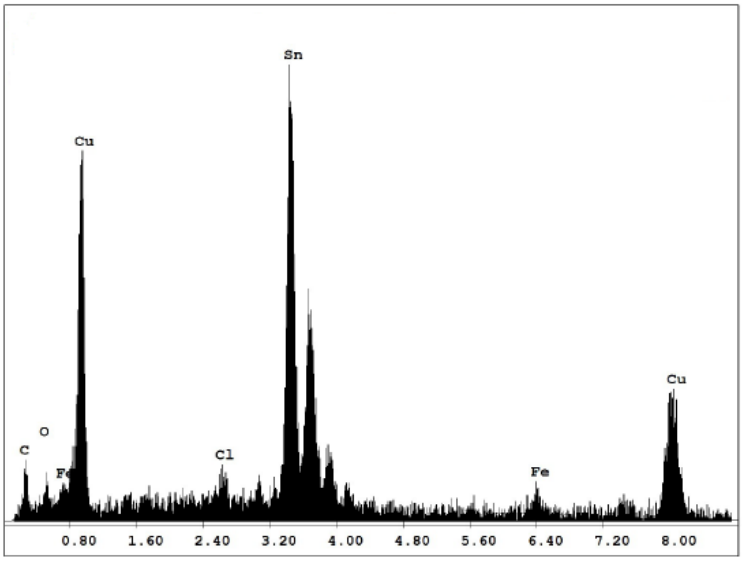

Figure 41: EDS Spectrum for the area shown in Figure 40d

SEM images in Figure 40 showed the surfaces obtained after the low temperature reflow process. EDS confirmed the presence of Sn over the Cu substrate, as shown in Figure 41. Reflow temperatures were approximately 30-40°C below the melting point of tin, therefore in principle it has been demonstrated that using nanoparticles the processing temperature of such paste can be substantially reduced. However, due to the large amount of flux relative to metal within the paste it

was not possible to obtain enough volume of metal within our coupon thus resulting in a limitation for the formation of a sound solder joint for device attach on a SMT process. The organic surfactant also played a critical role since it acts against the coagulation mechanisms needed for the surface melting required for the process. It has been theorized that increasing the metal load to ~80% or more should eliminate this limitation, but our current flux/nanoparticle material cannot be mixed in such a high metal content ratio without losing the necessary rheology needed on a solder paste. In response to this observation, the usage of commercially available Sn nanoparticles was introduced in order to prove our hypothesis and demonstrate the proof-of-concept.

4.1.2. Commercially available Sn nanoparticles

Commercially available Sn nanoparticles were procured from SSnano Corp. The nanoparticles specifications are: 99.9% of purity, an average particle size below 100nm, spherical particles without surfactant and a specific surface area of approximately $7m^2/g$.

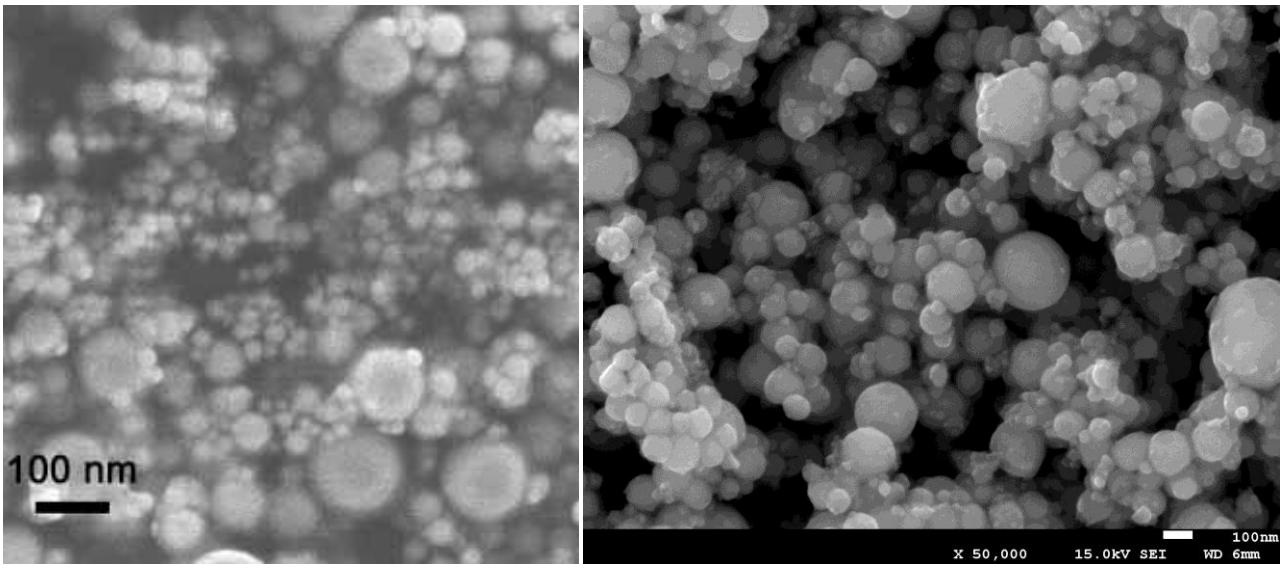

(A) (B)

Figure 42: SEM images of the Sn nanoparticles.

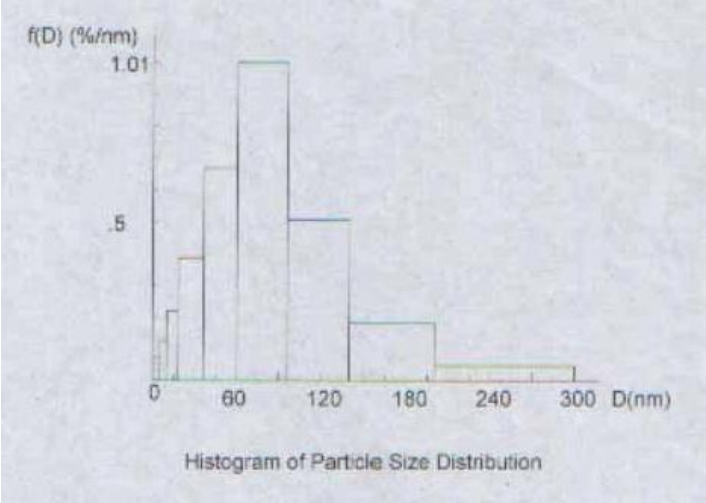

Figure 43: Particle size histogram provided by the supplier.

Figure 42 shows SEM images from the commercial nanoparticles; (A) is an image provided by the supplier and (B) is an image taken at a LMC laboratory. It can be shown that the particles are spherical and that, mostly, they are about 100nm in diameter. Figure 43 shows a particle size histogram of the nanoparticles having an average diameter of 94.6nm.

In order to avoid oxidation during the sintering process, the flux developed with the microparticles (50wt.% ethylene glycol and 50wt.% glutamic acid hydrochloride) will be used to prepare the paste. After some testing, the best embodiment for the paste was found; 60 wt.% Sn nanoparticles and 40 wt.% flux.

At this stage of the investigation we focused on the fabrication of test specimens both for qualitative observations as well as quantitative experiments that included mechanical testing and micrographic analysis. To prepare the samples, Cu foils were joined by depositing solder paste, via stencil printing, after processing them with a reflow process. Figure 44 shows the reflow profiles used to heat up the sample, temperature was measured on top of the Cu foil substrate with an external thermocouple. When using 180°C for processing, the samples didn't hold up to

the cleaning process of sonication in ethanol or acetone, thus this processing temperature was ruled out for all testing.

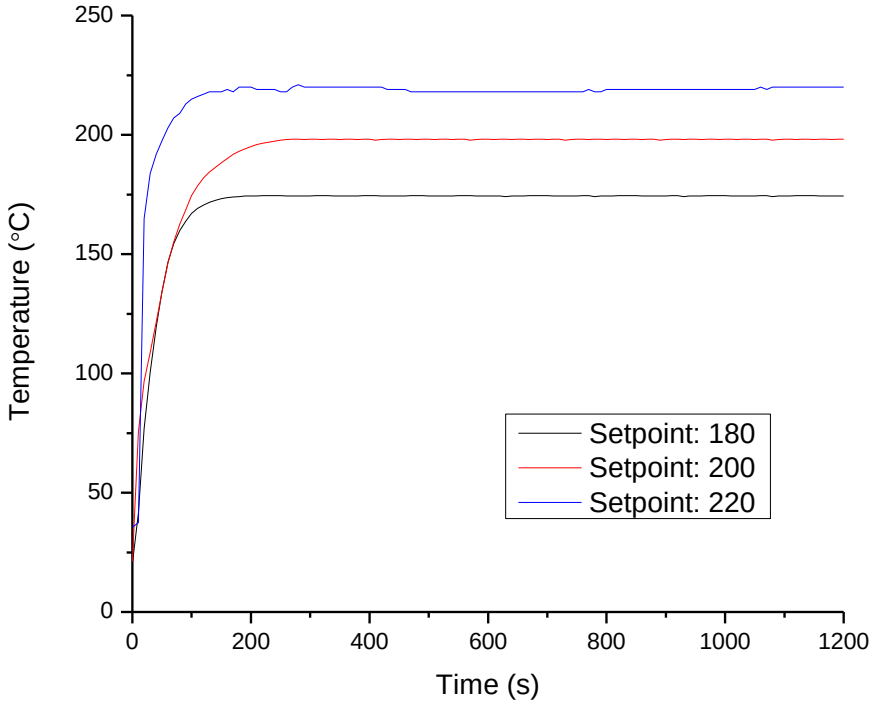

Figure 44: Reflow profiles measured at the surface of the samples

Lap shear tests were performed in order to characterize the mechanical strength of the joints. Two Cu foil strips were cut to 2", and then a stencil was used to print a square of paste in the tip of one strip with a length of 0.4". Figure 45 shows a schematic of the specimen used for mechanical testing. The tension machine used is a Mark 10- ESM301L, shown in Figure 46.

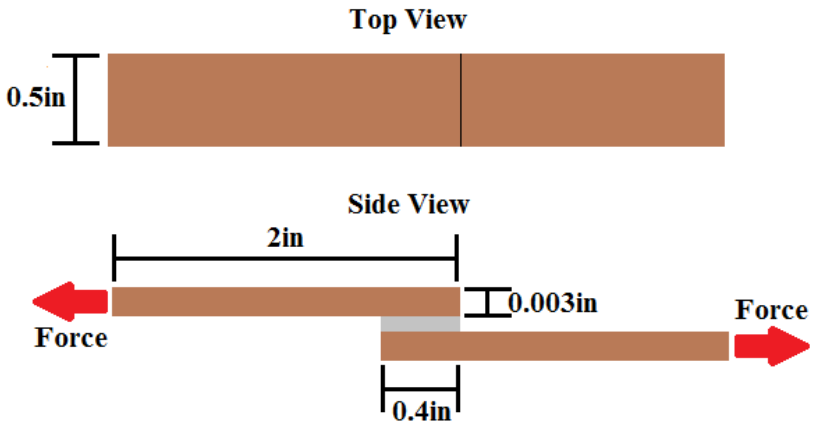

Figure 45: Schematic of the lap shear test specimen

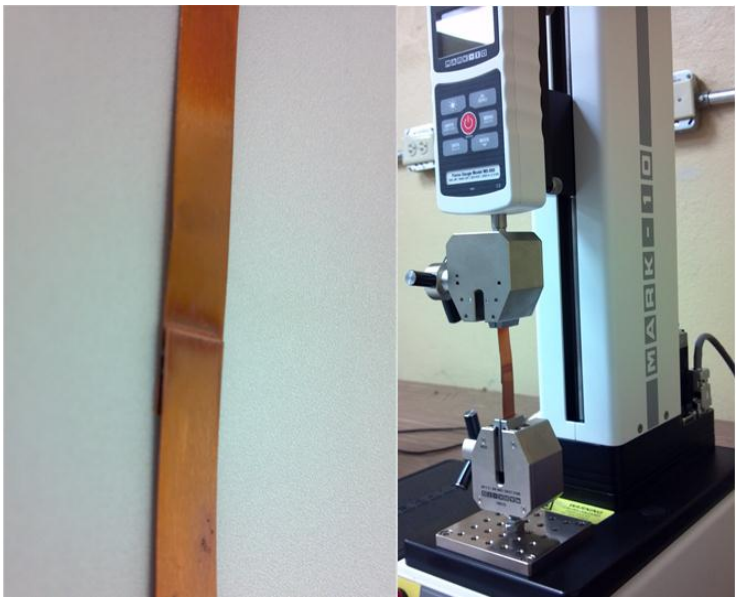

Figure 46: Actual sample and machine used for mechanical testing the joint

Table 1: Peak force data for specimens processed at different times and temperatures.

	200°C			220°C		
Time (min)	Avg. Force (Lbf)	Std Deviation	Shear strength (psi)	Avg. Force (Lbf)	Std Deviation	Shear strength (psi)
10	30.25	5.32	151.3	36.88	1.89	184.4
20	35.06	2.91	175.3	35.42	2.67	177.1
30	34.42	3.89	172.1	34.8	2.62	174

Ten data points were collected for each condition as presented in Table 1. The average and standard deviation were also calculated. An attempt to correlate the microstructure of the resulting attach material to the mechanical response was performed.

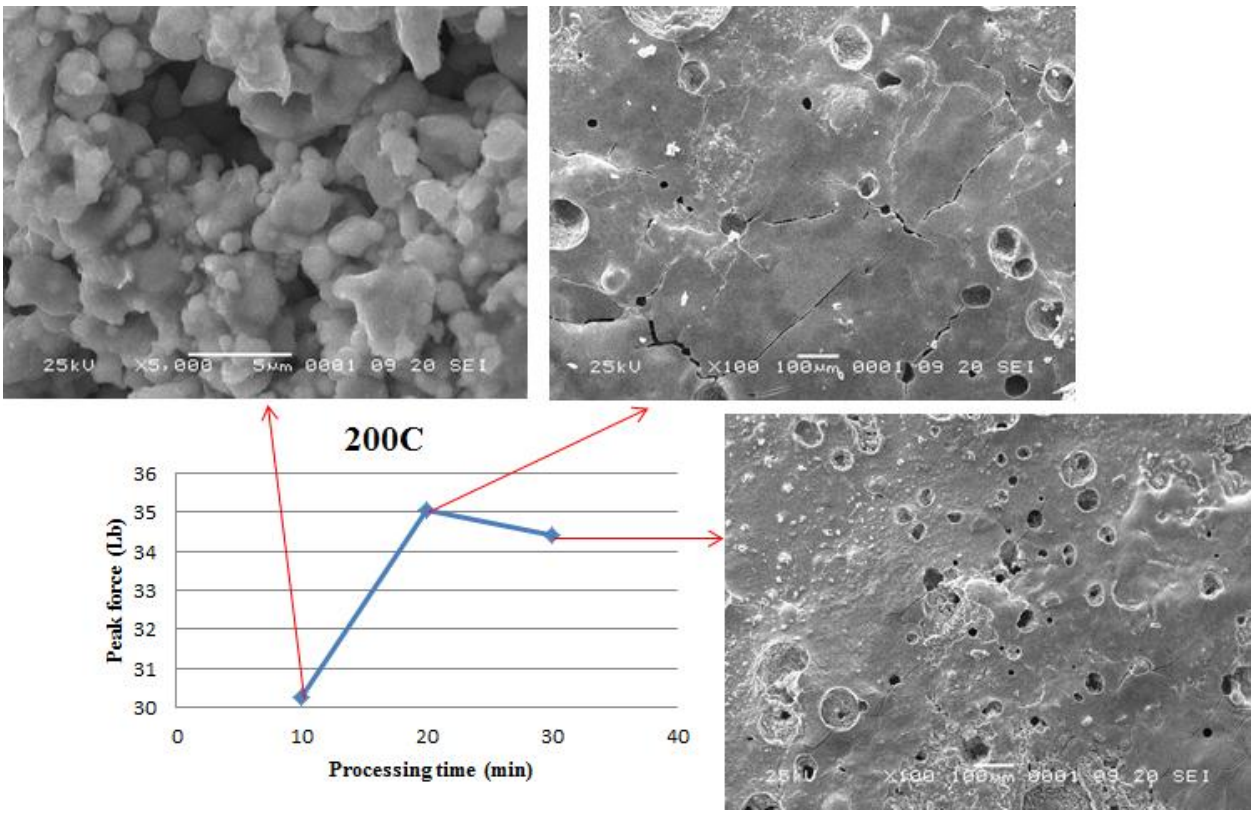

Figure 47: Microstructure-peak force characterization evolution for samples processed at 200C for various holding times.

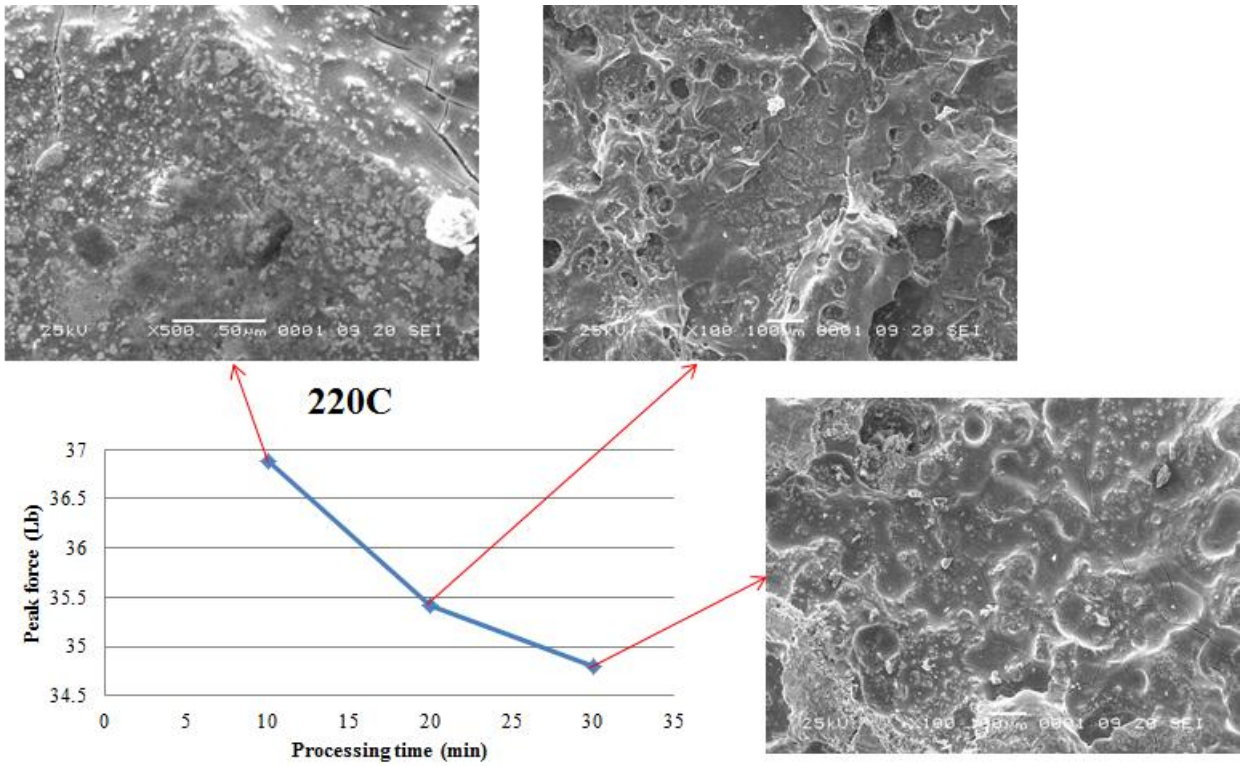

Figure 48: Microstructure-peak force characterization evolution for samples processed at 220C for various holding times.

At 200°C, samples were processed for 5, 10, 20 and 30 minutes. A stencil with a circular aperture of about 3mm in diameter was used to deposit the paste onto the Cu substrate. After reflowing the samples at the specific profiles, i.e. the two peak temperatures and the three processing times, the specimens were cleaned with ethanol using a 3 minutes sonication process. The sample processed for 5 minutes didn't hold up the sonication, the attach material (solder) disintegrated and got suspended into the ethanol. Figure 47 shows a relation between the measured peak force and the microstructure that resulted from the sintering process for the different experimental conditions. At 10 minutes, the sintering process had begun forming necks between adjacent nanoparticles resulting in a stronger structure than the 5 minutes sample that didn't hold up. At the 20 minutes mark the final stage of the sintering process was reached as evidenced by the formation of a microstructure that resembles a bulk material, though still showing some porosity which is intrinsic of the sintering process. After this point the samples started to oxidize as

time was increased because no more flux was available to protect the metal. At 30 minutes, the structure showed some pitting corrosion, but in general the structure is similar exhibiting pores and grain boundaries. Figure 50 depicts the EDS pattern for each set of parameters revealing the increment of the oxygen peak as time increases. Also, contamination of Cl and C is shown in the patterns. The source of contamination is the residues from the flux after reflow. At 200°C, the shear strength varied from 150psi (1.03MPa) to a maximum of 175psi (1.21MPa) for the sample processed at 20 minutes. Shear strength values for the eutectic Sn-Pb alloy ranging from 9.2 to 50 MPa have been published. Common Pb-free solders, as Sn-3.5Ag, Sn-0.7Cu, Sn-3.8Ag-0.7Cu and Sn-3.5Ag-3Bi (by weight), have shown values ranging from 9.2 to 49 MPa[59]. Comparing the shear strength values can be seen that the mechanical properties of the developed nano-solder are well below the common used alloys.

Similarly, reflow profiles with peak temperature of 220°C and processing times of 5, 10, 20, and 30 minutes were used. In this instance, samples processed for 5 minutes hold up to the cleaning process using sonication, but lap shear tests were not performed on this condition.

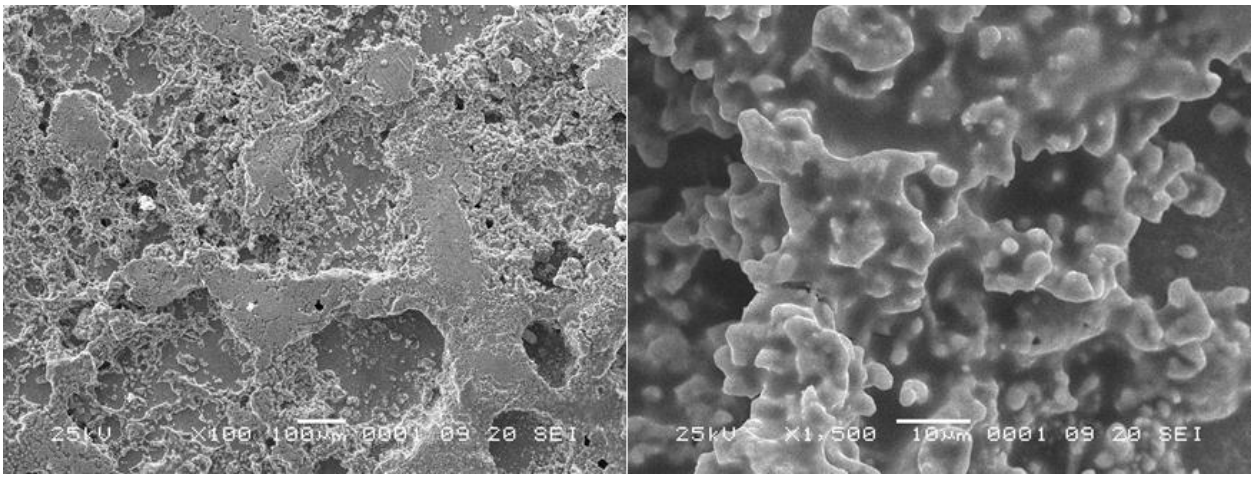

Figure 49: SEM images for a sintering process of 5 minutes at 220°C

Figure 49 shows the typical structure of the initial stage of sintering where high porosity and necking between adjacent nanoparticles is evident. Figure 48 shows the relation between the microstructure and the peak force for these samples processed at 220°C. At a processing time of 10 minutes the final stage of sintering is almost completed as evidenced from the formation of a continuous body with a high degree of densification. After 20 minutes the incremental oxidation of the samples became evident from the inspection. Processing times longer than ~10 minutes are known to be detrimental for flux, where activators are basically consumed and no longer capable of providing any reducing or protecting function. Figure 51 show the evolution of the oxygen peak using an EDS pattern. Table 2 shows the oxygen weight percentage for each case, contrasting with the peaks shown in the patterns and the observations on SEM images. As time and temperature increases, the oxidation level increases. As seen from the mechanical data, the shear strength varied from 174 to 184psi which is not a very significant change, however its deterioration with time could be attributed to the higher oxidation. At 220°C the oxidation process started earlier because of the higher temperature. From the EDS it was confirmed that contamination (Cl) from the flux is present on the samples.

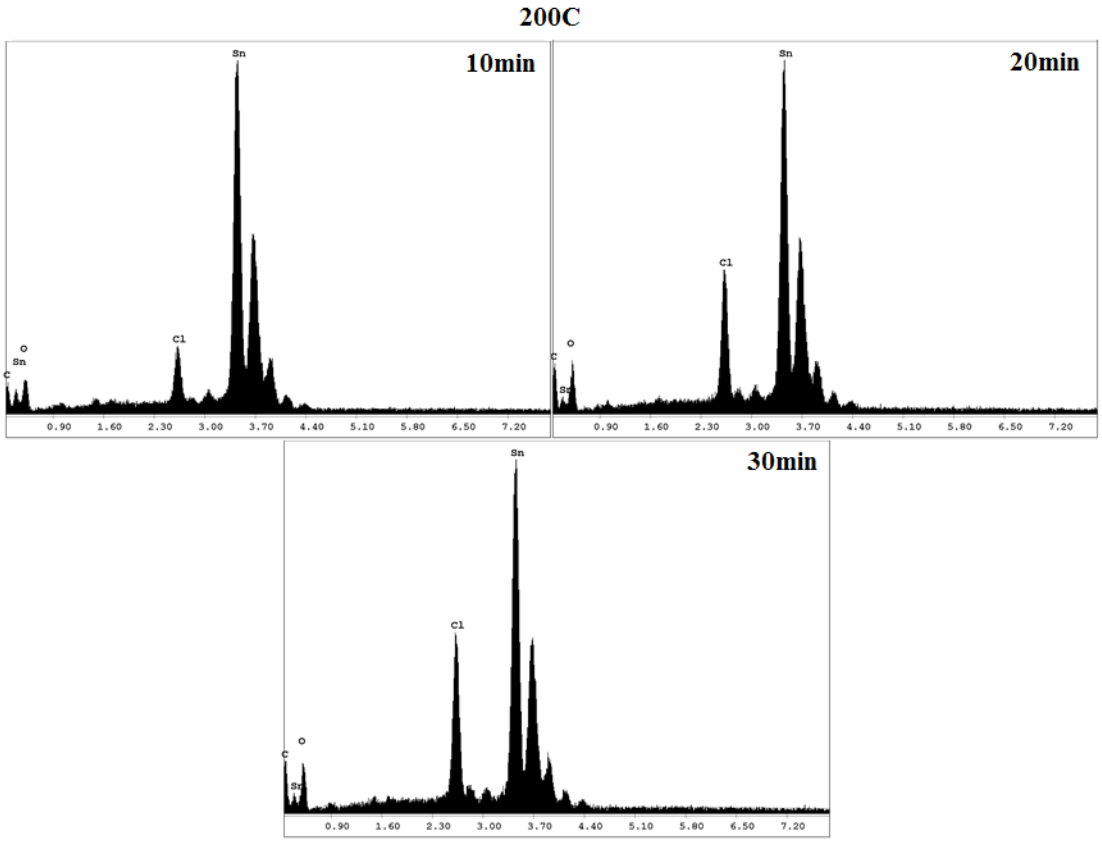

Figure 50: EDS patterns for samples processed at 200°C for different times.

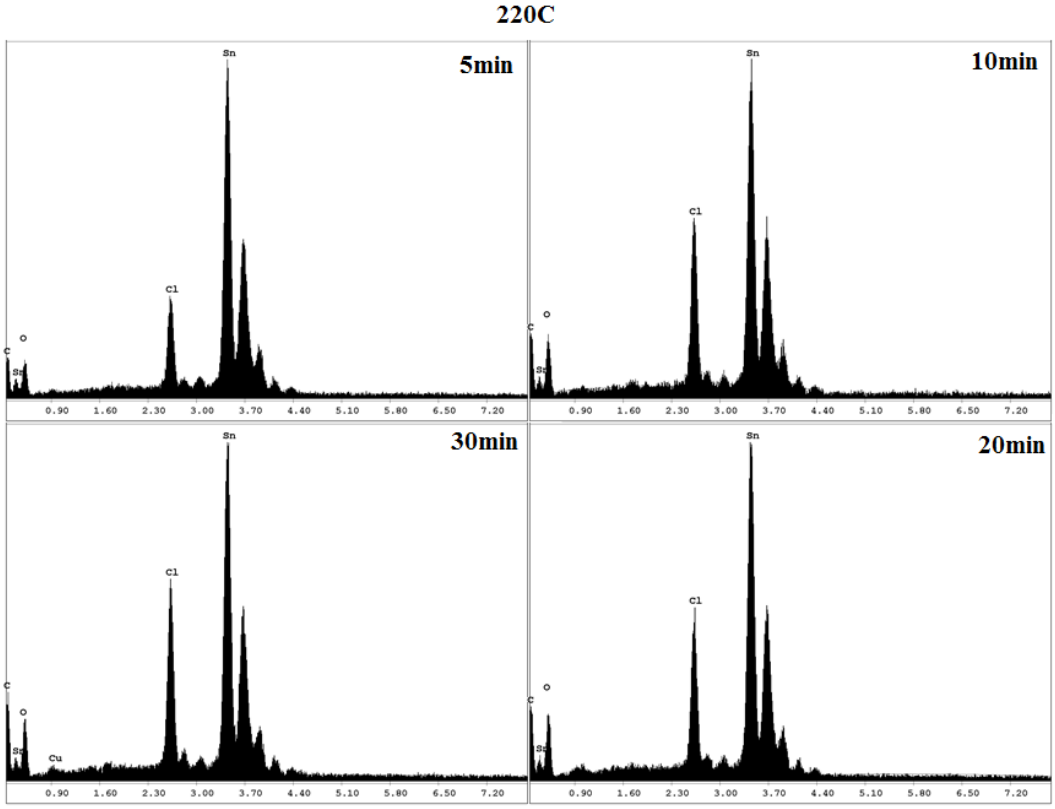

Figure 51:EDS patterns for samples processed at 220°C for different times.

Table 2: EDS measurements on Oxygen quantities

200°C		**220°C**	
Time (min)	O wt. %	Time (min)	O wt. %
		5	0.57
10	0.78	10	2.31
20	1.93	20	3.02
30	1.97	30	3.5

Table 3: Materials properties used for flux and nanoparticle surfactant

	Molecule	Melting Point (C°)	Boiling Point (C°)	Notes
1,10-phenanthroline	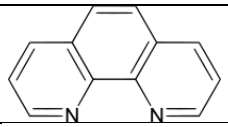	99-117	Not available	Soluble in acetone
Ethylene glycol	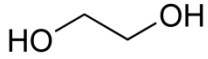	-12.9	197.3	
Glutamic acid hydrochloride	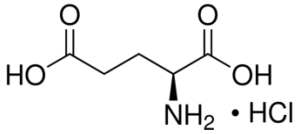	214	Not available	hygroscopic

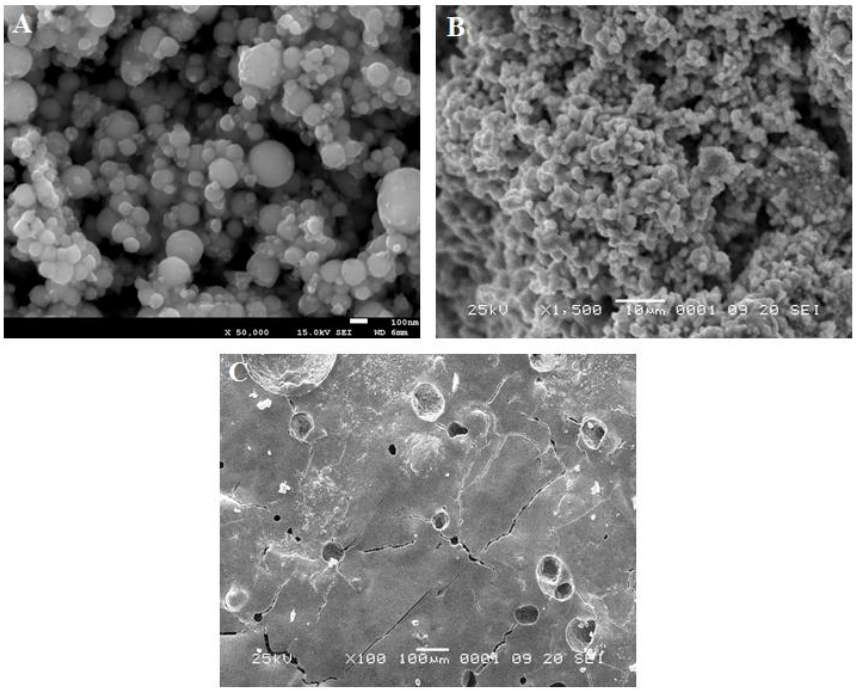

Figure 52: SEM images confirming the sintering process at a temperature of 200°C(A) loose nanoparticles (B) 10 minutes (C) 20 minutes

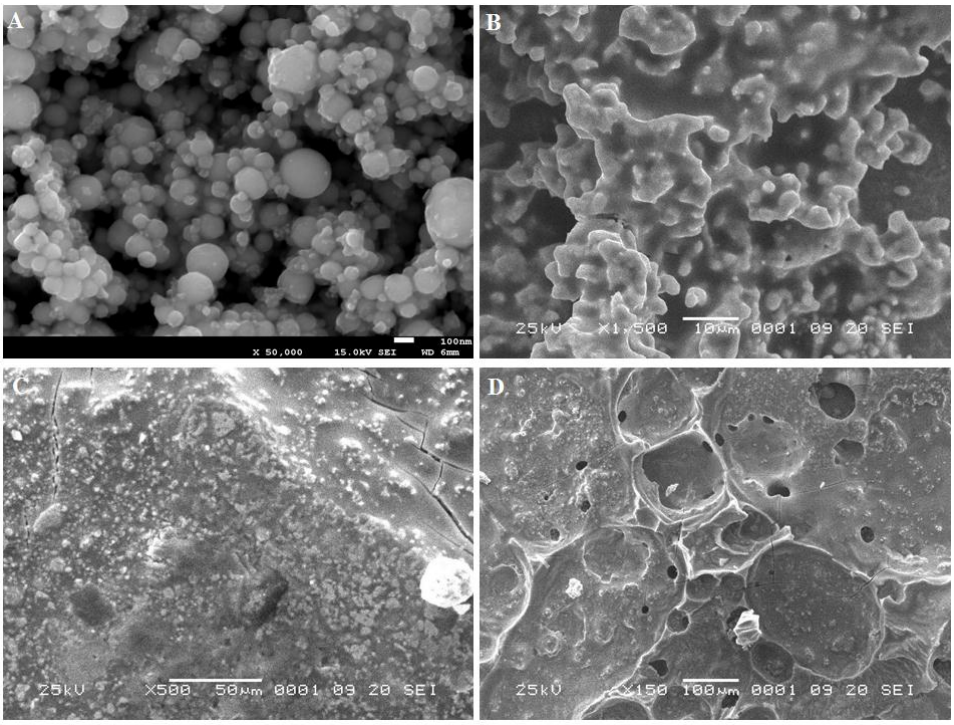

Figure 53: SEM images confirming the sintering process at a temperature of 220°C(A) loose nanoparticles (B) 5 minutes (C) 10 minutes (D) 20 minutes

Figure 52 and Figure 53 show the evolution in the coalescence of nanoparticles at different temperatures, 200°C and 220°C, respectively. The first image in each figure (A) shows the loose Sn nanoparticles powder. Figure 52 have SEM images for a processing time of 10min (B) and 20min (B) and Figure 53 have images for 5 (B), 10 (C) and 20 (D) minutes. At 200°C, the sample processed for 5 minutes didn't withstand the cleaning process (5 minutes of sonication in acetone) and can be inferred that the resulting structure at that time and temperature wasn't strong enough. The resulting structure improves as the processing time is longer. Also, by increasing the processing temperature an improved structure could be obtained at lower processing time. By visually inspecting Figure 52 (C) and Figure 53 (C), a similar surface structure was obtained at different conditions ((A) 200°C 20 min and (B) 220°C 10min). The densification of the material highly depended on the processing time and temperature, an evident sintering mechanism of coalescence. Necks between particles can also be observed in Figure 52 (B) and Figure 53 (B). Typical sintering behavior was observed by analyzing the resulting material surface. By comparing the results obtained with published results, shown in Figure 13: Example of sintering progress in tungsten powder[49]., similarities can be appreciated. The stages of sintering are shown at different times and temperatures. Figure 52 (B) shows the initial stage, Figure 53 (B) shows the intermediate stage and Figure 52 (C) shows the final stage with significant grain growth and the typical pores for a sintered material.

Using a GF-B-HT DDM Novastar reflow oven the use of argon for the process was assessed. The temperature profiles, shown in Figure 54, were used to process the samples with and without argon. For the samples processed in argon, a flow of 50scfm was used with an oven purge time of 20 minutes. The samples were prepared under the same conditions with a differ-

ence of 20 minutes between the samples with and without argon. The cleaning process used was sonication for 10 minutes in acetone.

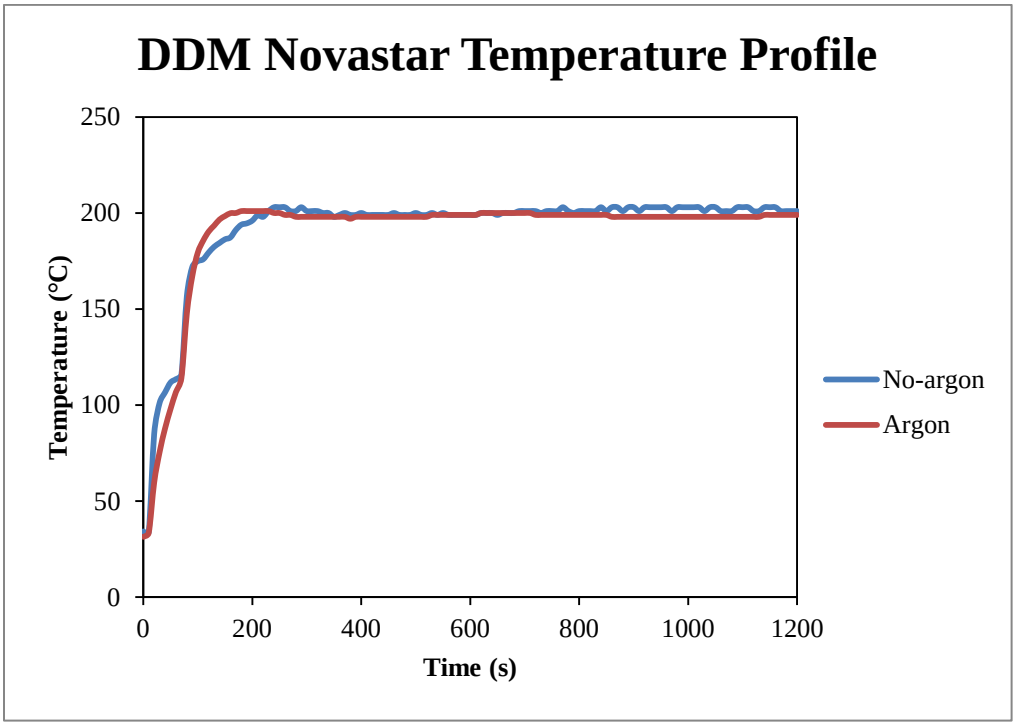

Figure 54: Temperature profiles measured for the DDM reflow oven

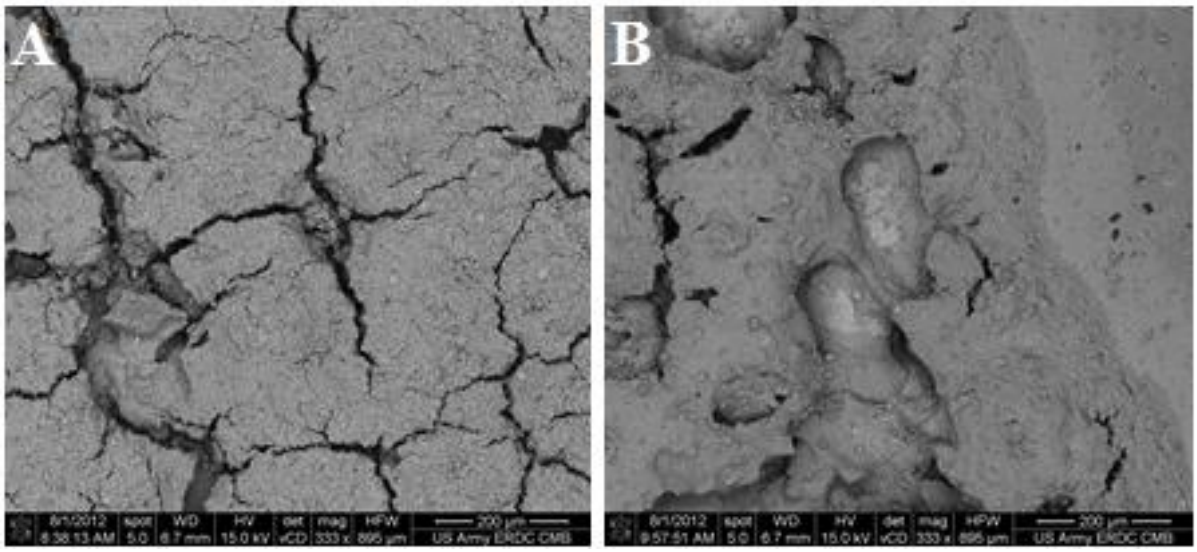

Figure 55: SEM image of the tin surface after reflow in (A) ambient atmosphere (B) inert atmosphere (argon)

SEM imaging was used to characterize the resulting surface for each case. Figure 55(A) shows the typical surface obtained for the samples processed without argon and Figure 55(B) shows the surface of the samples processed in argon. The samples processed with argon showed a less defective surface.

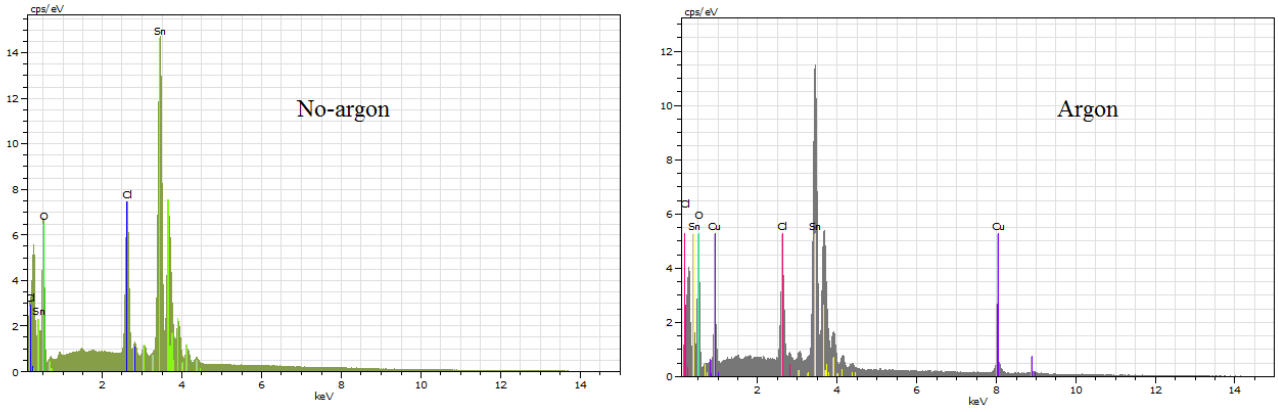

Figure 56: Examples of the EDS patterns obtained

Table 4: EDS average results for different samples and areas

	EDS analysis average wt.% values	
	No- Argon	Argon
Sn	77.33	76.69
O	15.98	14.88
Cl	6.69	8.43

Using EDS analysis, the tin surface was analyzed in order to measure contaminants levels. Table 4 shows the average measurements for different samples. There is no significant difference between the samples processed with or without argon. No significant difference can be seen between the oxidation (O) levels of the samples. Also, high levels of chlorine (Cl) in both samples were found due to the flux acid.

The electrical properties of the developed material were characterized. Electrical conductivity is the property of a material that measures the ability to conduct an electrical current. For

the attachment of electronic components materials with high conductivity are required. The high current densities used can produce enough heat causing damage to the attachment or the package. The electrical conductivity of the sintered tin nanoparticles was measured and compared to the bulk value reported in literature.

The resistance of material was measured using a Digital Milli-ohm meter (model 310 of BK precision) based on a four wire Kelvin test. The four wire Kelvin test working principle is to supply a current between two points and measure the voltage drop across two points, as shown in Figure 57. A constant current is applied between terminals 1 and 4 and the voltage drop is measured between terminals 2 and 3, maintaining a constant distance between the two across all the samples measured. Using Ohm's law (V=RI), the resistance between points 2 and 3 is calculated.

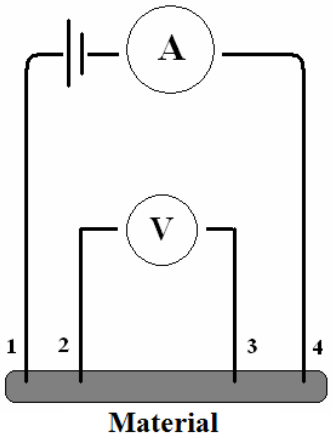

Figure 57: Schematic of the four wire Kelvin test (taken from: http://en.wikipedia.org/wiki/File:Four-point.png)

The material property of resistivity is calculated from the resistance. Resistivity (ρ) depends solely on the resistance and geometrical parameters. The equation describing the resistivity of a material is $\rho = \frac{RA_{cross-sectional}}{L}$, where L is the distance between the probes measuring the voltage drop, R is the resistance and $A_{cross\text{-}sectional}$ is the transversal area of the material, as shown

in Figure 58. Then the material conductivity is calculated, this value is defined as the inverse of the resistivity ($\frac{1}{\rho}$).

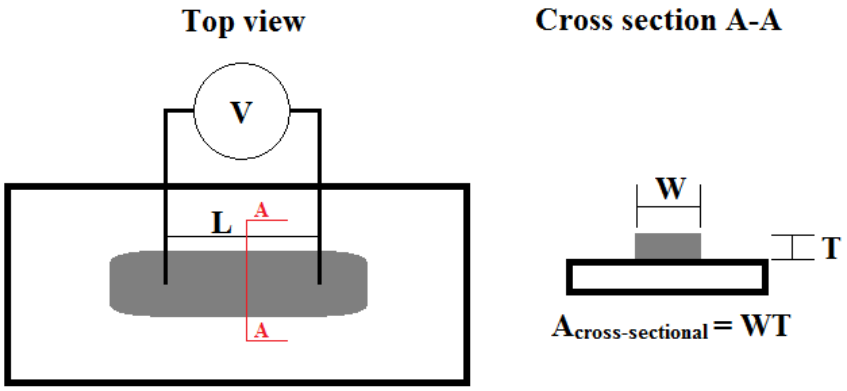

Figure 58: Schematic of samples and the dimensions used for analysis

The samples were prepared using the best embodiment of the paste and the reflow profile used was measured (Figure 54). The solder paste was deposited over a glass substrate using the process of stencil printing, and then they were processed using the reflow oven with and without argon. The as-processed sample is shown in Figure 59. The glass substrate was chosen because the sintered material should be electrically isolated so that the ohm-meter will only measure the resistance of the tin. The distance L was maintained constant throughout the samples (5mm). The distances W and T were measured with a digital caliper in each samples and then averaged because the stencil used was the same for all the samples and the measurements were close to each other. A total of 30 samples were prepared, 15 under environment conditions and 15 under argon.

Figure 59: As-processed sample

Table 5: Average electrical conductivity values

	Experimental: No-argon	Experimental: Argon	Theoretical: (http://periodictable.com/Elements/050/data.html)
Electrical Conductivity (S/m)	$1.36x10^5$	$3.29x10^5$	$9.10x10^6$

The resulting averaged conductivity values and the theoretical value for tin are shown in Table 5. Both measured values were an order of magnitude below the theoretical value. The conductivity of the sintered material gets a slight increase by the use of argon. Previous experiments showed an improvement of the surface when the samples are processed under argon atmosphere. The difference between the experimental and theoretical values can be attributed to the porous structure obtained via sintering. The cross-sectional area used in the resistivity calculations does not take into account the pores of the structure.

4.1.3. Thermal Analysis of the materials used

All the samples were analyzed using a DSC-e by Instrument Specialists. Aluminum pans were used without lid in order to mimic the real soldering process in which the materials will be exposed to the ambient inside the reflow oven. Argon, flowing at 15cc/min, was used to maintain an inert atmosphere on the DSC's furnace.

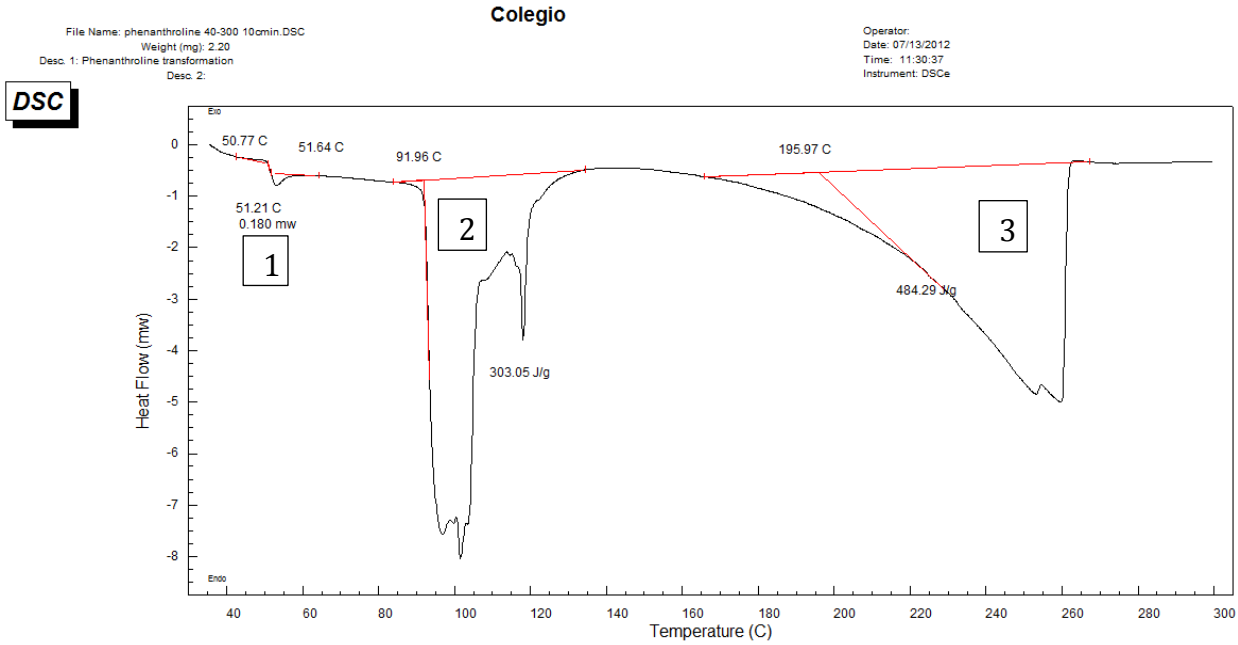

Figure 60: DSC curve for 1,10 phenanthroline.

When processing 1,10 phenanthroline, from 40 to 300°C at a heat rate of 10°C/min, several phase transformations were observed. A glass transition (#1) occurs at around 51°C, melting (#2) occurs at 92°C, and boiling (#3) at around 195°C, as shown in Figure 60. The third peak depicts a typical constant evaporation curve[60]; the inert gas, argon, is moving the gaseous 1,10 phenanthroline out of the furnace.

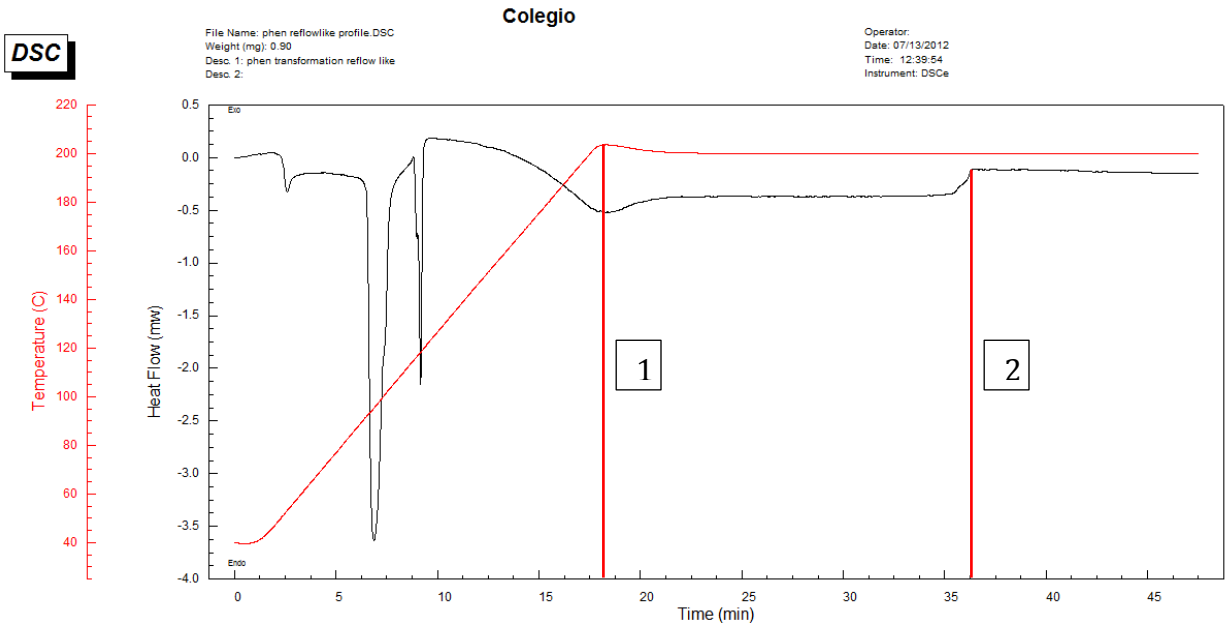

Figure 61: DSC reflow-like profile (ramp and hold).

Using a reflow-like temperature profile the changes in the material were registered versus time. The parameters for this test were 10°C/min from 30 to 200°C followed by an isothermal hold of 30 minutes as shown in Figure 61. Holding time began at the 17.5 minutes mark (#1). From the graph it can be observed that after holding the temperature for 18.5 minutes no further reactions were recorded as suggested from the flat line after the #2 mark. After this test the pan was observed to be completely empty, an indication that all the 1,10 phenanthroline converted to gas. It can be stated, with the used temperature profile, that all the material was gone by the 36th minute (#2) of processing.

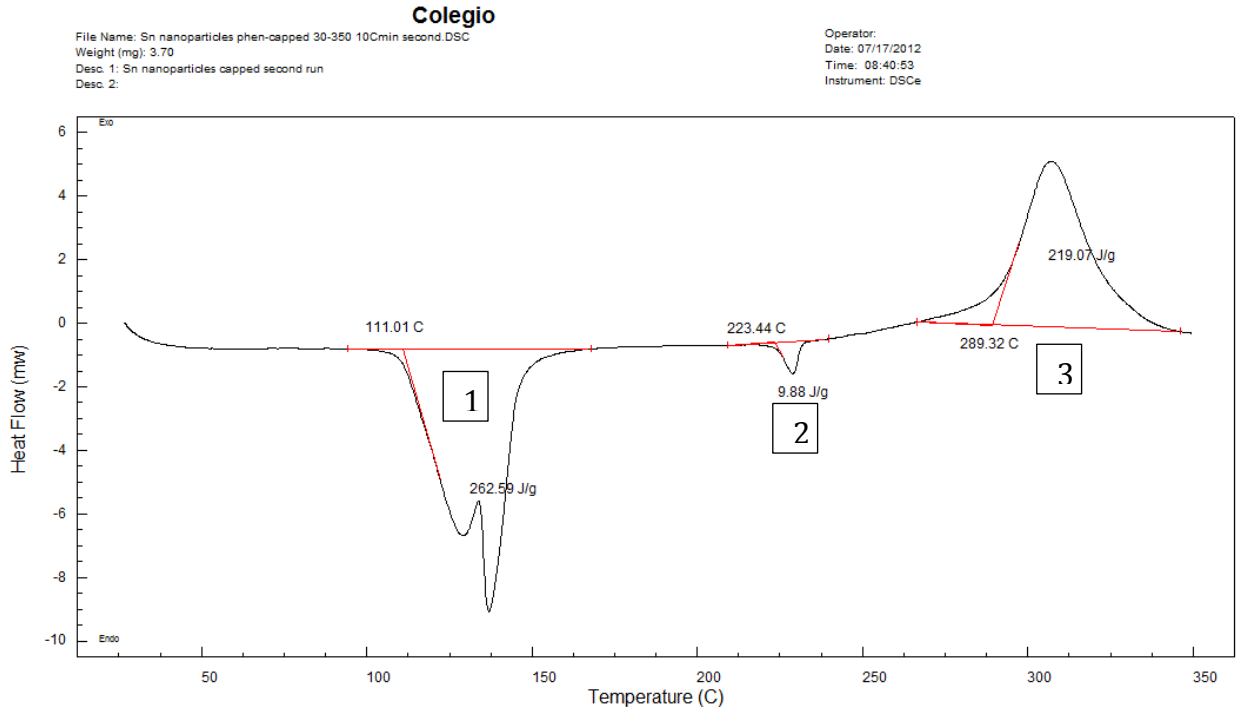

Figure 62: DSC profile of the tin capped nanoparticles

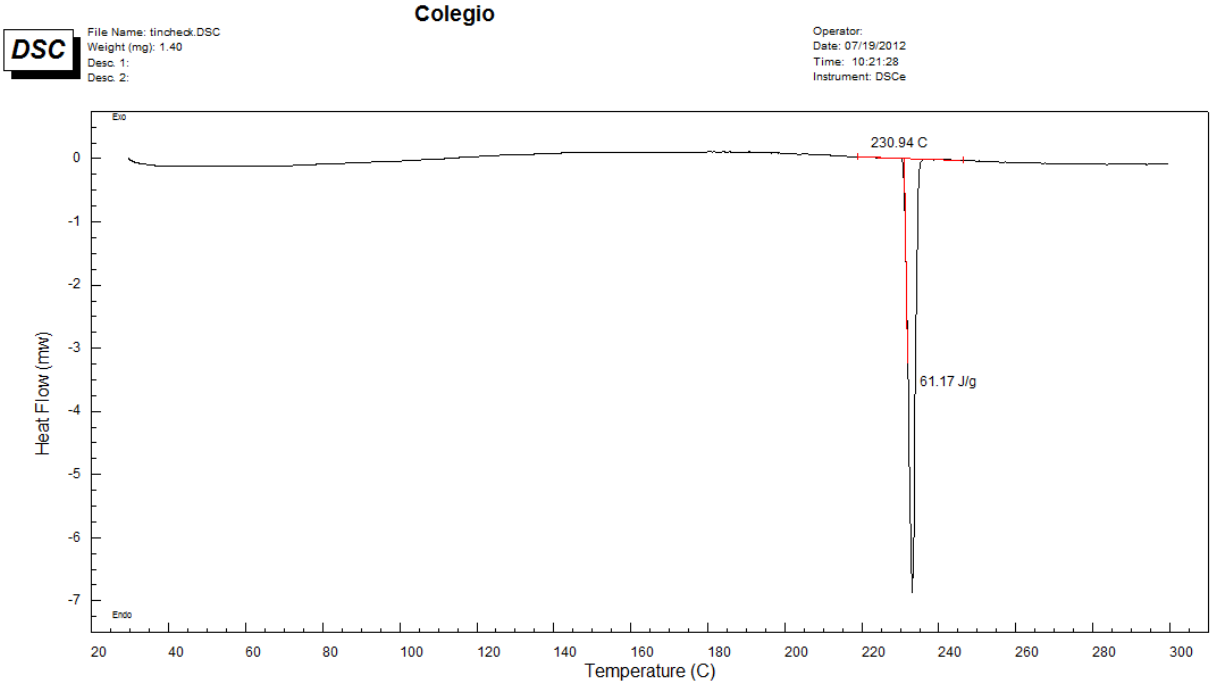

Figure 63: DSC curve for bulk tin

Using a 40 to 350°C temperature sweep, at a heating rate of 10°C/min, a DSC curve shown in Figure 62 for the 1,10 phenanthroline-capped tin nanoparticles was obtained. In this

case, a transformation (#1) at ~111°C was observed and attributed to the melting of the 1,10 phenanthroline; this behavior showed some difference when compared to the isolated polymer. The bond of the polymer with the nanoparticle is different from the polymer bond with itself. From the previous analysis on the isolated 1,10 phenanthroline, it was observed that the polymer completely evaporates below 200°C. The second transformation (#2) occurs at about 223°C which is attributed to the tin melting, a third peak (#3) shows what seems to be oxidation of the material. Figure 63 provides a DSC trace for bulk tin which will serve as a comparison basis. According to the data, tin nanoparticles have shown a depression of 8°C in their melting point, being 231°C the melting point measured for bulk tin.

The as-received nanoparticles were analyzed using a ramp profile. Figure 64 shows the DSC pattern for our sample. The DSC shows an endothermic peak related to the melting of the nanoparticles. The melting process starts (onset) around 221°C.

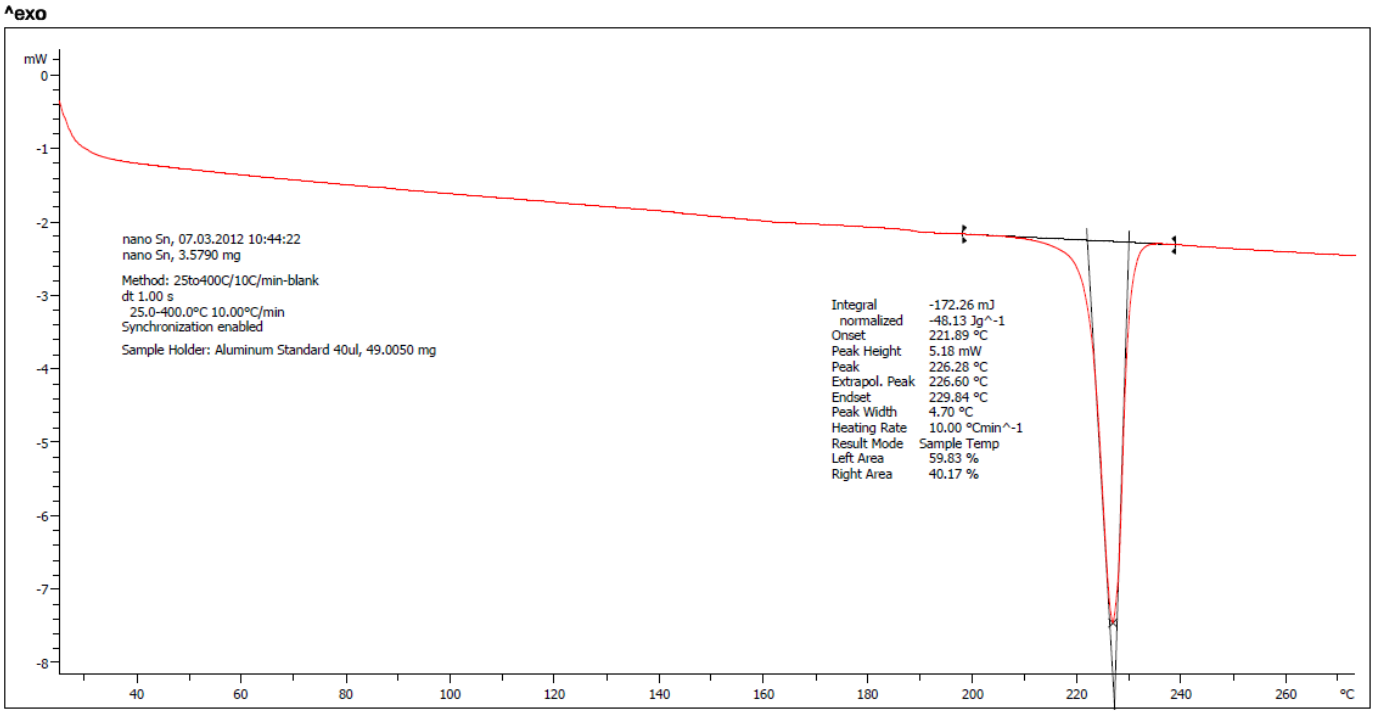

Figure 64: DSC graph on SSnano nanoparticles

TGA (Figure 65) shows an increase in mass as the temperature increases. This increase in mass could be associated to oxidation. The derivative of the mass versus temperature curve is at the lower end of this figure. The peak shows the temperature at which the oxidation process ends due to saturation which happened to be around 225°C.

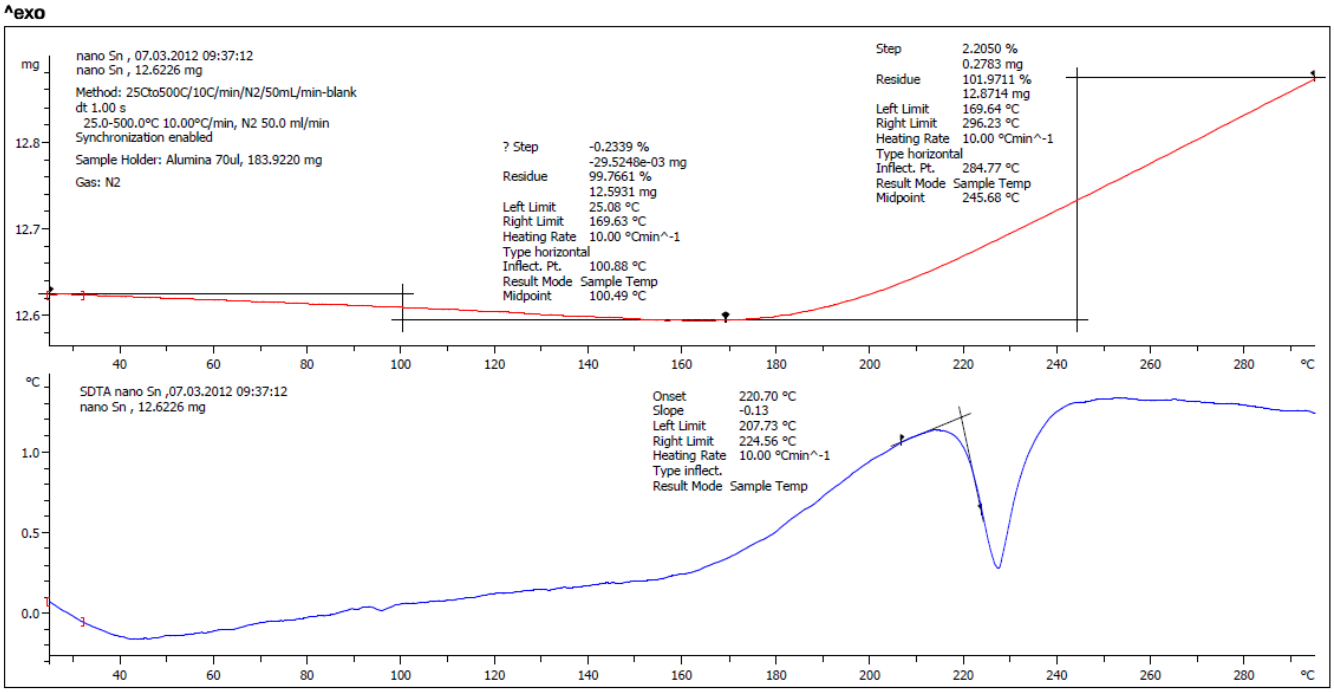

Figure 65: TGA for the Sn commercial nanoparticles

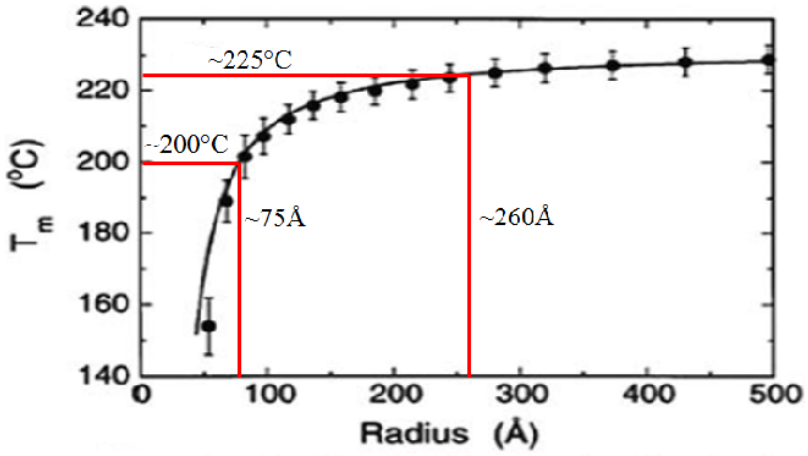

Figure 66: Tin melting point depression curve as function of particle size.

Figure 66 shows the melting point depression curve for tin as function of particle radius. Assuming that the onset of the DSC curve was approximately 225°C for both nanomaterials, i.e.

UPRM synthesized and procured from SSnano, the following analysis was done. Using a melting point temperature of 225°C, the average diameter of the nanoparticle should be 52nm according to Figure 66 . The experimental processing temperature used for reflowing the samples was 200°C. From inspection of Figure 66 a particle diameter of ~15nm is required if melting at 200°C is expected. The average particle diameter for the synthesized nanoparticles was approximately 45nm and 94.6nm for the commercially procured. The synthesized nanoparticles match the theoretical value for melting point depression as presented above, however the commercial nanoparticles are off by at least 5°C. The size distribution of the synthesized nanoparticles is narrower than the commercial material; this could be the causal factor for the concordance between the theoretical and experimental results. A critical observation is that coalescence of the nanoparticles was attained at 200°C, thus proving that if the nanoparticles are not small enough the mechanism that dominates is sintering where mass transfer between particles promotes the formation of a continuous body. In addition to that, we were able to demonstrate the ability to measure nanoscale properties with macro-analysis. Below a radius of 10nm the depression curve get steeper, therefore in this region the melting point depression should dominate the coalescence process.

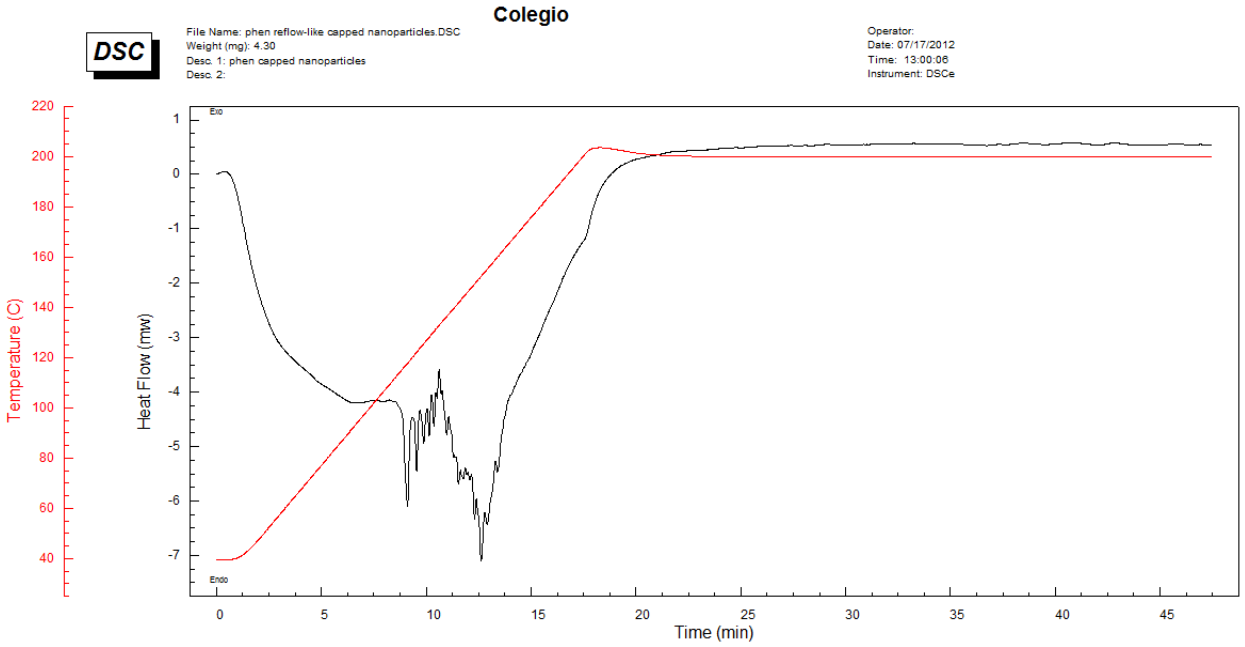

Figure 67: DSC curve with ramp and hold for the capped nanoparticles

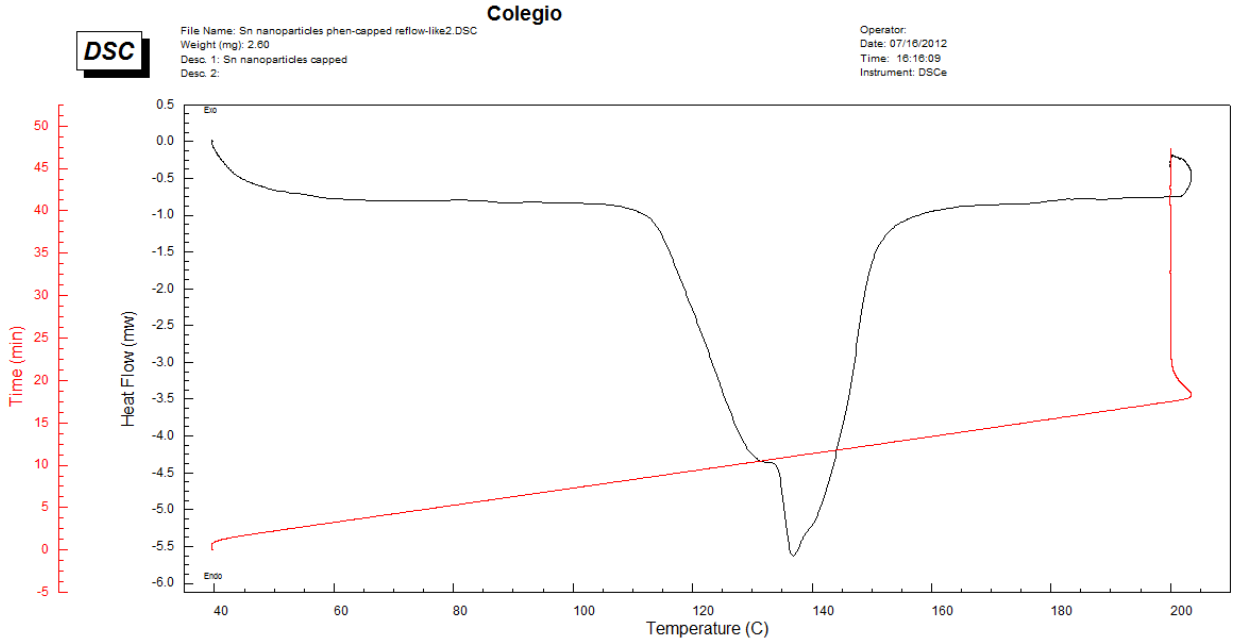

Figure 68: DSC curve with ramp and hold for the capped nanoparticles (2)

Using a reflow-like profile, as shown in Figure 68 and Figure 68, (the same used for the 1,10 phenanthroline) the capped nanoparticles were studied. Assuming that all the 1,10 phenanthroline will evaporate with this thermal profile, the quantity of capping agent covering the particles was estimated. Using off-line thermogravimetry[60] (weighing the samples before and after

the DSC test) a quantitative estimation of the amount of 1,10 phenanthroline was performed. In this case it was found that approximately 20% of the weight of the capped nanoparticles is 1,10 phenanthroline. The peak shown in Figure 68 corresponds to the peak #1 shown in Figure 62 which means that the 1,10 phenanthroline, when used as capping for nanoparticles, have a shift on its thermal properties.

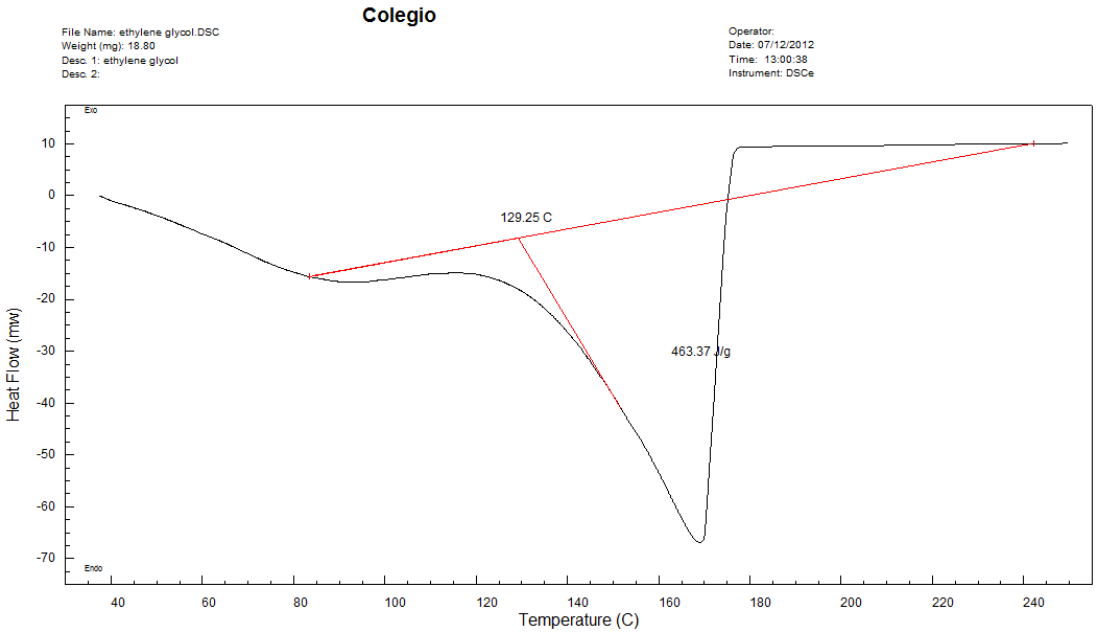

Figure 69: DSC curve for ethylene glycol

From the DSC analysis, as given in Figure 69, of the Ethylene Glycol it can be observed that after ~180°C the transformation ends. The conditions for this analysis were 10°C/min from 35 to 250°C. The curve is the typical behavior of an open pan evaporating material.

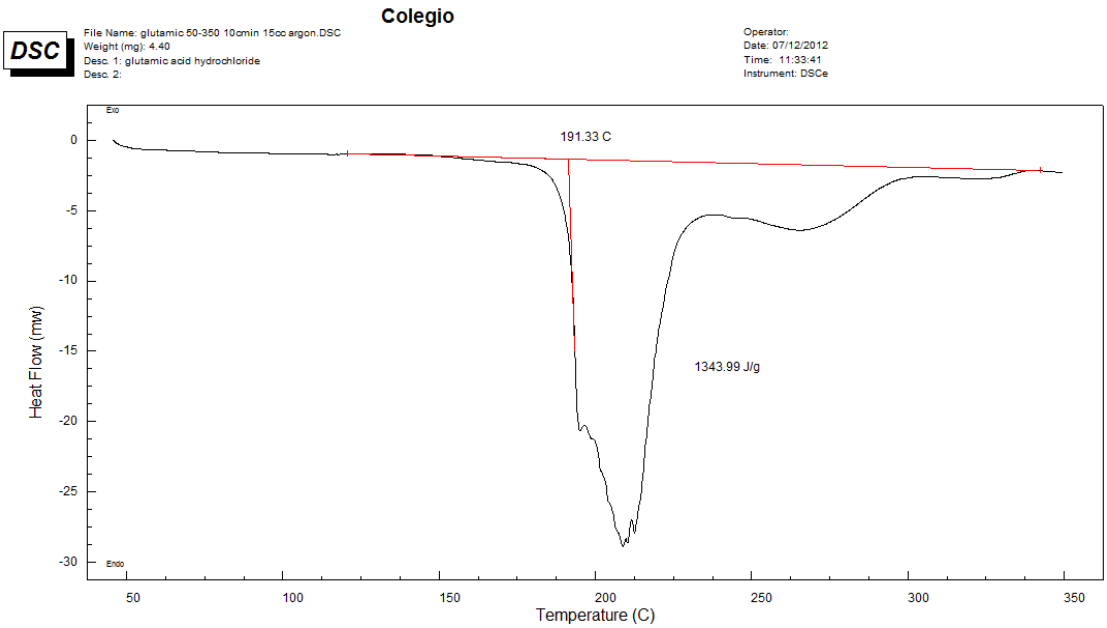

Figure 70: DSC curve of glutamic acid hydrochloride

Processing parameters of 10°C/min from 35 to 350°C were used to analyze the isolated glutamic acid hydrochloride in the DSC. From Figure 70 can be observed that the transformation of the acid starts at around 190°C, also the curve shows a melting with decomposition behavior typical of organic compounds[60]. After the DSC test burnt residues were observed, as depicted in Figure 71, on the pan confirming the decomposition of the material. By off-line thermogravimetry, a decrease of 61% in mass was measured.

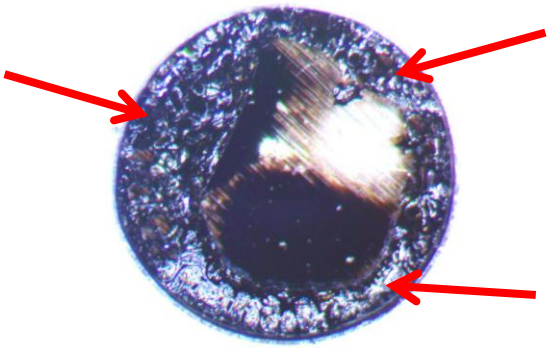

Figure 71: Residues on pan after DSC analysis

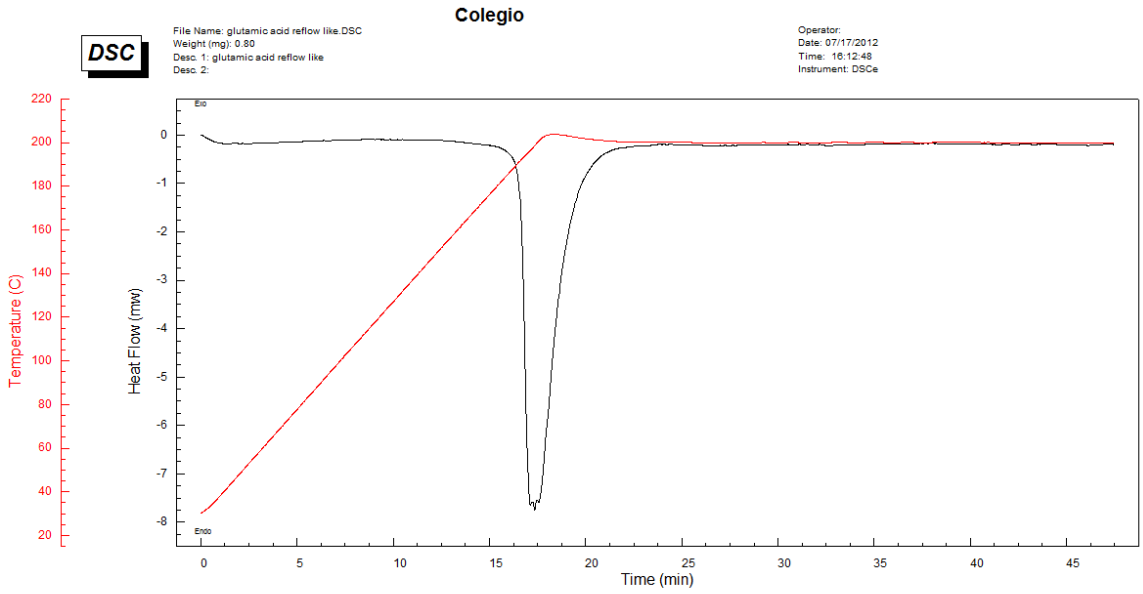

Figure 72: DSC profile with ramp and hold for the glutamic acid hydrochloride

Using a ramp and hold time, the behavior of the acid in a reflow environment was assessed. The parameters were 10°C/min from 30 to 200°C with a holding time of 30 minutes as shown in Figure 72. The mass loss due to this profile was around 50%, that is 11% less than when ramping up to 350°C where the decomposition is accelerated.

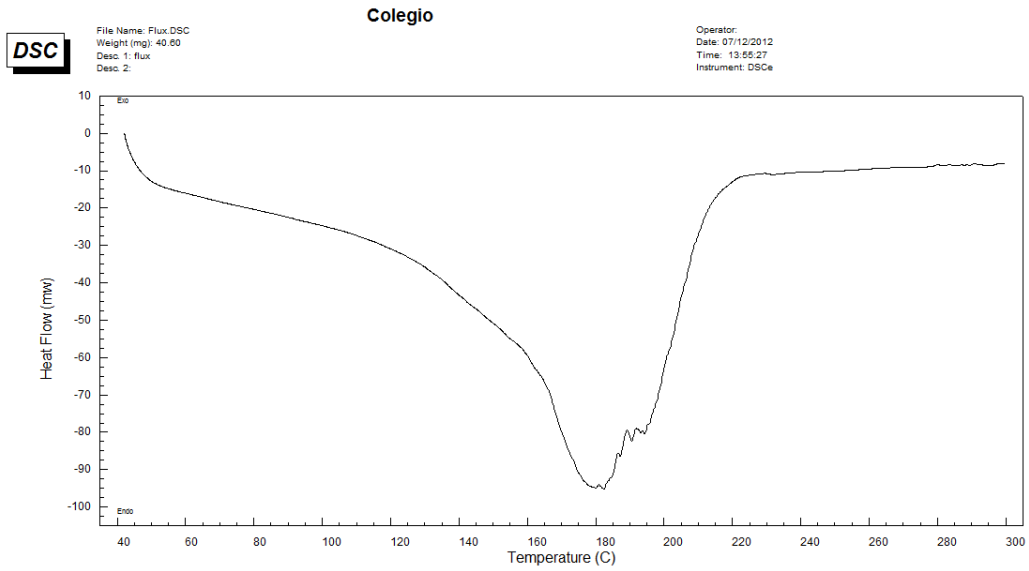

Figure 73: DSC profile for the flux

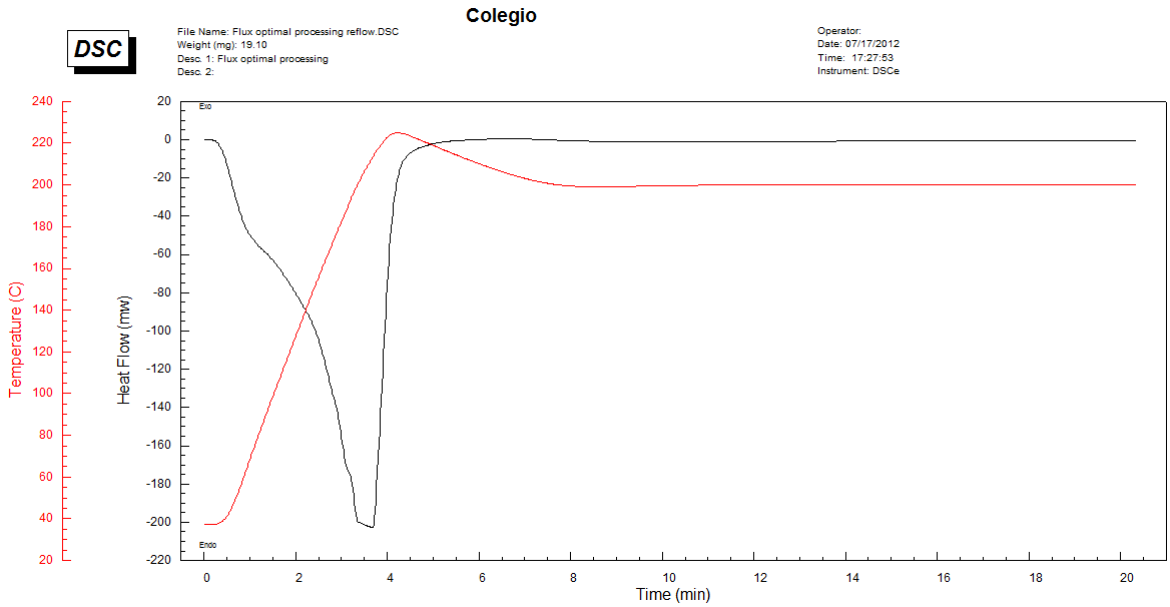

Figure 74: DSC profile for the flux with optimal parameters

The flux was analyzed using different profiles. The first one, Figure 73, shows the analysis for 10°C/min ramp with a temperature sweep from 30 to 300°C which resulted in a mass loss of 68%. The second profile, Figure 74, shows a profile similar to the optimal parameters found for our samples. The profile has a ramp of 60°C/min up to 200 and a total time of 20 minutes. After the profile, the mass loss was around 62%, which suggests that our samples have a ~38% of contaminants (from the flux) after reflowing. Figure 75 shows a picture of the flux residues.

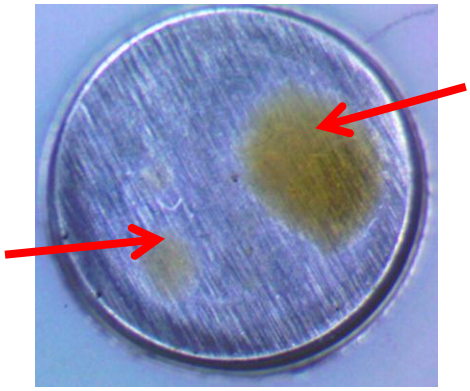

Figure 75: Residues of the flux after optimal processing parameters

The solder pastes, synthesized and commercial-based, were analyzed using the best embodiment for each case. When the nanoparticles were analyzed by themselves, no coalescence could be observed, but adding a flux resulted in evident coagulation. The flux is very important in the coalescence of nanoparticles; in this particular case a strong flux is required due to the propensity of tin to oxidation.

The synthesized nanoparticle paste was analyzed by using two different DSC profiles, 30-300°C at 10°C/min and 30-200°C with isothermal hold. With the first profile, a foam-like structure was obtained as shown in Figure 76(A). With the second profile, coalescence was observed together with some residues as shown in Figure 76(B). A reduction of 65% of the weight was measured on this condition.

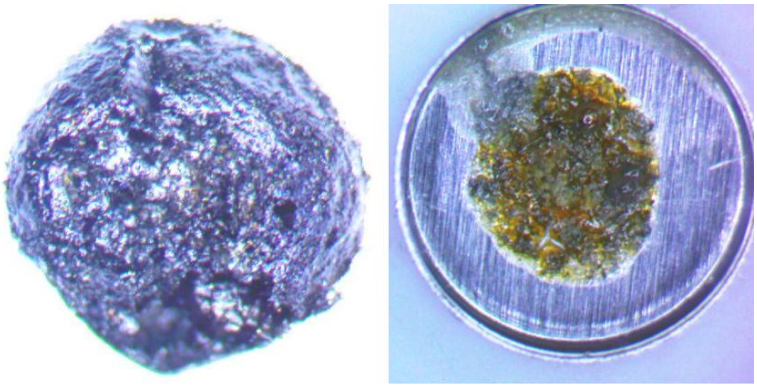

(A) (B)

Figure 76: Synthesized nanoparticles solder paste after DSC profile: (A) 30-300°C at 10°C/min (B) 30-200°C with isothermal hold.

The solder paste based on commercial nanoparticles was analyzed by using three different profiles as shown in Figure 77. The continuous ramp yielded the surface with the most imperfections. The effect of the ramp steepness (heating rate) was assessed using two different ramps with the same holding time. The steeper ramp, 60°C/min, produces the best surface on the solder (less roughness). As stated by Groza[50], the consolidation mechanism works better when high ramps are used.

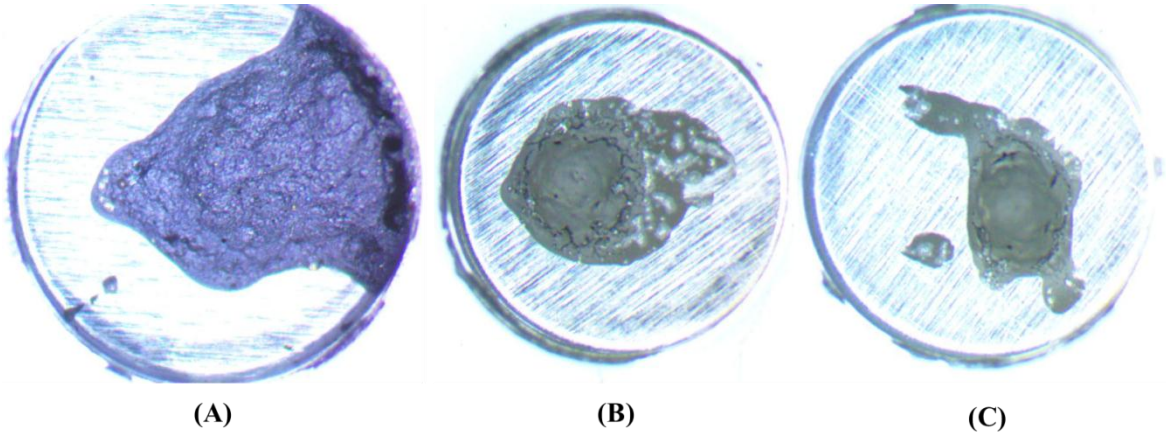

Figure 77: SSnano nanoparticles solder paste after DSC profile: (A) 30-300°C at 10°C/min (B) 30-200°C at 10°C/min with isothermal hold (B) 30-200°C at 60°C/min with isothermal hold.

4.2. Tin whiskers

4.2.1. Initial stage

A ternary system, Ag-Ni-Cu, was deposited over matte tin. The layers of materials used in this project are similar to those used in commercially available leadframes, i.e. a Cu substrate plated with Sn. SEM characterization was performed on a cross shape pattern on the surface of the sample which divided the sample in quadrants as depicted in Figure 78.

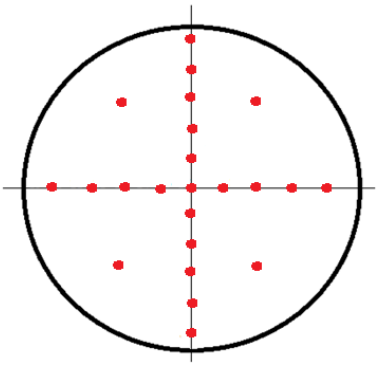

Figure 78: Schematic showing the areas studied with the SEM (represented by the dots).

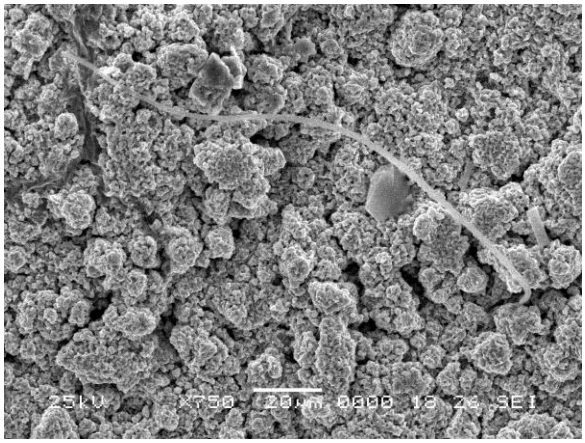

(a) 92.6 wt.% Sn, 2.9 wt.% Ni, 2.3 wt.% Cu & 2.1 wt.% Ag

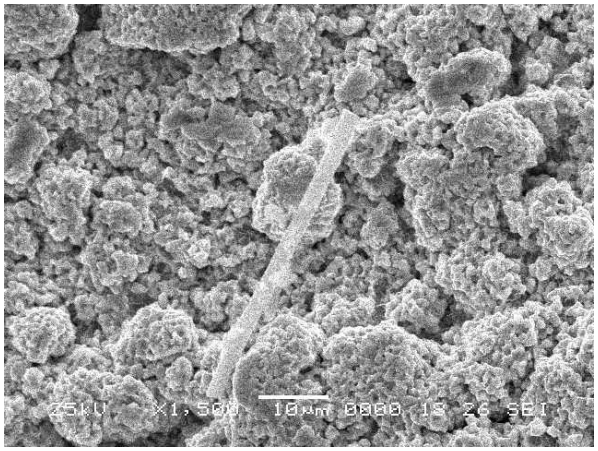

(b) 94.3 wt.% Sn, 2.8 wt.% Ni, 2.2 wt.% Cu & 0.7 wt.% Ag

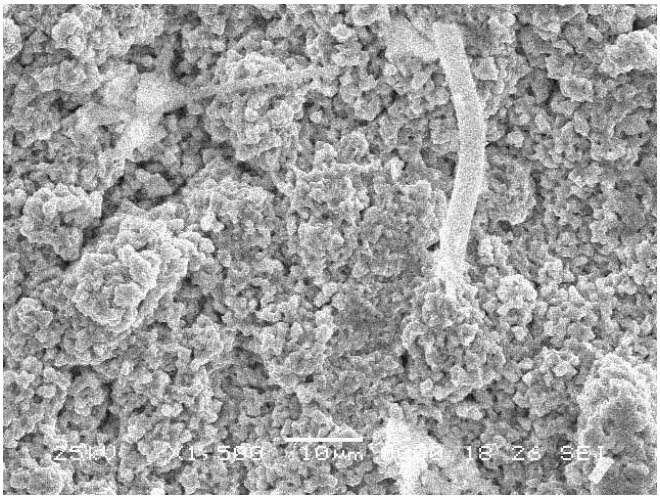

(c) 96 wt.% Sn, 1.4 wt.% Ni & 2.6 wt.% Cu

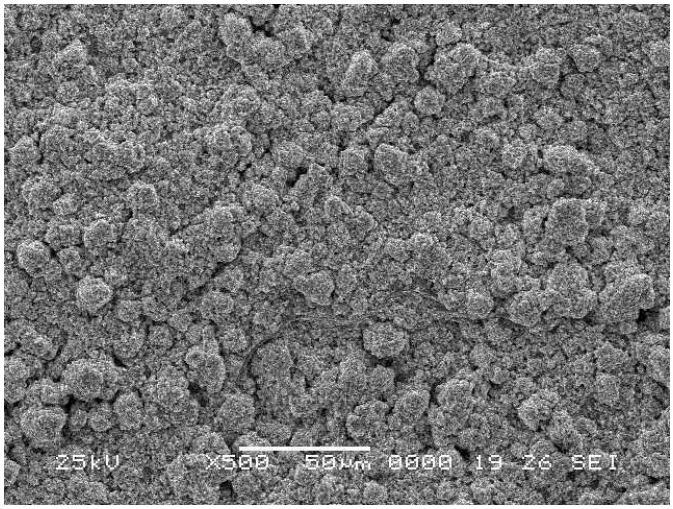

(d) 100 wt. % Sn

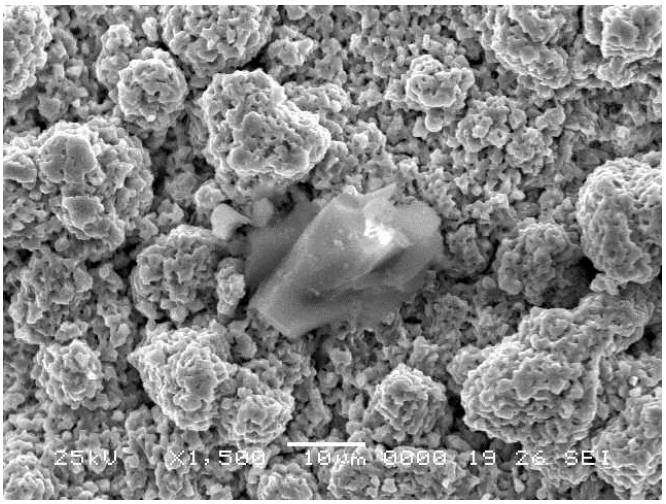

(e) 100 wt. % Sn

Figure 79: SEM images of areas hidden (masked) from the sputtered materials.

The characterization process began by inspecting selected areas that were to be masked from the sputtered materials, i.e. no Ag-Ni-Cu should be detected. From the EDS analysis, it was observed that traces of the sputtered constituents diffused into the Sn (shown in Figure 79 (a) (b) (c)). It is believed that the reflow process accelerated the three dimensional diffusion resulting in the Sn getting "contaminated" with Ag-Ni-Cu. Furthermore, the mask used may have leaved a gap thus letting some of the materials to be sputtered on the control area (was what supposed to be 100 wt.% Sn), however pure tin areas were still successfully identified across the sample.

Effectively, tin whiskers were found on the studied tin-rich areas. As reported in literature[61], electroplated tin was found to be more susceptible to whiskers than alloyed materials.

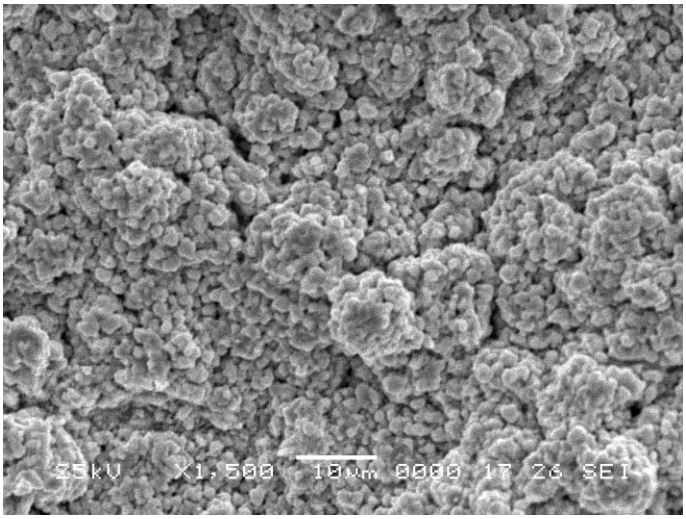

(a) 62.2 wt.% Sn, 18.1 wt.% Ni, & 19.7 wt.% Cu

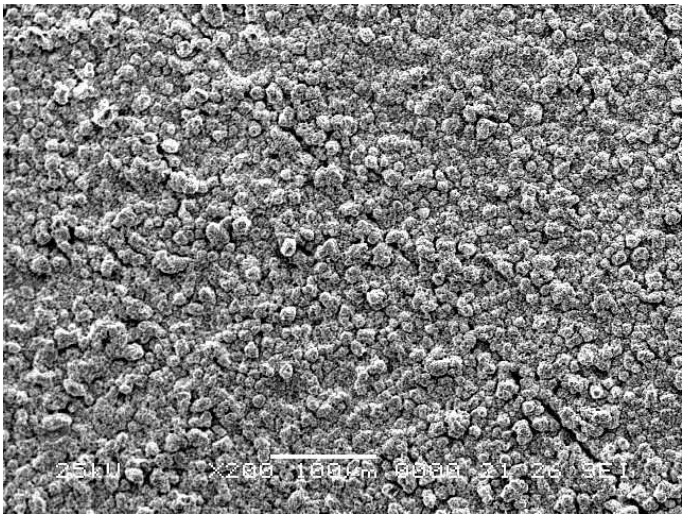

(b) 63.5 wt.% Sn, 13.4 wt.% Ni, 21.7 wt.% Cu & 1.4 wt.% Ag

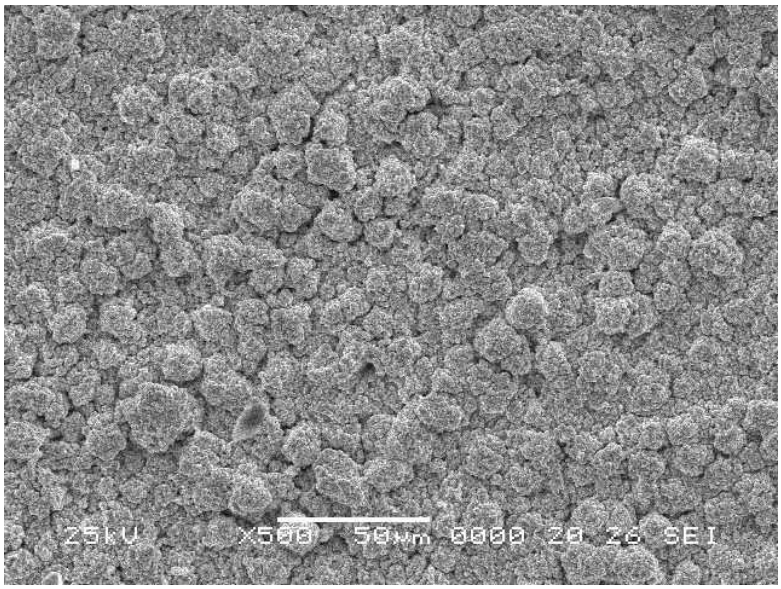

(c) 61.2 wt.% Sn, 15.1 wt.% Ni, & 23.8 wt.% Cu

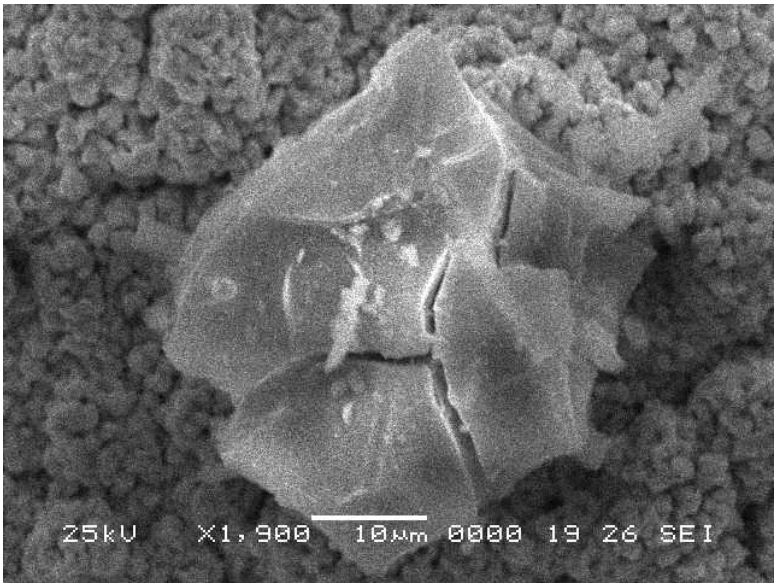

(d) 65.5 wt.% Sn, 13.1 wt.% Ni, & 21.4 wt.% Cu

Figure 80: SEM images of alloyed (unmasked) areas.

Unmasked areas, where a mixture of all constituents was expected, were analyzed by EDS revealing a high concentration of Sn (~61 – 66 wt.%), however these Sn concentrations are well below of what was observed in the areas reported in Figure 79. The low deposition rate of Ag is evident from this analysis where Ag was not detected or barely detected as can be noted from the elemental compositions in Figure 80. It is being theorized that the mixing of all constit-

uents through the thickness of the compositional library was not completely achieved during the reflow process. A longer dwell time at the peak temperature is proposed to guarantee proper mixing and the achievement of a homogeneous mixture as schematically depicted in Figure 24.

From the initial phase of this combinatorial approach for the mitigation of tin whiskers it can be pointed out that a novel methodology for the fabrication and testing of specimens, that can indeed enhance the screening of complex combination of materials in a compact format. Preliminary results indicate that there are some combinations, Figure 80 a,b,c; that tend to minimize the growth of the whiskers whereas other elemental composition exhibited their propensity to growth the whiskers (Figure 80d).

4.2.2. Refined approach

4.2.2.1. Control samples

Three 25mm^2 Sn electroplated Cu squares were used as control. The control samples went through the same reflow profile and high temperature/high humidity test as the co-sputtered samples. Characterization with SEM and EDS revealed growth of whiskers in the developed plating procedure.

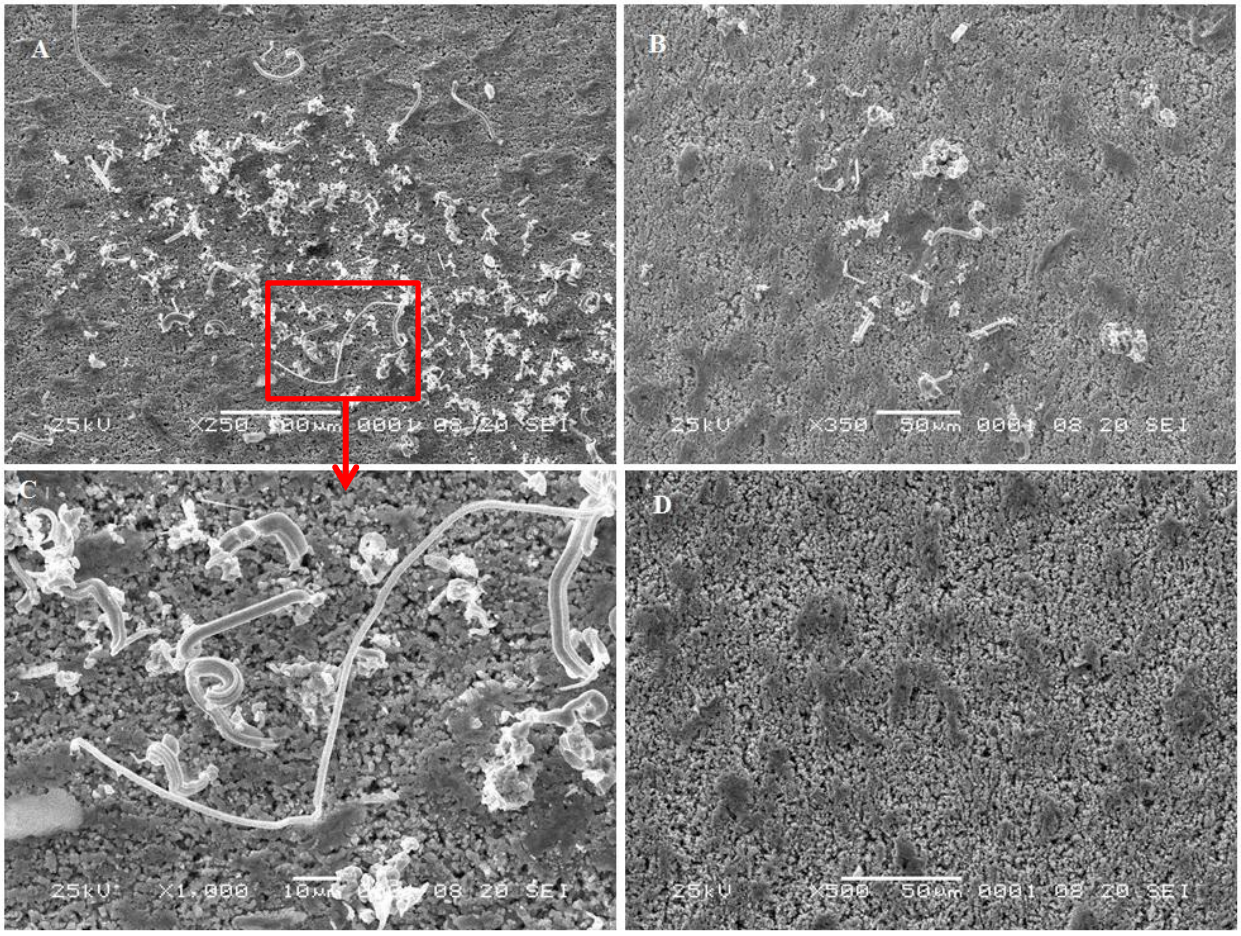

Figure 81: Different areas having different behavior on whisker growth.

Areas with high densities of whisker growth were found on the control samples. As shown in Figure 81 (A,C) whiskers ranging from approximately 20 to 120um showed on the samples. Areas with lower concentration of whiskers (Figure 81B) were also found. Areas with no growth (Figure 81D) were a lot less common through the samples.

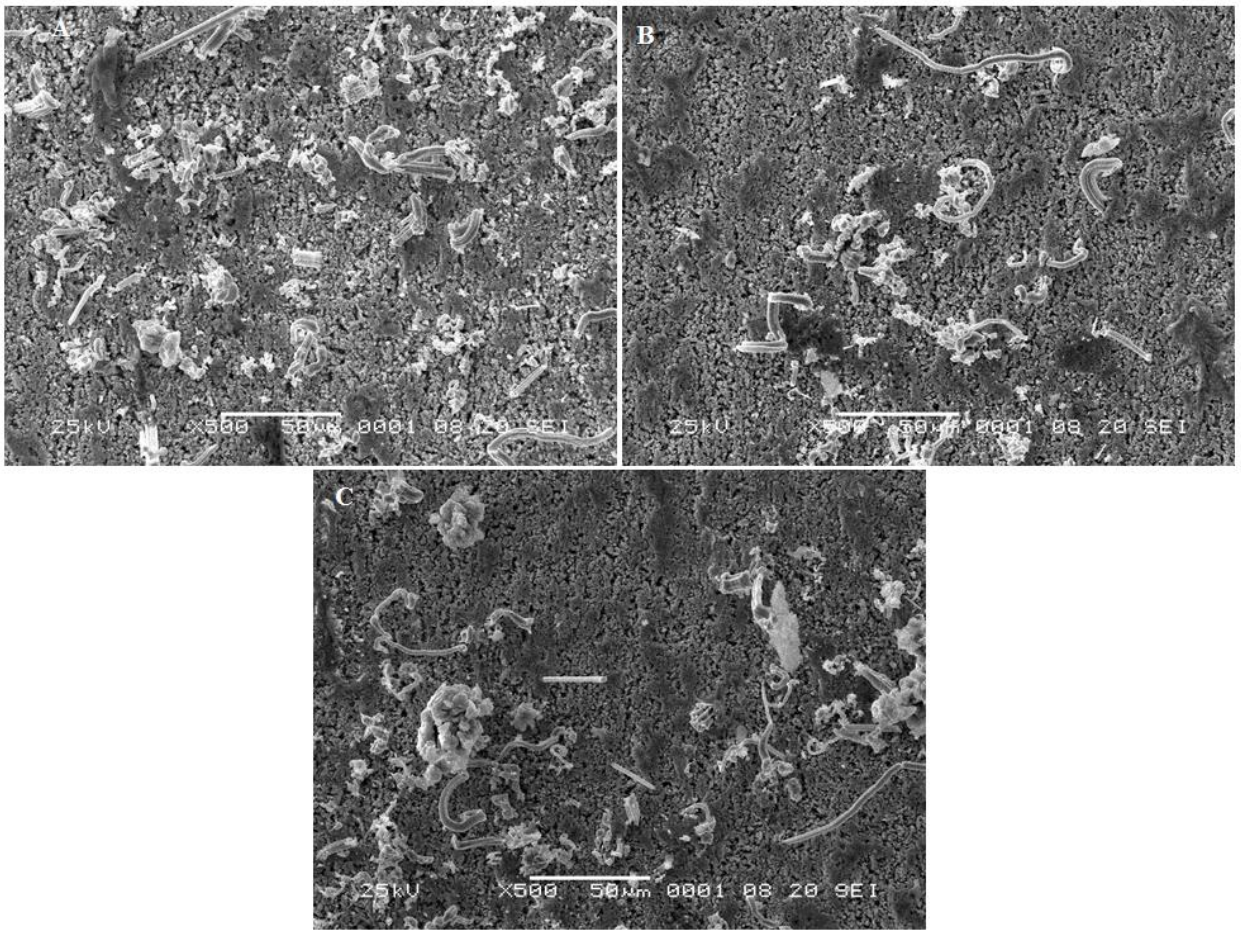

Figure 82: Areas showing high concentration of whiskers.

In Figure 82(A, B, C), areas of approximately 0.08mm^2 are shown. Whiskers of up to 75µm long with different shapes were found on the electroplated Sn film over Cu. A detail of the different shapes that were found is given in Figure 83 (A, B, C, D) and Figure 84 (A, B, C, D). Long (110 µm max) and straight whiskers were very common, a type of growth that increases the risk of short circuits when encountered in fine pitch components.

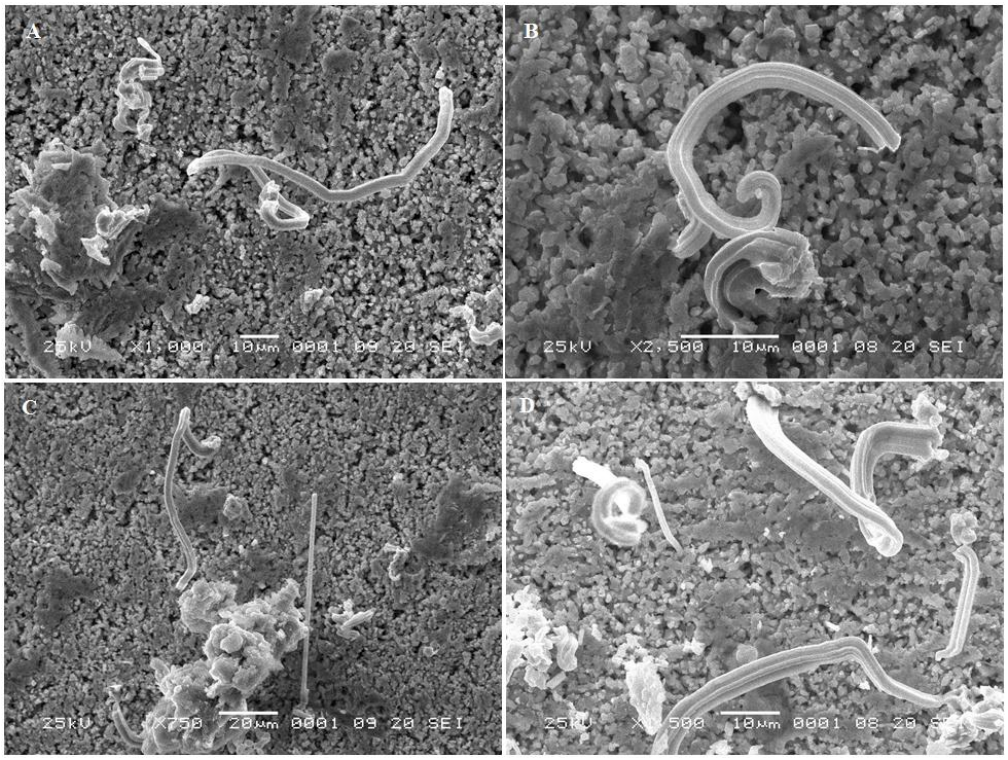

Figure 83: Different shapes of whiskers I

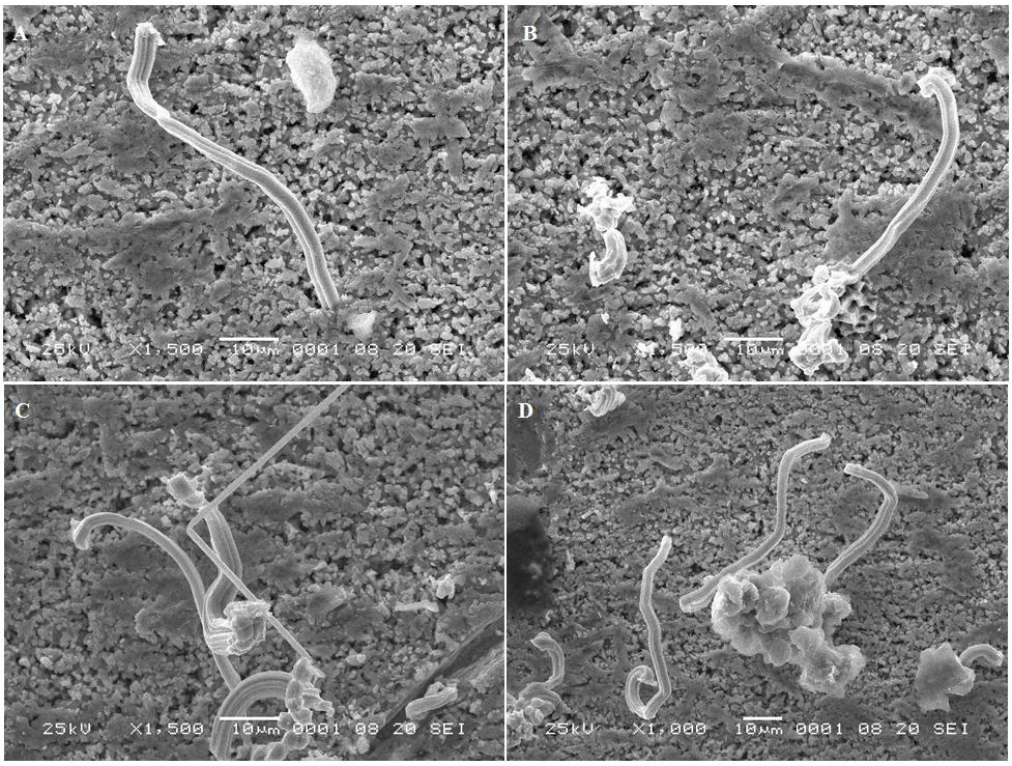

Figure 84: Different shapes of whiskers II

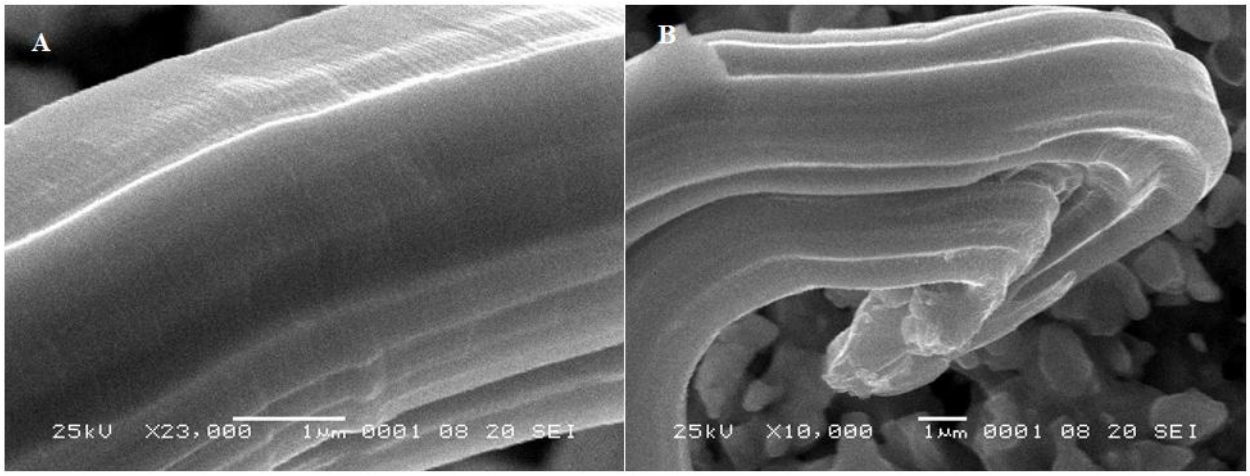

Figure 85: Whisker surface up-close

Figure 85 (A, B) shows the typical faceted surface of the whiskers. The diameter of the whiskers is around 5um.

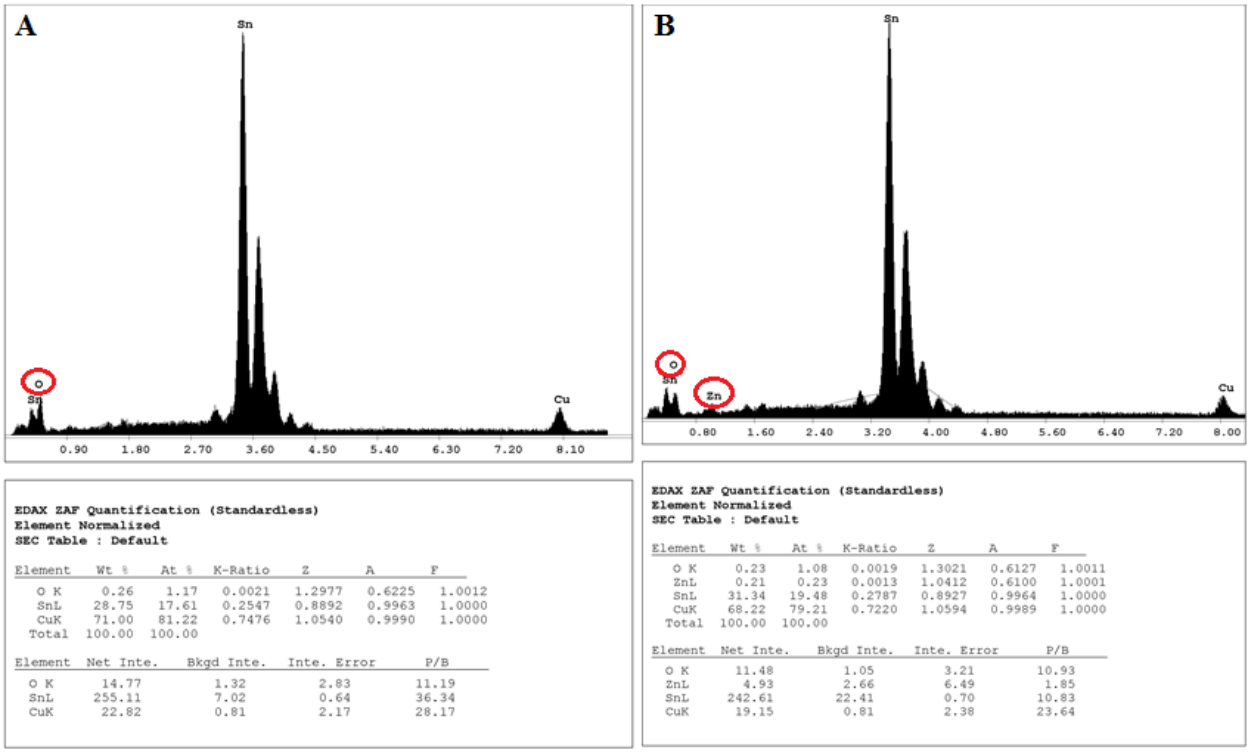

Figure 86: EDS patterns for control samples

Figure 86 (A, B) shows two EDS patterns for the control samples. As expected, Sn and Cu were found on the samples; also oxygen was measured due to the oxidation of the surface. An unexpected Zn peak has been found across many samples. After further investigation, it was found that the sample holder used was the responsible for the contamination with Zn. The aging process used to accelerate the whiskers growth, also oxidizes the surface of the Zn holder causing particles of zinc get into the tin during sample manipulation. Future samples will require to take into consideration the type of holder that is going to be used.

4.2.2.2. Samples with co-sputtered Cu-Ag

Ag and Cu were sputtered on top of two samples containing the Sn electroplated Cu substrates. After reflowing and aging the samples as previously discussed, the characterization process began. Sample #1 was characterized by dividing each point in four quadrants. Then, four areas at a magnification of 150X were selected to perform EDS analysis. An average of the four EDS measurements were used (without taken into consideration the oxygen on the samples) to estimate chemical composition of the samples. Figure 87 shows the average values of Sn, Ag and Cu for each point across the sample.

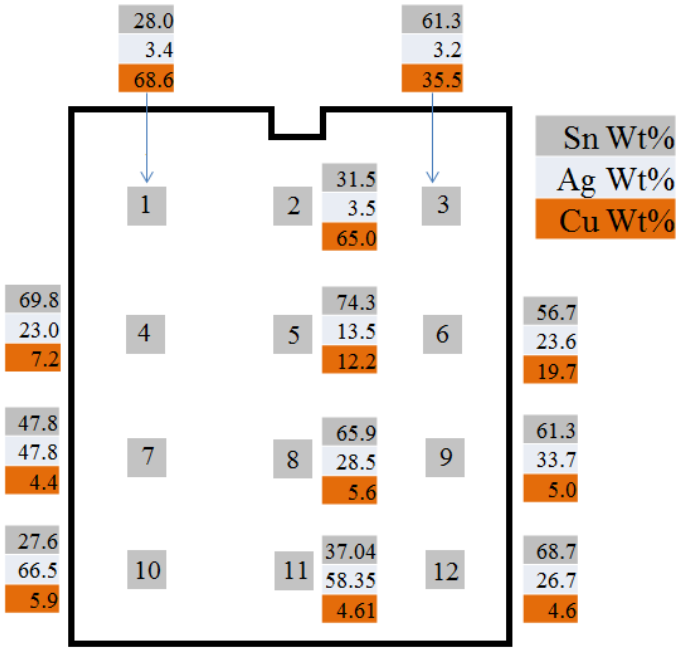

Figure 87: EDS average values for sample #1

According to the data, the side closest to the target had a higher weight percentage of the corresponding material. The second sample was used to test the reproducibility of the technique. The sample was processed using the same parameters of the first one. Figure 88 shows the values obtained for sample #2. The values were obtained by having an EDS measurement on areas randomly selected using a magnification of 75X. The compositional gradient tendency was found to be similar to the one in sample #1, however the values weren't exactly the same. Figure 89 shows schematically the variation of Cu and Ag across the sample.

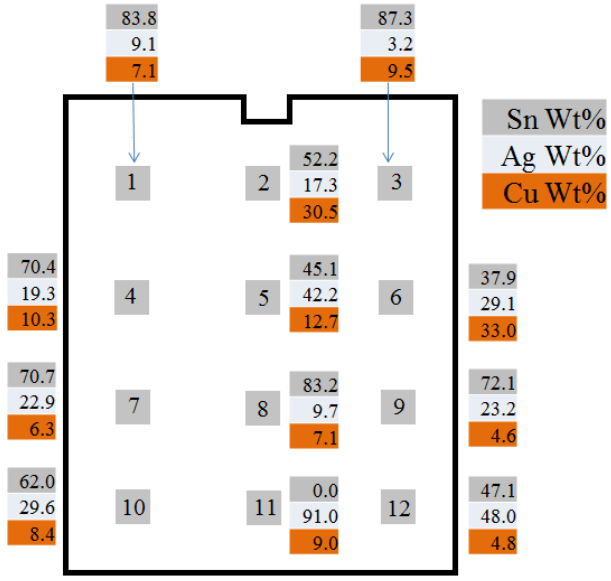

Figure 88: EDS values for sample #2

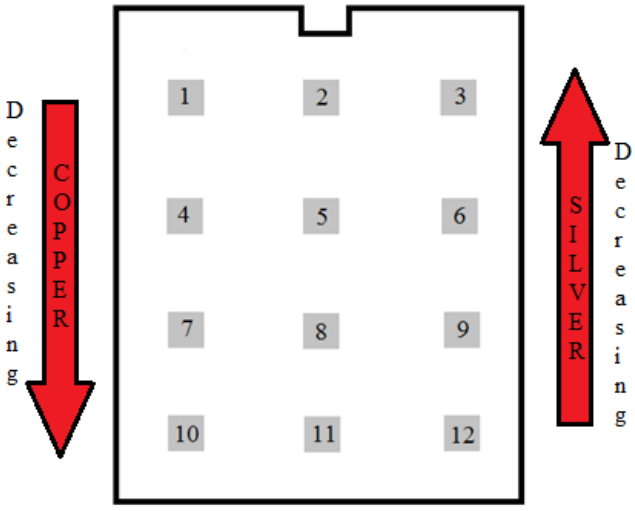

Figure 89: Schematic of compositional gradient

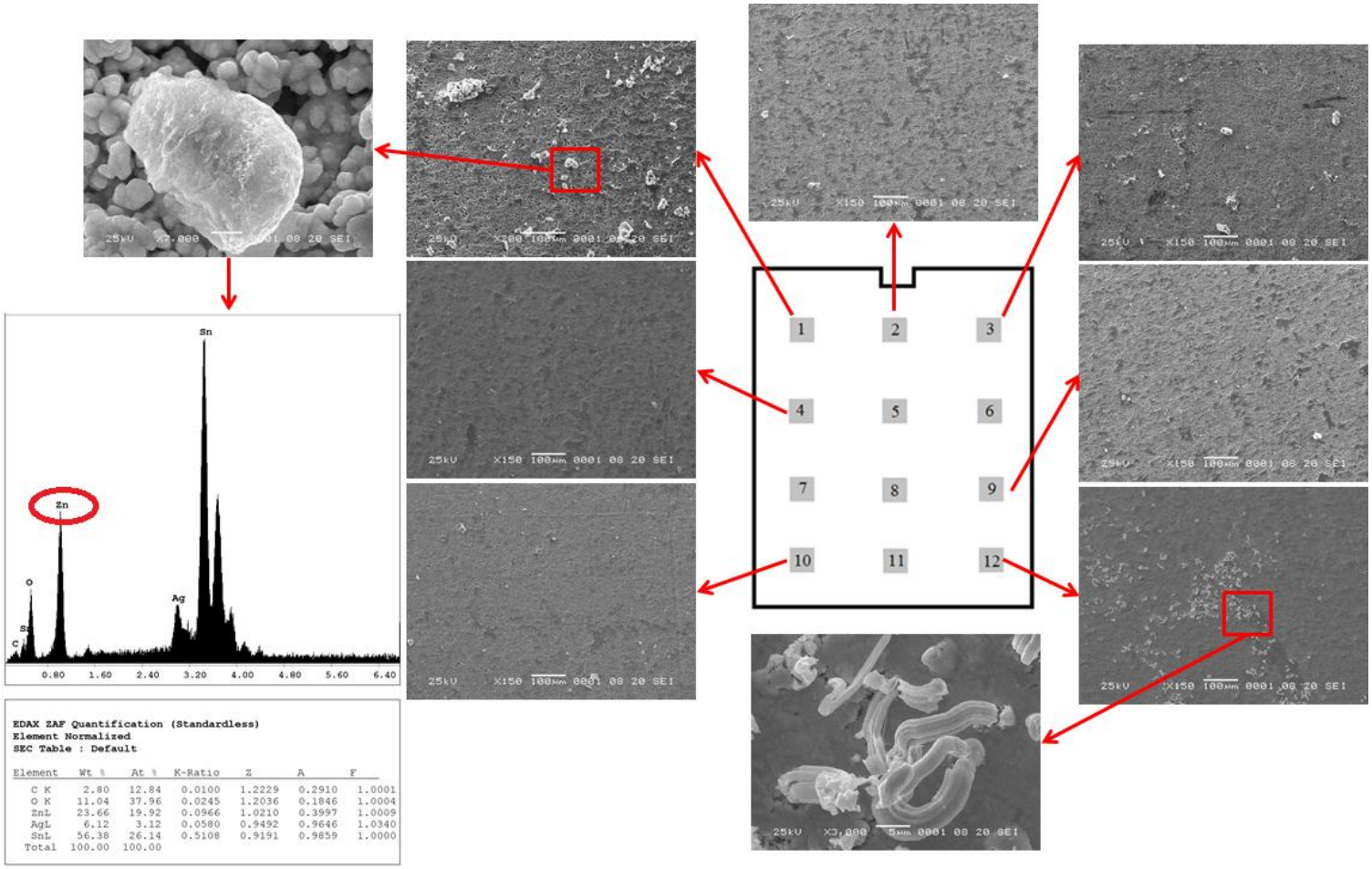

Figure 90: Schematic with SEM results per point in sample #1

Sample #1 showed almost no whiskers grow. As shown in Figure 90, only point 12 had moderate whisker density across it. The bright spots seen on the points are contamination from the holder. The EDS revealed a peak of Zn corresponding to the material from the holder. Points 1 to 11 didn't show any appreciable growth, but the surfaces had considerable amounts of debris from the holder.

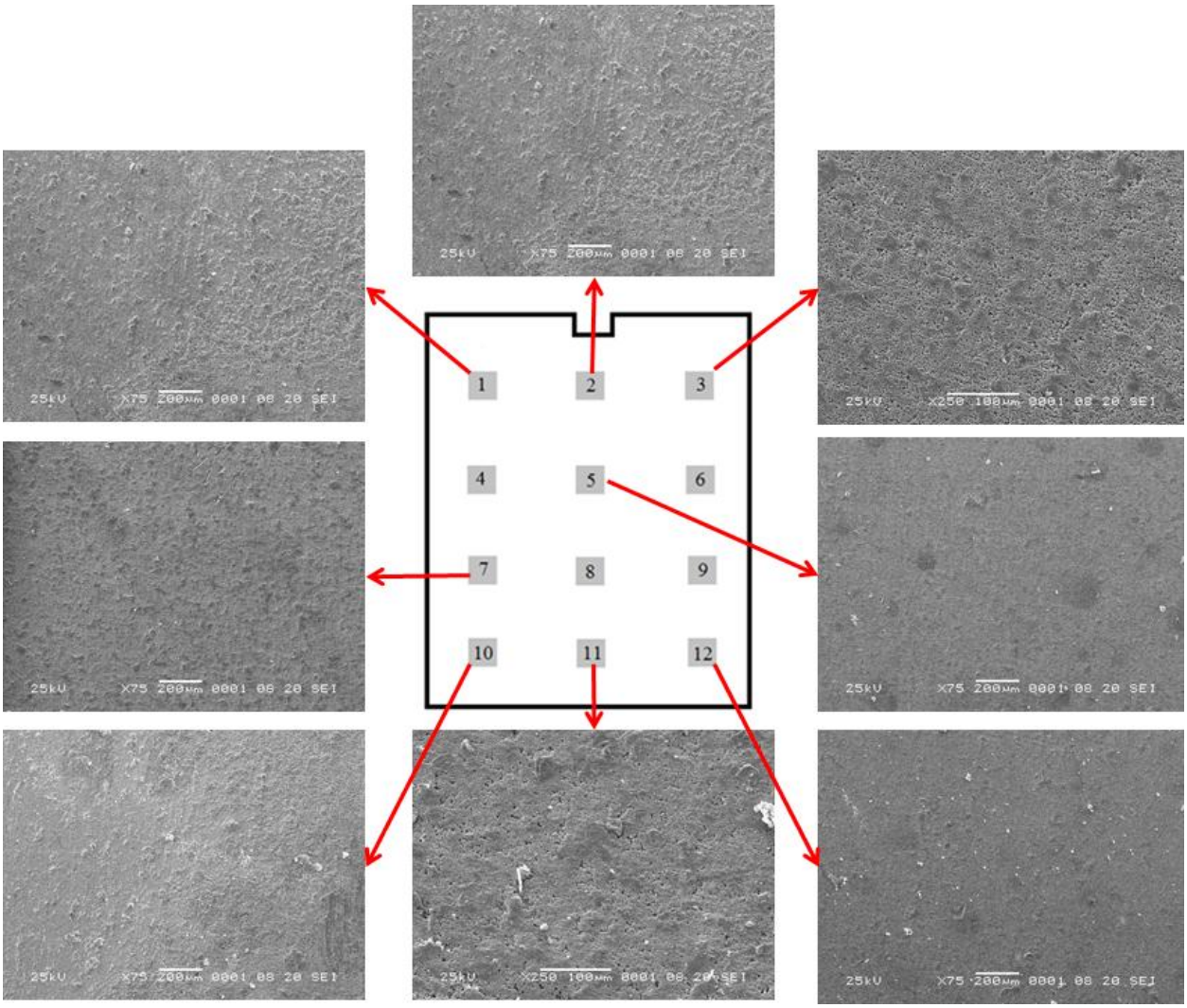

Figure 91: Schematic with SEM results per point in sample #2

The second sample showed no growth at all, as shown in Figure 91. Less contamination was observed in these samples, but there were still some Zn on the samples.

The co-sputtering of Cu and Ag proved to reduce the risk of growing Sn whiskers. Oxidation was found throughout the sample. The samples with Ag and Cu showed higher levels of oxidation, when compared to the control samples. The reflow profile in air has produced the oxides on the samples. Gradients of Ag and Cu were evidently found across the sample. Further refinement of the technique is still needed.

5. CONCLUSIONS AND FUTURE WORK

Sn nanoparticles were successfully synthesized and used in the formulation of a novel nano-solder paste. Low temperatures (~200°C), well below those needed for SAC Pb-free reflow, were used to process the nano-solder paste which resulted in the successful formation of a tinned copper substrate. However, owing to the low metal content and the presence of the organic surfactant, the formation of a bulk metallic joint was not possible at this stage. Commercially available Sn nanoparticles, with no capping agent, were used to prepare a solder paste with higher metallic content in order to proof-the-concept developed from our synthesized paste. After a series of experimental trials, a successful nano-paste was obtained with a best embodiment of 60 wt.% Sn nanoparticles and 40 wt.% flux. From qualitative tests this paste proved to be a potential solution for the reduction of processing temperature on Pb-free solders. Microstructural analysis and mechanical testing were used to characterize the joints which were further related to the process parameters. The optimal condition, when processing the sample in air, was found to be 20 minutes at 200°C which resulted in an evolved metallic microstructure (showing features at the microscale) with minimal pores and peak mechanical response. Prolonged processing times and higher temperatures resulted in excessive oxidation due to the loss of flux presence. Electrical response of the material, i.e. conductivity, was obtained resulting in a value an order of magnitude below bulk tin due to the fact that the resulting structure have pores that are not taken into account in the analysis.

Sn nanoparticles have shown its potential to produce solder joints, but some work still needed in order to suggest this technique as a replacement to current used manufacturing processes. The flux components should be modified in order to obtain fewer residues after the reflow process. To improve the applicability, addition of microparticles to the solder paste should

be assessed in order to reduce cracking and pores across the samples. Also, the addition of a lower melting point material to the solder paste could reduce cracking and pores. The lower melting point material will melt suspending the solid Sn nanoparticles. Due to solid-liquid diffusion an in-situ alloy will be obtained via liquid-phase or transient liquid-phase sintering that could have a higher melting point after processing depending on the materials chosen. The main concern will be to reduce cracks and pores along the sintered material.

A novel technique for sample preparation to test for Sn whiskers has been developed. Compositional gradients were fabricated by the use of magnetron sputtering. Characterization of the sample was simpler when discrete squares were used on top of a holder. A Sn electroplating procedure has been developed and has shown to be prone to whisker growth. The tools of SEM and EDS are pivotal in the development of this screening technique. Almost all elemental compositions showed mitigation or elimination of the Sn whiskers. Combinatorial material science has proved that it can be used as a fast screening method when correctly applied.

Refinement of the screening technique still required. Key issues to assess are the sample preparation, mixing of the elements and sample handling is still required. Contamination from the sample holder was found across the sample; a more suitable sample holder should be used. Thermal analysis of the layered structure acquired after co-sputtering will be required in order to suggest a better reflow profile so that the mixing of the elements get improved. Different holding times should be used and DSC analysis will confirm the consumption of the electroplated Sn, this should be performed in argon to avoid oxidation of the samples.

6. REFERENCES

[1] C. Kazmierski, "Semiconductor Industry Association: Semiconductor Year-over-Year Sales Growth Encouraging," *INDUSTRY STATISTICS*, 2011. [Online]. Available: http://www.sia-online.org/news/2011/05/31/global-sales-reports-2011/semiconductor-year-over-year-sales-growth-encouraging/. [Accessed: 30-Apr-2012].

[2] A. D. Kostic and D. Ph, "Lead-free Electronics Reliability - An Update Lead (Pb) – Some Background," *Group*, no. August. 2011.

[3] Z. Illyefalvi-Vitez and O. Krammer, "Testing the Impact of Pb-free Soldering on Reliability," *IEEE Conference, 2006. 1st*, vol. 00, pp. 468–473, 2006.

[4] C. Andersson, "Manufacture, microstructure and microhardness analysis of Sn-Bi lead-free solder reinforced with Sn-Ag-Cu nano-particles," *2008 International Conference on Electronic Packaging Technology & High Density Packaging*, no. 149, pp. 1–5, Jul. 2008.

[5] Y. Wang, D. Ding, T. Liu, and K. Galuschki, "Effect of Ni barrier on the tin whisker formation of electroplating Sn on lead-frame alloy," *International Conference on Electronic Packaging Technology & High Density Packaging*, pp. 980–983, 2010.

[6] MEC-Innovation, "Understanding the Requirements of the European RoHS Directive and its Impact on Your Business Overview of the RoHS Directive and its Requirements," pp. 1–6, 2006.

[7] S. Mathew, M. Osterman, T. Shibutani, Q. Yu, and M. Pecht, "Tin whiskers: How to mitigate and manage the risks," in *High Density packaging and Microsystem Integration, 2007. HDP'07. International Symposium on*, 2007, pp. 1–8.

[8] C. D. Zou, Y. L. Gao, B. Yang, X. Z. Xia, Q. J. Zhai, C. Andersson, and J. Liu, "Nanoparticles of the Lead-free Solder Alloy Sn-3.0Ag-0.5Cu with Large Melting Temperature Depression," *Journal of Electronic Materials*, vol. 38, no. 2, pp. 351–355, Oct. 2008.

[9] J. Liu, C. Andersson, Y. Gao, and Q. Zhai, "Recent Development of Nano-solder Paste for Electronics Interconnect Applications," in *Electronics Packaging Technology Conference, 2008. EPTC 2008. 10th*, 2008, pp. 84–93.

[10] J. Lau, C. Wong, and N. Lee, "Electronics manufacturing: with lead-free, halogen-free, and conductive-adhesive materials," 2003.

[11] J. E. Morris, "Nanoparticles Properties," in *Nanopackaging: Nanotechnologies and Electronics Packaging*, Springer, 2009, pp. 1–14.

[12] S. Lai, J. Guo, V. Petrova, G. Ramanath, and L. Allen, "Size-Dependent Melting Properties of Small Tin Particles: Nanocalorimetric Measurements.," *Physical review letters*, vol. 77, no. 1, pp. 99–102, Jul. 1996.

[13] C. Zou, Y. Gao, B. Yang, and Q. Zhai, “Size-dependent melting properties of Sn nanoparticles by chemical reduction synthesis,” *Transactions of Nonferrous Metals Society of China*, vol. 20, no. 2, pp. 248–253, Feb. 2010.

[14] V. V. Lubashenko, “Size-dependent melting of nanocrystals: a self-consistent statistical approach,” *Journal of Nanoparticle Research*, vol. 12, no. 5, pp. 1837–1844, Aug. 2009.

[15] H. Jiang, K. J. Moon, and C. Wong, “Nanolead-Free Solder Pastes for Low Processing Temperature Interconnect Applications in Microelectronic Packaging,” *Nano-Bio-Electronic, Photonic and MEMS Packaging*, p. 217, 2009.

[16] H. Jiang and C. P. Wong, “Low Processing Temperature of Lead-Free Solder Interconnects,” *IEEE Nanotechnology Magazine*, vol. 4, no. 2, pp. 20–23, Jun. 2010.

[17] V. Schroeder, P. Bush, M. Williams, N. (Nick) Vo, and H. L. Reynolds, “Tin Whisker Test Method Development,” *IEEE Transactions on Electronics Packaging Manufacturing*, vol. 29, no. 4, pp. 231–238, Oct. 2006.

[18] T. Shibutani, M. Osterman, and M. Pecht, “Standards for Tin Whisker Test Methods on Lead-Free Components,” *Components and Packaging Technologies, IEEE Transactions on*, vol. 32, no. 1, pp. 216–219, Oct. 2009.

[19] H. Hao, Y. Shi, Z. Xia, Y. Lei, and F. Guo, “Oxidization-Induced Tin Whisker Growth on the Surface of Sn-3.8Ag-0.7Cu-1.0Er Alloy,” *Metallurgical and Materials Transactions A*, vol. 40, no. 8, pp. 2016–2021, Jun. 2009.

[20] J. Brusse, G. Ewell, and J. Siplon, “Tin whiskers: Attributes and mitigation,” *Carts Europe*, vol. 16, no. March, pp. 67–80, 2002.

[21] M. Schmidt, R. Kusche, and H. Haberland, “Irregular variations in the melting point of size-selected atomic clusters,” *Nature*, vol. 393, no. May, pp. 238–240, 1998.

[22] M. Efremov, F. Schiettekatte, M. Zhang, E. Olson, A. Kwan, R. Berry, and L. Allen, “Discrete periodic melting point observations for nanostructure ensembles,” *Physical review letters*, vol. 85, no. 17, pp. 3560–3, Oct. 2000.

[23] H. Jiang, K. Moon, F. Hua, and C. P. Wong, “Synthesis and Thermal and Wetting Properties of Tin/Silver Alloy Nanoparticles for Low Melting Point Lead-Free Solders,” *Chemistry of Materials*, vol. 19, no. 18, pp. 4482–4485, Sep. 2007.

[24] H. Jiang and C. P. Wong, “Tin/silver/copper alloy nanoparticle pastes for low temperature lead-free interconnect applications,” *2008 58th Electronic Components and Technology Conference*, pp. 1400–1404, May 2008.

[25] H. Alarifi, A. Hu, M. Yavuz, and Y. N. Zhou, “Silver Nanoparticle Paste for Low-Temperature Bonding of Copper,” *Journal of Electronic Materials*, vol. 40, no. 6, pp. 1394–1402, Mar. 2011.

[26] L.-Y. Hsiao and J.-G. Duh, “Synthesis and Characterization of Lead-Free Solders with Sn-3.5Ag-xCu (x=0.2, 0.5, 1.0) Alloy Nanoparticles by the Chemical Reduction Method,” *Journal of The Electrochemical Society*, vol. 152, no. 9, p. J105, 2005.

[27] D. C. Lin, T. S. Srivatsan, G.-X. Wang, and R. Kovacevic, “Understanding the Influence of Copper Nanoparticles on Thermal Characteristics and Microstructural Development of a Tin-Silver Solder,” *Journal of Materials Engineering and Performance*, vol. 16, no. 5, pp. 647–654, May 2007.

[28] D. Wakuda, K. S. Kim, and K. Suganuma, “Time-dependent sintering properties of Ag nanoparticle paste for room temperature bonding,” in *Nanotechnology, 2009. IEEE-NANO 2009. 9th IEEE Conference on*, 2009, vol. 8, pp. 412–415.

[29] M. Osterman, “Mitigation Strategies for Tin Whiskers.”

[30] Q. Sun, “Understanding and Minimization of Tin Whiskers,” 2003.

[31] A. Vicenzo, “Tin Whiskers : Testing and Mitigation,” no. April, pp. 1–19, 2006.

[32] L. Panashchenko and M. Osterman, “Examination of nickel underlayer as a tin whisker mitigator,” *2009 59th Electronic Components and Technology Conference*, pp. 1037–1043, May 2009.

[33] Y. Fukuda, M. Osterman, and M. Pecht, “The effect of annealing on tin whisker growth,” *Electronics Packaging Manufacturing, IEEE Transactions on*, vol. 29, no. 4, pp. 252–258, 2006.

[34] R. F. Champaign and R. R. Ogden, “Microscopy Study of Tin Whiskers,” *Journal of Failure Analysis and Prevention*, vol. 10, no. 6, pp. 444–449, Sep. 2010.

[35] P. O. Quintero-Aguiló, P. Cáceres-Valencia, R. Valentin, and A. Diaz, “Combinatorial Studies for the Minimization of Tin Whiskers Growth in Lead Free Electronics,” in *IPACK*, 2009, pp. 1–6.

[36] H. Kwak and T. Hubing, “AN OVERVIEW OF ADVANCED ELECTRONIC PACKAGING TECHNOLOGY,” *Clemson University Vehicular Electronics Lab*, 2007.

[37] S. Lopez-buedo and E. Boemo, “Electronic Packaging Technologies,” *Universidad Autonoma de Madrid*.

[38] R. Tummala, “Fundamentals of microsystems packaging,” *McGraw-Hill*, 2001.

[39] N. Ghalib, Q. Chu, and G. Wable, “Lead-Free Reflow Profile Study,” in *Lead-free Electronic Components and Assemblies*, 2003.

[40] J. Pérez, L. Bax, and C. Escolano, “Roadmap Report on Nanoparticles,” *nanoroadmap project*, no. November, pp. 1–57, 2005.

[41] W. YONG, “Nanosize tin composite anode materials for lithium ion batteries,” National University of Singapore, 2004.

[42] A. Velasco-Abreo, “PREPARATION OF COPPER-BEARING NANOFLUIDS FOR THERMAL APPLICATIONS,” University of Puerto Rico, 2008.

[43] R. Viswanatha and D. D. Sarma, *Growth of Nanocrystals in Solution*. 2007, pp. 139–170.

[44] J. Bonsak, “CHEMICAL SYNTHESIS OF SILVER NANOPARTICLES FOR LIGHT TRAPPING APPLICATIONS IN SILICON SOLAR CELLS,” University of Oslo, 2010.

[45] M. Zhang, M. Efremov, F. Schiettekatte, E. Olson, a. Kwan, S. Lai, T. Wisleder, J. Greene, and L. Allen, “Size-dependent melting point depression of nanostructures: Nanocalorimetric measurements,” *Physical Review B*, vol. 62, no. 15, pp. 10548–10557, Oct. 2000.

[46] K. Nanda, “Size-dependent melting of nanoparticles: Hundred years of thermodynamic model,” *Pramana*, vol. 72, no. 4, pp. 617–628, 2009.

[47] K. F. Peters, Y.-W. Chung, and J. B. Cohen, “Surface melting on small particles,” *Applied Physics Letters*, vol. 71, no. 16, p. 2391, 1997.

[48] Q. Mei and K. Lu, “Melting and superheating of crystalline solids: From bulk to nanocrystals,” *Progress in Materials Science*, vol. 52, no. 8, pp. 1175–1262, Nov. 2007.

[49] E. A. Olevsky, “SINTERING THEORY: a brief introduction,” in *SAN DIEGO STATE UNIVERSITY, CALIFORNIA, USA*, 2011.

[50] J. R. Groza, “Nanocrystalline powder consolidation methods,” pp. 115–178, 2007.

[51] Q. Sun and G. Selvaduray, “Understanding and Minimizing Tin Whiskers,” *Materials Engineering*, 2003.

[52] J. Smetana, “Theory of Tin Whisker Growth : ‘ The End Game ’,” *Electronics Packaging Manufacturing, IEEE*, vol. 30, no. 1, pp. 11–22, 2007.

[53] D. Smith, *Thin-Film Deposition: Principles and Practice*. McGraw-Hill Professional, 1995, p. 616.

[54] J. E. Mahan, *Physical Vapor Deposition of Thin Films*. Wiley-Interscience, 2000, p. 336.

[55] Y. Kwon, M. G. Kim, Y. Kim, Y. Lee, and J. Cho, "Effect of Capping Agents in Tin Nanoparticles on Electrochemical Cycling," *Electrochemical and Solid-State Letters*, vol. 9, no. 1, p. A34, 2006.

[56] H. Jiang, K. J. Moon, and C. P. Wong, "Nano-Bio- Electronic, Photonic and MEMS Packaging," 2010.

[57] C. C. Johnson and J. Kevra, *Solder Paste Technology: Principles and Applications*. Tab Professional & Reference, 1989, p. 304.

[58] "Standard Reflow Profile for Standard and Lead-Free Packages," *Actel Power Matters*, no. June, 2008.

[59] S. K. Kang, "Recent Progress in Lead (Pb) - Free Solders and Soldering Technology," vol. 3932. 2002.

[60] Mettler Toledo, "Interpreting DSC curves Part 1: Dynamic measurements," 2000.

[61] G. T. Galyon, "A History of Tin Whisker Theory : 1946 to 2004," *New York*, 2004.